

Theoretical Study of Heat Transport in Si-based Ordered, Disordered and Nanostructured Bulk Materials

By

YUPING HE

B.S. (China Agriculture University, China) 1998

M.S. (University of Science and Technology Beijing, China) 2001

M.S. (Southern Methodist University, United States) 2006

DISSERTATION

Submitted in partial satisfaction of the requirements for the degree of

DOCTOR OF PHILOSOPHY

in

CHEMISTRY

in the

OFFICE OF GRADUATE STUDIES

of the

UNIVERSITY OF CALIFORNIA

DAVIS

Approved:

Giulia Galli (Chair)

Gang-yu Liu

Susan M. Kauzlarich

Committee in Charge
2011

UMI Number: 3499549

All rights reserved

INFORMATION TO ALL USERS

The quality of this reproduction is dependent on the quality of the copy submitted.

In the unlikely event that the author did not send a complete manuscript and there are missing pages, these will be noted. Also, if material had to be removed, a note will indicate the deletion.



UMI 3499549

Copyright 2012 by ProQuest LLC.

All rights reserved. This edition of the work is protected against unauthorized copying under Title 17, United States Code.



ProQuest LLC.
789 East Eisenhower Parkway
P.O. Box 1346
Ann Arbor, MI 48106 - 1346

Copyright by

Yuping He

2011

This dissertation is dedicated

to my daughters

Tracy Xu and Kayla Xu

and my husband

Yue Xu

List of symbols

T	Temperature
S	Seebeck coefficient
I	Electric current
\mathbf{J}	Heat current
Π	Peltier coefficient
J_e	Current density
μ	Thomson coefficient
σ	Electrical conductivity
κ	Thermal conductivity
W	Potential energy
\mathbf{v}	Atomic velocity
\mathbf{F}	Atomic force
t	Time
\mathbf{a}	Atomic acceleration
m	Atomic mass
\mathbf{u}	Atomic displacement
ω	Angular frequency
ν	Frequency
\mathbf{k}	Wave vector
V	Volume
\mathbf{s}	Stress tensor
k_B	Boltzmann constant
τ	Lifetime
λ	Mean free path
\mathbf{v}_g	Group velocity
\hbar	Reduced plank constant
c	Specific heat
P	Pressure

Theoretical Study of Heat Transport in Si-based Ordered, Disordered and Nanostructured Bulk Materials

Abstract

Thermoelectric materials, which can either generate electricity from waste heat or use electricity for solid-state Peltier cooling, are to date inefficient, compared to conventional generators and refrigerators. One way to obtain systems with improved efficiency is to engineer nanostructured semiconductors, so as to reduce the thermal conductivity of the crystalline material, while preserving its electronic properties. Such a strategy has been recently applied to Si, an Earth abundant, cheap and non-toxic material, and promising results have been obtained for Si nanowires and thin films of nanoporous Si. Mass disorder may also help reduce the thermal conductivity of semiconductors and indeed SiGe alloys are efficient thermoelectric materials, but unfortunately only at high temperature.

This dissertation presents a theoretical investigation of the microscopic mechanisms responsible for heat transport in Si and SiGe alloys at the nanoscale, with the goal of providing insight into design rules for efficient thermoelectric semiconductors. We carried out a detailed atomistic study of the thermal conductivity (κ) of crystalline, amorphous and nanostructured Si and SiGe alloys, using several theoretical and computational approaches — equilibrium molecular dynamics (EMD), non-equilibrium molecular dynamics (NEMD), the Boltzmann transport equation (BTE) and the Allen-Feldman (AF) theory. We also studied the thermal properties of SiO₂, which is most often present on surfaces of Si based materials, when exposed to air.

We first investigated heat conduction in crystalline Si and Ge to test the numerical and theoretical approximations adopted in our study, including the size of the molecular dynamics cells, the simulation time and the interatomic potentials. Our findings permitted to understand and reconcile apparently conflicting results reported in the literature for these materials. We then carried out simulations for amorphous Si (*a*-Si) and disordered SiGe alloys, to study the effect of structural disorder and of mass disorder on heat conduction.

In the case of *a*-Si we found that the majority of heat carriers are quasi-stationary modes; however the small proportion (about 3%) of propagating vibrations contributes to about half of the value of κ . We showed that in bulk samples the mean free path of several long-wavelength modes is of the order of microns; this value may be substantially decreased either in thin films or in systems with etched holes, resulting in a smaller thermal conductivity. Our results provided a unified explanation of several experiments and showed that kinetic theory cannot be applied to describe thermal transport in *a*-Si at room temperature.

Heat transport in amorphous silica was found to be qualitatively different from that in *a*-Si due to the absence of propagating modes. In the case of SiGe alloys, heat transport is dominated by mass disorder; we found that a small amount of propagating modes with long mean free paths is responsible for most of the value of the thermal conductivity measured in SiGe materials.

Building on our results for crystalline and disordered Si and SiGe, we then studied nanostructured Si and SiGe. In particular we focused on nanoporous Si and nanoporous SiGe, that is bulk Si and stoichiometric SiGe samples with nano holes, and we considered different geometrical arrangements of holes, and ordered and disordered hole surfaces. Using molecular dynamics simulations and lattice dynamics

calculations, we showed that the thermal conductivity of nanoporous silicon may attain values 10~20 times smaller than in the bulk for porosities and surface-to-volume ratios similar to those obtained in recently fabricated nanomeshes. We also showed that further reduction of almost an order of magnitude is obtained in thin films with thickness of 20nm, in agreement with experiment. Our lattice dynamics analysis indicated that the presence of pores has two main effects on the heat carriers: the appearance of non-propagating, diffusive modes and the reduction of the group velocity of propagating modes. The former effect is enhanced by the presence of disorder at the pore surfaces, while the latter is enhanced by decreasing film thickness.

The thermal conductivity of stoichiometric SiGe alloys may be decreased as well by nanostructuring. Our MD simulations showed that it may be reduced by more than one order of magnitude, by etching nanometer-sized holes in the material, and it becomes almost constant as a function of temperature between 300 and 1100 K for samples with 1 nm wide pores. In nanoporous SiGe, thermal conduction is largely determined by mass disorder and boundary scattering, and thus the dependence of κ on pore distance and on structural, atomistic disorder is much weaker than in the case of nanoporous Si. These results indicate that one may minimize the thermal conductivity of the alloy with less stringent morphological constraints than for pure Si.

These results found quantitative validation in several recent experiments and provide an atomistic description of the microscopic mechanisms of heat transport at the nanoscale.

Acknowledgments

I am really lucky to have Prof. Giulia Galli as my advisor. I am still thankful that she admitted me to our ANGSTROM group in the first place. It is Giulia who first triggered my interest in heat transport at nanoscale. This Ph.D thesis would not have been possible without Giulia's support and guidance. What I have learned from Giulia is not only the knowledge of scientific computing, but also her passion and faith in computational materials science.

I am also grateful for the encouragement and guidance of the other members of my thesis committee, Prof. Gangyu Liu and Prof. Susan Kauzlarich.

I would like to thank all the former and current group members, special thanks to Dr. Davide Donadio for building up the basic and wonderful foundations for my heat transport research and for teaching me how to run the simulation jobs and debug the code. I like to thank Dr. Ivana Savic for the useful discussion. I owe my deepest gratitude to Dr. Yan Li. Her encouragement to me made this thesis possible. I would like to show my gratitude to Dr. Deyu Lu, Dr. Tianshu Li, Dr. Éamonn D. Murray and Tuan Anh Pham for your help in using group cluster.

I would also like to thank our former group assistant, Ibra Henley, and our current group assistant Mary Woolf, for listening to my practice of presentations.

Finally, to my husband and my daughters, thank you for your support and love.

List of Figures

1.1.1	Schematic diagram of a typical thermoelectric module.	4
1.1.2	Efficiency of thermoelectrics as a function of size	5
1.2.1	Figure of merit ZT of semiconductors as a function of year of discovery	6
2.2.1	Simplified diagram of a molecular dynamics simulation.	10
2.2.2	Schematic representation of a two-dimensional periodic system.	16
2.2.3	Schematic representation of non-equilibrium MD simulation cell.	21
3.2.1	Schematic diagram of the diamond structure.	40
3.2.2	Heat current autocorrelation function of c-Si.	41
3.2.3	Thermal conductivity of c-Si as a function of atoms in the MD cell.	43
3.2.4	Exchange of kinetic energy in non-equilibrium MD.	44
3.2.5	Temperature profile in c-Si in non-equilibrium MD for 500ps.	45
3.2.6	Temperature profile in c-Si in non-equilibrium MD for 2ns.	46
3.2.7	Inverse of thermal conductivity of c-Si as a function of L_Z	48
3.2.8	Group velocities of c-Si as a function of frequency.	50
3.2.9	Lifetimes of c-Si as a function of frequency.	50
3.2.10	Mean free paths of c-Si as a function of frequency.	51
3.2.11	Ratio between quantum and classical values of heat capacity of c-Si.	51
3.2.12	Thermal conductivity of c-Si from the BTE.	52

3.3.1	Heat current autocorrelation function of c-Ge	54
3.3.2	Thermal conductivity of c-Ge as a function of atoms in the MD cell.	56
3.3.3	Phonon density of states of c-Ge and c-Si	57
3.3.4	Group velocities of c-Ge as a function of frequency.	58
3.3.5	Lifetimes of c-Ge as a function of frequency.	58
3.3.6	Mean free paths of c-Ge as a function of frequency.	59
3.3.7	Ratio between quantum and classical values of heat capacity of c-Ge.	60
3.3.8	Thermal conductivity of c-Ge from the BTE.	60
3.4.1	Unit cell of the α -cristobalite crystal.	61
3.4.2	Bond angle distribution of α -SiO ₂	62
3.4.3	Partial radial distribution functions of α -SiO ₂	63
3.4.4	Coordination numbers of oxygen and silicon in α -SiO ₂	63
3.4.5	Heat current autocorrelation function of α -SiO ₂	66
3.4.6	Contributions of convective and conductive items to thermal conductivity of α -SiO ₂ from convection and conduction.	67
3.4.7	Thermal conductivity of α -SiO ₂ as a function of atoms in the MD cell.	69
3.4.8	Phonon density of states of α -SiO ₂	70
3.4.9	Group velocities of α -SiO ₂ as a function of frequency	71
3.4.10	Lifetimes of α -SiO ₂ as a function of frequency.	71
3.4.11	Mean free paths of α -SiO ₂ as a function of frequency.	72
3.4.12	Thermal conductivity of α -SiO ₂ from the BTE.	73
3.4.13	Thermal conductivity of α -SiO ₂ from the Allen-Feldman theory. . .	74
4.2.1	Radial distribution function and structure factor of a -Si.	77
4.2.2	Angle distribution function of a -Si.	78
4.2.3	Heat current autocorrelation function of a -Si.	79

4.2.4	Temperature profile of <i>a</i> -Si in NEMD.	80
4.2.5	Thermal conductivity of <i>a</i> -Si by EMD and NEMD.	80
4.2.6	Temperature gradient of <i>a</i> -Si in NEMD.	81
4.2.7	Lifetime and mean free path of <i>a</i> -Si.	83
4.2.8	Phonon density of states of <i>a</i> -Si.	86
4.2.9	Thermal conductivity of <i>a</i> -Si by MD and the BTE.	87
4.3.1	Heat current auto-correlation function of SiGe.	89
4.3.2	Thermal conductivity of SiGe as a function of the cell.	90
4.3.3	Mean free paths of SiGe as a function of frequency.	90
4.3.4	HCAF of SiGe as a function of the size.	91
4.3.5	Lattice constant of SiGe.	93
4.3.6	Composition dependence of κ in $\text{Si}_{1-x}\text{Ge}_x$ alloys.	93
4.4.1	Bond angle distribution in <i>a</i> - SiO_2	96
4.4.2	Partial radial distribution functions of <i>a</i> - SiO_2	97
4.4.3	Coordination numbers of <i>a</i> - SiO_2	97
4.4.4	Structure factor of <i>a</i> - SiO_2	98
4.4.5	Heat current autocorrelation function of <i>a</i> - SiO_2	100
4.4.6	Thermal conductivity of <i>a</i> - SiO_2 as a function of atoms in the MD cell.100	
4.4.7	Group velocities of <i>a</i> - SiO_2 as a function of frequency	101
4.4.8	Lifetimes of <i>a</i> - SiO_2 as a function of frequency.	102
4.4.9	Mean free paths of <i>a</i> - SiO_2 as a function of frequency.	102
4.4.10	Phonon density of states of <i>a</i> - SiO_2	103
4.4.11	Thermal conductivity of <i>a</i> - SiO_2 as a function of the Lorentzian width.105	
4.4.12	Phase quotient of <i>a</i> - SiO_2	106
4.4.13	Spatial decay of vibrational states of <i>a</i> - SiO_2	107

4.4.14	Inverse participation of a -SiO ₂	107
5.2.1	Representative picture of np-Si.	112
5.2.2	Group velocities of np-Si as a function of frequency.	115
5.2.3	Phase quotient of c-Si, a -Si and np-Si as a function of frequency. . .	115
5.2.4	Mean free paths of c-Si, a -Si and np-Si as a function of frequency. .	117
5.3.1	Schematic diagram of np-SiGe.	118
5.3.2	Thermal conductivity of bulk SiGe and np-SiGe.	120
5.3.3	Heat current autocorrelation function of np-SiGe.	121
5.3.4	Thermal conductivity of np-Si and np-SiGe as a function of pore spacing	122
5.3.5	Mean free paths of np-SiGe as a function of frequency.	123
5.3.6	Group velocities of np-SiGe as a function of frequency.	124
5.3.7	Lifetimes of np-SiGe as a function of frequency.	125
5.3.8	Thermal conductivity of np-SiGe as a function of T and mean free path.	127

List of Tables

2.2.1	Parameters of the Tersoff potential for silicon and germanium. . . .	15
2.2.2	Parameters of the Tersoff potential for silicon and oxygen in SiO ₂ .	15
2.4.1	Summary of theoretical methods used to compute the thermal conductivity.	33
3.1.1	Experimental and theoretical κ of c-Si at 300K	37
3.1.2	Experimental κ of c-Ge at 300K	38
3.2.1	Thermal conductivity of c-Si as a function of number atoms in MD cell.	42
3.3.1	Thermal conductivity of c-Ge as a function of number of atoms in MD cell.	55
3.4.1	Thermal conductivity of α -SiO ₂ as a function of number atoms in MD cell.	65
4.2.1	Thermal conductivity of <i>a</i> -Si as a function of film thickness.	84
4.4.1	Experimental results of κ of <i>a</i> -SiO ₂	95
4.4.2	Thermal conductivity of <i>a</i> -SiO ₂ as a function of number atoms in MD cell.	99
5.2.1	Ratio between κ computed for c-Si and np-Si.	112

5.3.1	κ of np-SiGe as a function of porosity.	121
-------	--	-----

Contents

List of symbols	iii
Abstract	iv
Acknowledgments	vii
List of figures	xi
List of tables	xiii
1 Introduction	1
1.1 Review of thermoelectricity	1
1.2 Thermoelectricity in semiconductor nanostructures	5
1.3 Motivation and outline of the thesis	7
2 Theoretical approaches	8
2.1 Thermal conductivity	8
2.2 Molecular dynamics simulations	9
2.2.1 Equilibrium molecular dynamics	17
2.2.2 Non-equilibrium molecular dynamics	20
2.3 Boltzmann transport equation	21

2.3.1	Lattice dynamics	22
2.3.2	Approximate solutions for ordered systems	26
2.3.3	Approximate solutions for disordered systems	30
2.4	Summary	33
3	Heat transport in ordered bulk materials	34
3.1	Background and objectives	34
3.1.1	Silicon	34
3.1.2	Germanium	37
3.1.3	Silicon dioxide	38
3.2	Thermal transport in bulk crystalline silicon	39
3.3	Thermal transport in bulk crystalline germanium	53
3.4	Thermal transport in bulk crystalline silicon dioxide	61
4	Heat transport in disordered bulk materials	75
4.1	Background and objectives	75
4.2	Thermal transport in amorphous silicon	75
4.3	Thermal transport in silicon germanium alloy	88
4.4	Thermal transport in amorphous silicon dioxide	94
5	Heat transport in nanostructured bulk materials	109
5.1	Background and objectives	109
5.2	Thermal transport in nanoporous silicon	111
5.3	Thermal transport in nanoporous silicon germanium	117
6	Conclusions	128

Chapter 1

Introduction

1.1 Review of thermoelectricity

The thermoelectric effect consists of the conversion of a temperature difference into electric voltage and vice versa. Below we briefly review experimental and theoretical studies of the thermoelectric effect, starting from its discovery at the end of the 19th century.

Research into thermoelectricity dates back to the 19th century. In 1821, Thomas Seebeck [1] discovered that a compass needle is deflected if placed near a closed loop made of two dissimilar metals when one of the metal junctions is heated. However he attributed this phenomenon to magnetic effects. The generated voltage difference (ΔV) at the end of the junction depends on the temperature difference (ΔT) between the pair of materials: $\Delta V = S \bullet \Delta T$, where S is now known as Seebeck coefficient. In 1833, Jean Peltier [2] discovered that there is a temperature change at a junction of dissimilar metals when current flows: $J = \Pi I$, here J is the rate at which heat is absorbed, I is the electric current and Π is now known as the Peltier coefficient. The Peltier effect was further demonstrated and explained by Lenz in

1838. In 1851, William Thomson [3], Lord Kelvin found that a material may be heated and cooled by imposing an electric current in the presence of a temperature gradient: $q = \rho J_e^2 - \mu J_e \frac{dT}{dx}$, where J_e is the current density, ρ is the resistivity of the conductor, dT/dx is the temperature gradient between two sides of the conductor, and μ is now known as the Thomson coefficient. In 1854, Thomson established the proportionality relationships among Seebeck, Peltier and Thomson coefficients : $\mu = T \frac{dS}{dT}$ and $\Pi = S \bullet T$, where T is the absolute temperature. The Thomson coefficient is a property of individual materials, while the Seebeck and Peltier coefficients may only be determined for pairs of materials.

The possibility of using the thermoelectric effect in power generation was first proposed by Rayleigh in 1885, who, however, incorrectly calculated the efficiency of thermoelectric generators. In 1909 [4] and 1911 [5], Altenkirch developed a correct theory of thermoelectric generation, and showed that efficient thermoelectric materials should possess large Seebeck coefficients (S), and small thermal conductivity (κ) to retain the heat at the junctions, and low electrical resistance (or large electrical conductivity σ) to minimize the Joule heating. These transport properties may be used to define a figure of merit: $Z = S^2 \sigma / \kappa$ with unit $1/K$. A dimensionless quantity ZT is generally used to describe the efficiency of thermoelectric materials, where T is the average working temperature. The efficiency of thermoelectric devices is proportional to the material's Figure of Merit ZT .

In the 1920s, researchers investigated a large number of materials to search for systems with large ZT . The search was focused on metals and metal alloys. In these materials, the ratio of electrical and thermal conductivity (σ/κ) is a constant according to Wiedemann-Franz law [6]. It is not possible to increase one while decreasing the other. Therefore, the efficiency of thermoelectric generators made from metals or

metal alloys is rather low, about 1%. In the 1930s, semiconductors were synthesized and were predicted to have larger Seebeck coefficients than metals. Unfortunately, the ratio of electrical to thermal conductivity in semiconductors is much smaller than that of metals, so that the thermal efficiency of semiconductors turned out to be on average an improvement of only 5% with respect to that of metals. In 1956, Ioffe and his co-workers [7] showed that the ratio σ/κ could be increased in semiconducting compounds with isomorphous elements (that is elements belonging to same group of the periodic table), e.g. SiGe. Following Ioffe's discovery, in U.S. laboratories, several other semiconductor alloys were synthesized with thermoelectric efficiency upto 10%, paving the way to many applications. For example, in 1961 [8], the first radioisotope thermoelectric generator (RTG) was built and launched in space, where the heat released by the decay of radioactive material was converted into electricity by an array of thermocouples based on the Seebeck effect. RTGs built out of silicon germanium alloys, lead telluride and tellurides of antimony are still used in space missions. In the late 1970s, due to the increasing price of oil and awareness about global warming, scientific activities to search for and develop environmentally friendly sources of electrical power based on thermoelectric effects were greatly increased. At the same time, thermoelectric applications became interesting also in other fields, including solid state refrigeration, electronics and optoelectronics, and devices for several applications, including in medical physics, and marine explorations.

A typical thermoelectric module is an array of n-type and p-type semiconducting materials connected electrically in series via a conductive metal and thermally in parallel between ceramics, as shown in Fig. 1.1.1. In n-type materials electrons are charge carriers, while in p-type materials holes are charge carriers. When heating one side of the module, the generated temperature gradient causes the carriers to diffuse

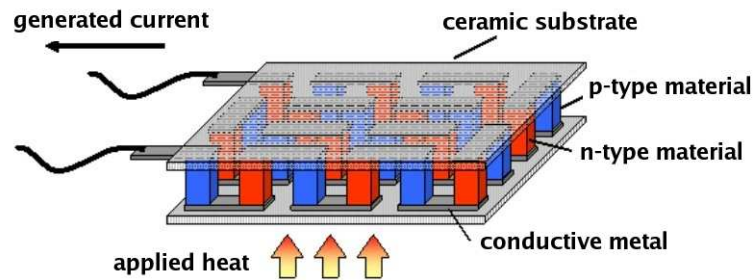


Figure 1.1.1: Schematic diagram of a typical thermoelectric module. Small legs of n-type(red) and p-type(blue) materials are connected in series by a conductive metal and then sandwiched between ceramic substrates.(Figure from Sigma-Aldrich Co. LLC.)

from the hot to the cold side, generating a thermoelectric voltage or thermoelectric electromotive force (EMF).

It can be shown [9] that the maximum efficiency (η_{MAX}) of thermoelectric devices is given by :

$$\eta_{MAX} = \left(\frac{T_H - T_C}{T_H} \right) \left(\frac{\sqrt{1 + ZT} - 1}{\sqrt{1 + ZT} + \frac{T_C}{T_H}} \right) \quad (1.1.1)$$

where T_H is the temperature at the hot side of the module, T_C is the temperature at the cold side, T is the average temperature between the hot and cold sides, and ZT is the material's figure of merit. At a desired working temperature, the efficiency of thermoelectric devices may be increased by increasing the value of ZT . However this is a very challenging task, since S , σ and κ are tightly interdependent and may not be independently controlled. Therefore, over the past decade, the efficiency of thermoelectric power generators has remained low compared to that of conventional generators (See Fig. 1.1.2).

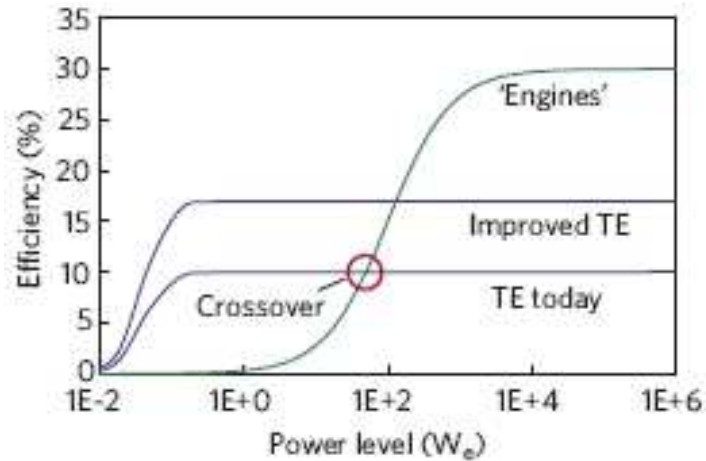


Figure 1.1.2: An illustrative plot of efficiency versus size for thermoelectrics (TE) and conventional steam engines (Figure from C. B. Vining, *Nature Mater.* vol. 8, p.83, 2009 [10]).

1.2 Thermoelectricity in semiconductor nanostructures

To be competitive compared with conventional refrigerators and generators, one must develop thermoelectric materials with $ZT > 3$ [11]. However, in the last five decades, the room-temperature ZT of bulk semiconductors has increased only from 0.6 to 1 [11]. In the last 10 years, theoretical and experimental investigations have showed that thermoelectric efficiency may be enhanced through nanostructural engineering [12, 13]. For examples, recent experiments [14, 15, 16] on $\text{Bi}_2\text{Te}_3\text{-Sb}_2\text{Te}_3$ and PbTe-PbSe films have shown that lattice thermal conductivity in nanostructured materials can be reduced to values as low as $0.2\text{-}0.5 \text{ W/m}^1\text{K}^{-1}$ [17, 18]. In addition, materials such as skutterudites, clathrates, half-Heuslers phases and novel oxides have received much attention. Fig. 1.2.1 shows the ZT values of Bi_2Te_3 and $\text{Si}_{1-x}\text{Ge}_x$ materials

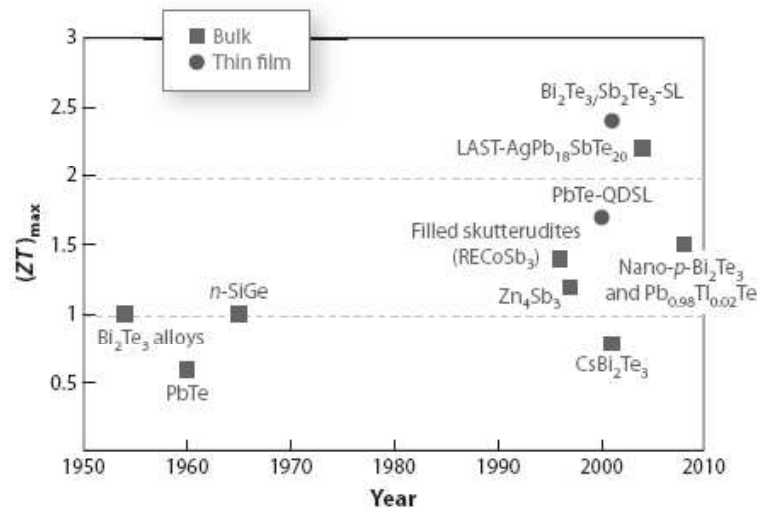


Figure 1.2.1: The figure of merit ZT , as a function of the time frame of several key TE materials relative to their discovery year, thus showing many of the recent advancements in both thin-film and bulk thermoelectric materials. Abbreviations: LAST, PbAgSbTe compounds; QDSL, quantum dot superlattice; SL, superlattice (Figure from Terry M. Tritt, *Annu. Rev. Mater. Res.* 2011. 41:433-48).

and of their more recently discovered nanocomposite forms, as well as the ZT values of several bulk and thin-film materials developed over the past several years.

As the basic constituent of semiconductor electronics, Silicon is one of the most studied materials of the last 50-60 years. It is Earth-abundant, cheap and non-toxic. Unfortunately, bulk crystalline silicon is not a good thermal-to-electrical energy converter, with $ZT = 0.01$ [17], and lattice thermal conductivity ≈ 150 W/mK [19] at room temperature. However, at the nanoscale, silicon thermoelectric properties can be greatly improved. For example, silicon wires [20] have been fabricated with κ up to 100 times smaller than that of crystalline silicon and $ZT = 0.6$. The thermal conductivity of nanomeshes [21] and porous membranes [22] has been made even smaller than those of nanowires for specific choices of the pore size and spacing, without degrading the electronic properties of crystalline silicon.

Even though both experimental and theoretical studies demonstrated that nanostructuring can significantly improve the value of ZT by reducing lattice thermal conductivity, the microscopic origin of the reduction of κ in nanostructured materials is poorly understood, and theoretical and computational techniques to study thermoelectric complex materials are not very well developed.

1.3 Motivation and outline of the thesis

In this dissertation, by using a series of equilibrium and non-equilibrium molecular dynamics simulations and lattice dynamics techniques to obtain approximate solutions of the Boltzmann Transport equation, we have studied heat transport in bulk and nanostructured Si and SiGe based materials. In particular we have explored the microscopic origin of the reduction of the thermal conductivity at the nanoscale, to understand design rules for the prediction of optimized thermoelectric materials.

The dissertation consists of five chapters. Chapter 1 contains a brief review of thermoelectricity in bulk materials and thermoelectricity in semiconductor nanostructures. Chapter 2 introduces the theoretical approaches for computing lattice thermal conductivity, including equilibrium molecular dynamics, non-equilibrium molecular dynamics, the Boltzmann transport equation and the Allen-Feldman theory. In Chapter 3, our study of heat transport in bulk ordered semiconductors is presented, including bulk crystalline silicon, bulk crystalline germanium and bulk crystalline silica (α -cristobalite). Chapter 4 describes our results on heat transport in bulk disordered materials, including amorphous silicon (structural disorder), silicon germanium alloys (mass disorder) and amorphous silica (structural disorder and local mass disorder). Chapter 5 discusses our findings on heat transport in nanostructured bulk materials, e.g. nanoporous silicon, and nanoporous silicon germanium.

Chapter 2

Theoretical approaches

2.1 Thermal conductivity

According to Fourier's law the thermal conductivity of a system is defined as the ratio of the heat current in the direction of heat flow (e.g. z direction) and the negative local temperature gradient ($-\frac{dT}{dz}$) along that direction:

$$J_z = -\kappa_z \frac{dT}{dz} \quad (2.1.1)$$

In solids heat may be transmitted via electrical carriers (electrons or holes), lattice vibrations (phonons), electromagnetic waves, spin waves, or other excitations. In metals electrons represent the majority of the heat carriers, while in insulators lattice vibrations are the dominant heat carriers. The total thermal conductivity (κ) can be written as a sum of all the components arising from various excitations [23]:

$$\kappa = \sum_n \kappa_n \quad (2.1.2)$$

where n denotes an excitation.

In this thesis we focused on semiconductors, and therefore we carried out calculations of the lattice thermal conductivity of a variety of materials, using equilibrium molecular dynamics (EMD), non-equilibrium molecular dynamics (NEMD), and the Boltzmann transport equation (BTE). The aim of this chapter is to review these methods and discuss the different approximations on which they rely upon.

2.2 Molecular dynamics simulations

Molecular dynamics (MD) is a computer simulation technique, in which classical Newton's equations of the motion of N particles interacting via a given potential are integrated by using numerical algorithms. Molecular dynamics may be used to simulate the microscopic properties of gases, solids and liquids: for *ergodic* systems one can show that the statistical ensemble averages are equal to the time averages [24]. Fig. 2.2.1 summarizes the basic steps of a molecular dynamics simulation.

To start a simulation, one needs to set up the initial positions and velocities of all particles in the system. The positions of particles may be chosen according to the experimental data. The initial velocities may be chosen e.g. according to a Gaussian distribution, and then scaled to the desired temperature : $\langle v_\alpha^2 \rangle = k_B T / m$, here $\langle v_\alpha \rangle$ is the α component of the velocity of a given particle, k_B is the Boltzmann constant, T is temperature, and m is the mass of the particles. In addition, the scaled values of velocities must be chosen in such a way as to guarantee that the total momentum of the system is conserved. The acceleration (\mathbf{a}_i) of particle i is calculated from the total force (\mathbf{F}_i) on the particle i by Newton's law : $\mathbf{F}_i = m_i \mathbf{a}_i$. The total force exerted on particle i can be obtained by the gradient of the total potential energy (W) of the system with respect to the position of the particle : $\mathbf{F}_i = -\Delta W(\mathbf{r}_i)$.

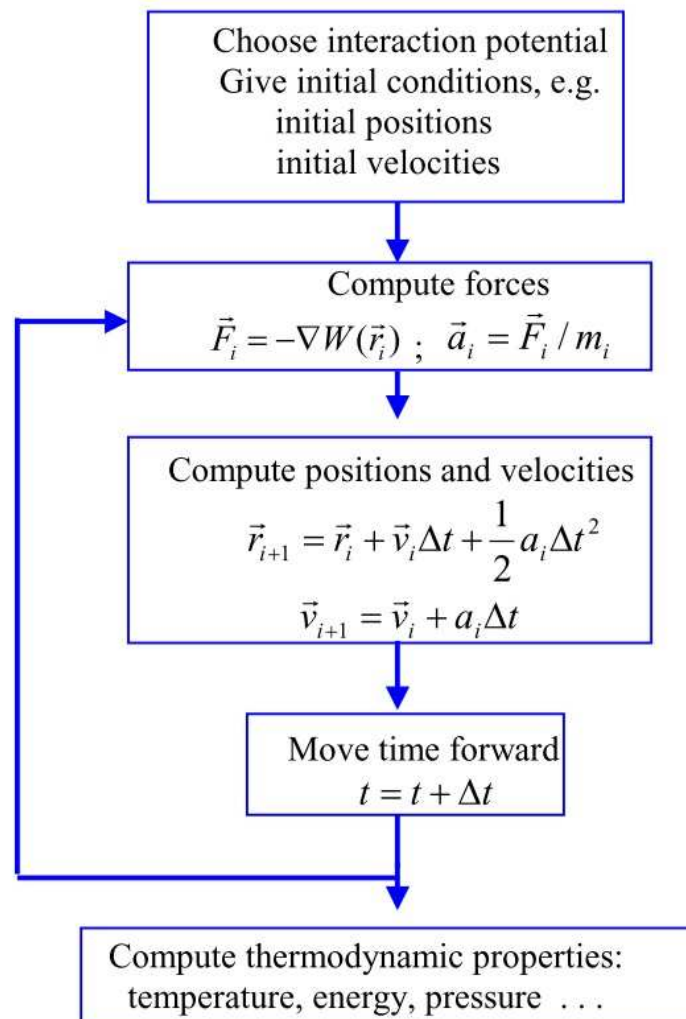


Figure 2.2.1: Simplified diagram of a molecular dynamics simulation. The simulation proceeds iteratively by solving the Newton's equations of motion of an N-particle system.

There are various integration algorithms used to solve the ordinary differential equations of an N particles system. The Verlet algorithm is one of the most widely used techniques. There are three forms of the Verlet algorithm: Verlet's original form, the leap-frog and the velocity Verlet algorithm. In the original form, positions at time $(t + \Delta t)$ can be predicted based on positions at time t ($\mathbf{r}(t)$), accelerations $\mathbf{a}(t)$, and previous positions $\mathbf{r}(t - \Delta t)$:

$$\mathbf{r}(t + \Delta t) = 2\mathbf{r}(t) - \mathbf{r}(t - \Delta t) + \Delta t^2 \mathbf{a}(t) \quad (2.2.1)$$

The velocities are obtained from the formula:

$$\mathbf{v}(t) = \frac{\mathbf{r}(t + \Delta t) - \mathbf{r}(t - \Delta t)}{2\Delta t} \quad (2.2.2)$$

The original Verlet form is simple, reversible in time, and allows one to conserve the linear momentum and energy within a simulation. However, it does not allow one to calculate the positions and velocities at the same time. Velocities can only be computed once $\mathbf{r}(t + \Delta t)$ is known. To tackle this deficiency, the basic Verlet scheme has been modified into the leap-frog [25] and the velocity [26] schemes. The leap-frog algorithm is defined as follows:

$$\mathbf{r}(t + \Delta t) = \mathbf{r}(t) + \Delta t \mathbf{v}(t + \frac{1}{2} \Delta t) \quad (2.2.3)$$

$$\mathbf{v}(t + \frac{1}{2} \Delta t) = \mathbf{v}(t - \frac{1}{2} \Delta t) + \Delta t \mathbf{a}(t) \quad (2.2.4)$$

The quantities stored in the memory in the course of a simulations are the current positions $\mathbf{r}(t)$ and accelerations $\mathbf{a}(t)$ together with the mid-step velocities $\mathbf{v}(t - \frac{1}{2} \Delta t)$.

The current velocities are computed by

$$\mathbf{v}(t) = \frac{1}{2}(\mathbf{v}(t + \frac{1}{2}\Delta t) + \mathbf{v}(t - \frac{1}{2}\Delta t)) \quad (2.2.5)$$

As Eq. 2.2.5 shows, the leap-frog algorithm does not yet handle the calculation of velocities in a completely satisfactory manner, since it only improves the calculation of velocities by half step. When using the velocity Verlet algorithm, one does store positions, velocities and accelerations all at the same time, and it takes the form:

$$\mathbf{r}(t + \Delta t) = \mathbf{r}(t) + \Delta t\mathbf{v}(t) + \frac{1}{2}\Delta t^2\mathbf{a}(t) \quad (2.2.6)$$

$$\mathbf{v}(t + \frac{1}{2}\Delta t) = \mathbf{v}(t) + \frac{1}{2}\Delta t\mathbf{a}(t) \quad (2.2.7)$$

$$\mathbf{v}(t + \Delta t) = \mathbf{v}(t + \frac{1}{2}\Delta t) + \frac{1}{2}\Delta t\mathbf{a}(t + \Delta t) \quad (2.2.8)$$

The new positions at time $(t + \Delta t)$ are calculated using Eq. 2.2.6, and the velocities at mid-step are computed using Eq. 2.2.7. After the forces and accelerations at time $(t + \Delta t)$ are evaluated, the velocities at time $t + \Delta t$ can be obtained using Eq. 2.2.8. In addition, kinetic energy, potential energy and other quantities of interest may be evaluated at this time. Therefore, the numerical stability, convenience, and simplicity of velocity Verlet make it perhaps the most widely used algorithm to date. The simulations in this thesis used the velocity Verlet integration algorithm.

In order to carry out a molecular dynamics simulation, it is essential to choose or determine the interatomic potential W , which in turn determines the forces between particles. For covalently bonded solids, such as silicon and germanium, there

are several proposed empirical potentials: Stillinger-Weber [27], Pearson et al. [28], environment dependent interatomic potential (EDIP) [29] and Tersoff potential [30]. The Tersoff potential has been used to study surface reconstructions and the phase diagram of silicon germanium alloys [31], and gave results consistent with several experiments [32]. In addition, the Tersoff potential describes accurately the properties of nontetrahedral forms of Si [33]. This potential has been employed for the heat transport calculations reported in this dissertation, and it is defined as:

$$W_{ij} = f_C(r_{ij})[f_R(r_{ij}) + b_{ij}f_A(r_{ij})] \quad (2.2.9)$$

$$f_R(r_{ij}) = A_{ij}exp(-\lambda_{ij}r_{ij}) \quad (2.2.10)$$

$$f_A(r_{ij}) = -B_{ij}exp(-\mu_{ij}r_{ij}) \quad (2.2.11)$$

$$f_C(r_{ij}) = \begin{cases} 1, & r_{ij} < R_{ij} \\ \frac{1}{2} + \frac{1}{2}\cos[\pi(r_{ij} - R_{ij})/(S_{ij} - R_{ij})], & R_{ij} < r_{ij} < S_{ij} \\ 0, & r_{ij} > S_{ij} \end{cases} \quad (2.2.12)$$

$$b_{ij} = \chi_{ij}(1 + \beta_i^{n_i} \zeta_{ij}^{n_i})^{-1/2n_i} \quad (2.2.13)$$

$$\zeta_{ij} = \sum_{k \neq i, j} f_C(r_{ik})\omega_{ik}g(\theta_{ijk}) \quad (2.2.14)$$

$$g(\theta_{ijk}) = 1 + c_i^2/d_i^2 - c_i^2/[d_i^2 + (h_i - \cos\theta_{ijk})^2] \quad (2.2.15)$$

$$\lambda_{ij} = (\lambda_i + \lambda_j)/2 \quad (2.2.16)$$

$$\mu_{ij} = (\mu_i + \mu_j)/2 \quad (2.2.17)$$

$$A_{ij} = (A_i A_j)^{1/2} \quad (2.2.18)$$

$$B_{ij} = (B_i B_j)^{1/2} \quad (2.2.19)$$

$$R_{ij} = (R_i R_j)^{1/2} \quad (2.2.20)$$

$$S_{ij} = (S_i S_j)^{1/2} \quad (2.2.21)$$

Here the indices i , j and k run over all atoms in the system, r_{ij} is the length of the ij bond, θ_{ijk} is the bond angle between bonds ij and ik . The repulsive pair potential $f_R(r_{ij})$ and the attractive pair potential $f_A(r_{ij})$ have a Morse potential form. f_C is a smooth potential cutoff function. The function b_{ij} accounts for the dependence of the potential on bonds' order. The Tersoff potential has eleven parameters determined by fitting to a set of physical properties obtained from experiments and ab initio calculations, including cohesive energy, bulk modulus and lattice constant. Tab. 2.2.1 and 2.2.2 give the parameters for Si, Ge and O used in this dissertation [30, 34].

To avoid surface effects (that in real experiments one avoids by using macroscopic samples), one uses periodic boundary conditions in MD simulations. A simulation box with a relatively small number of atoms is replicated throughout space to form

Table 2.2.1: Parameters entering the definition of the Tersoff empirical potential for silicon and germanium (Table from J. Tersoff, Phys. Rev. B, vol. 39, 5566 (1989) [30])

	Si	Ge
$A(eV)$	1.8308×10^3	1.769×10^3
$B(eV)$	4.7118×10^2	4.1923×10^2
$\lambda(\text{\AA}^{-1})$	2.4799	2.4451
$\mu(\text{\AA}^{-1})$	1.7322	1.7047
β	1.1000×10^{-6}	9.01666×10^{-7}
n	7.8734×10^{-1}	7.5627×10^{-1}
c	1.0039×10^5	1.0643×10^5
d	1.6217×10^1	1.5652×10^1
h	-5.9825×10^{-1}	-4.3884×10^{-1}
$R(\text{\AA})$	2.7	2.8
$S(\text{\AA})$	3.0	3.1
$\chi_{Si-Ge}=1.00061$		

Table 2.2.2: Parameters entering the definition of the Tersoff empirical potential for silicon and oxygen in silica (Table from S.Munetoh et al., Comput. Mater. Sci, vol. 39, 334 (2006) [34])

	Si	O
$A(eV)$	1.8308×10^3	1.88255×10^3
$B(eV)$	4.7118×10^2	2.18787×10^2
$\lambda(\text{\AA}^{-1})$	2.4799	4.17108
$\mu(\text{\AA}^{-1})$	1.7322	2.35692
β	1.1000×10^{-6}	1.1632×10^{-7}
n	7.8734×10^{-1}	1.04968
c	1.0039×10^5	6.46921×10^4
d	1.6217×10^1	4.11127
h	-5.9825×10^{-1}	-8.45922×10^{-1}
$R(\text{\AA})$	2.5	1.7
$S(\text{\AA})$	2.8	2.0
$\chi_{Si-O}=1.17945$		

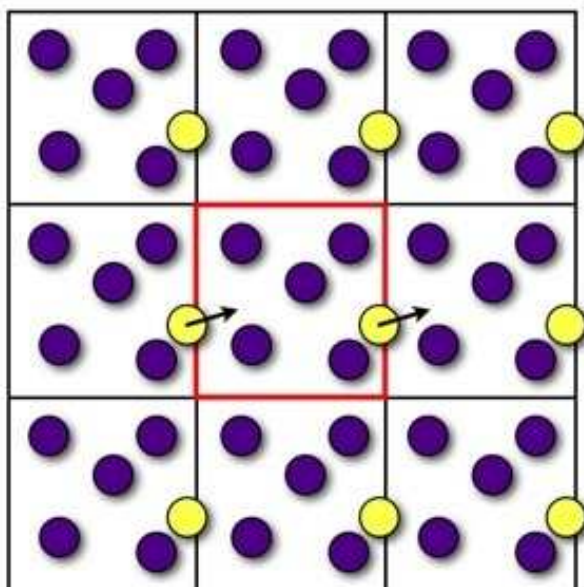


Figure 2.2.2: Schematic representation of a two-dimensional periodic system. Particles can enter and leave each box across each of the four edges. In a three-dimensional periodic system, particles would be free to cross any of the six edges. (Figure from <http://creativecommons.org/licenses/by-nc-sa/3.0/>)

an infinite lattice without any free surfaces. In the course of the simulation (See Fig. 2.2.2), as a particle moves in the original box, its periodic image in each of the neighboring boxes moves in, in exactly the same way. When a particle leaves the central box, one of its images will enter through neighboring units. Since the dynamics of atoms in the original box is exactly the same as that of atoms in the replicated boxes, it is not necessary to store the trajectories of all the images in a simulation, but only the coordinates of the particles in the central box are recorded. The properties of systems are then computed based on the coordinates of atoms in the central box only. The effects of a finite simulation domain on computed quantities have to be tested by increasing the size of the central box for each of the computed properties.

2.2.1 Equilibrium molecular dynamics

We now turn to the discussion of how MD is used to compute thermal conductivity. In a molecular dynamics simulation, considering a system at equilibrium within the microcanonical ensemble (NVE, where N is the number of atoms, V is the volume of system, and E is the total energy), the average heat flux is zero. The lattice thermal conductivity can be obtained from the variations of the instantaneous heat current using the Green-Kubo relation based on the fluctuation-dissipation theorem [35]:

$$\kappa_\alpha = \frac{V}{k_B T^2} \int_0^\infty \langle J_\alpha(t) J_\alpha(0) \rangle dt, \quad (2.2.22)$$

where k_B is the Boltzmann constant, V is the volume of the system, T is the temperature, and $\langle J_\alpha(t) J_\alpha(0) \rangle$ is the average heat current (\mathbf{J}) autocorrelation function (HCACF) along the α direction.

The heat current may be derived from local energy conservation:

$$\dot{\mathbf{H}} + \Delta \cdot \mathbf{J} = 0 \quad (2.2.23)$$

where \mathbf{H} is the Hamiltonian of the system, and Δ is the Laplace operator. Within the classical approximation, Eq. 2.2.23 becomes:

$$\frac{1}{V} \frac{\partial \epsilon(\mathbf{r}, t)}{\partial t} + \Delta \cdot \mathbf{J} = 0 \quad (2.2.24)$$

where $\epsilon(\mathbf{r}, t)$ is the instantaneous local energy density and \mathbf{J} is the instantaneous local heat current. Eq. 2.2.24 can be rewritten as:

$$\mathbf{J}(\mathbf{r}, t) = \frac{1}{V} \frac{d}{dt} \sum_i \mathbf{r}_i \epsilon_i \quad (2.2.25)$$

here \mathbf{r}_i is the position of atom i , and ϵ_i can be expressed as:

$$\epsilon_i = \frac{1}{2} m_i \mathbf{v}_i^2 + W_i \quad (2.2.26)$$

where \mathbf{v}_i and W_i are the velocity vector and the local potential energy assigned to atom i , respectively. For a many body interaction potential, such as the Tersoff potential, the heat current can then be expressed as follows [36].

$$\mathbf{J} = \frac{1}{V} \left[\sum_i^N \epsilon_i \mathbf{v}_i + \frac{1}{2} \sum_{i,j;i \neq j}^N (\mathbf{F}_{ij} \cdot \mathbf{v}_i) \mathbf{r}_{ij} + \frac{1}{6} \sum_{i,j,k;i \neq j \neq k}^N (\mathbf{F}_{ijk} \cdot \mathbf{v}_i) (\mathbf{r}_{ij} + \mathbf{r}_{ik}) \right], \quad (2.2.27)$$

Equivalently, the heat current can also be calculated from the following expression:

$$\mathbf{J} = \frac{1}{V} \left[\sum_i^N \epsilon_i \mathbf{v}_i - \sum_i^N \mathbf{S}_i \cdot \mathbf{v}_i \right] \quad (2.2.28)$$

\mathbf{S}_i is 3×3 atomic stress tensor, given by:

$$S_{i,\alpha\beta} = -m_i v_{i,\alpha} v_{i,\beta} - \frac{1}{2} \sum_j^N (r_{i,\alpha} F'_{ij,\beta} + r_{j,\alpha} F'_{ij,\beta}) \quad (2.2.29)$$

The first term of the right hand side is the kinetic energy contribution from atom i . The second term is the potential energy contribution. $r_{i,\alpha}$ and $r_{j,\alpha}$ are the projection of the positions of atom i and j on the α direction. $F'_{ij,\beta}$ is the β component of the interatomic many-body force. In this work, molecular dynamics was used to obtain the coordinates, velocities, forces and stress tensors needed to compute the heat current (Eq. 2.2.27).

In analogy with the calculation of diffusion coefficients in Brownian motion theory [37], the thermal conductivity can also be computed from equilibrium molecular dynamics simulations by fitting the mean square displacement \mathbf{R} of the integrated heat current by an Einstein type relation [38]:

$$\langle (R_\alpha(t) - R_\alpha(0))^2 \rangle = 2k_B T^2 V \kappa_\alpha [t + \tau(e^{-t/\tau} - 1)] \quad (2.2.30)$$

where R_α is the integrated heat current \mathbf{R} along the α direction. τ provides a rough estimate of the average ballistic propagation time.

2.2.2 Non-equilibrium molecular dynamics

The thermal conductivity can also be computed using non-equilibrium molecular dynamics (NEMD). We implemented an NEMD method based on the approach proposed by Plathe [39]. According to Fourier's law, in an isotropic system, the thermal conductivity κ in the heat propagation direction e.g. the z direction, is defined by the following formula:

$$\kappa = \lim_{\partial T/\partial z \rightarrow 0} \lim_{t \rightarrow \infty} -\frac{\langle J_z(t) \rangle}{\partial T/\partial z} \quad (2.2.31)$$

Instead of computing the heat flux, the strategy here is to impose a well defined heat flux on the system and then measure the resulting temperature gradient. In order to obtain the temperature gradient, the simulation box is divided into N_s equal slabs perpendicular to the z direction (see Fig. 2.2.3). Slab 0 is defined as the 'hot' slab and slabs $N_s/2$ and $-N_s/2$ as the 'cold' slabs. The artificial heat flux is generated by interchanging the kinetic energy of the hottest atom in the cold slab and the kinetic energy of the coldest atom in the hot slab so that the temperature decreases in the cool slab and increases in the hot slab. The simulation cell is periodically replicated. The instantaneous local temperature T_k in the slab k is given by:

$$T_k = \frac{1}{3n_k k_B} \sum_{i \in k}^{n_k} m_i v_i^2 \quad (2.2.32)$$

where n_k is the number of atoms in the slab k , m_i and v_i are the mass and velocity of atom i , respectively. A temperature profile is then calculated by computing an average T_k . A temperature gradient $\partial T/\partial z$ is obtained by the slope of the least-square fit of the temperature profile. As the transferred kinetic energy is balanced by the thermal energy in the opposite direction caused by the temperature difference

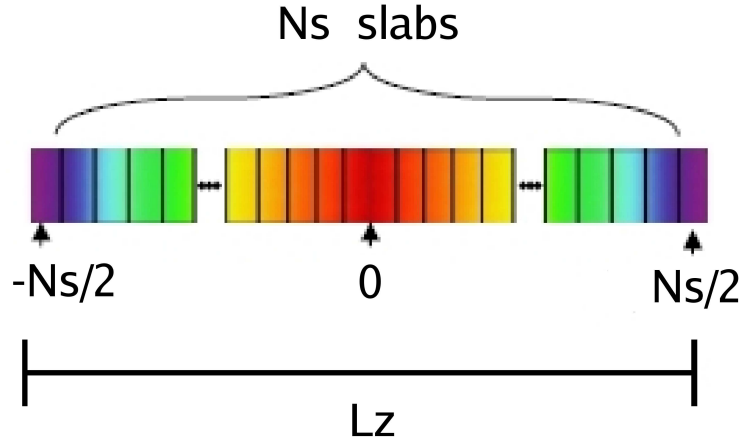


Figure 2.2.3: Periodic simulation cell composed of N_s slices used in non-equilibrium MD simulations. Slab 0 is the 'hot' slab, slab $N_s/2$ and $-N_s/2$ are 'cold' slabs. Thermal energy flows through the system as indicated by the colors. The red color represents the hottest region while the blue color represents the coldest region.

between the cold and hot slabs, the system reaches a steady state. The imposed heat flux is given exactly by the kinetic energy transferred during the simulation:

$$J_z = -\frac{\sum_{transfers} \frac{m}{2}(v_h^2 - v_c^2)}{2tL_xL_y} \quad (2.2.33)$$

where t is the simulation time, v_h is the velocity of the hottest atom in the cold slab, v_c is the velocity of the coldest atom in the hot slab, L_x and L_y are the box length in x and y directions, respectively. The factor 2 in the denominator arises from the fact that thermal energy flows in two directions from the middle of slab 0.

2.3 Boltzmann transport equation

An alternative way to compute the thermal conductivity is provided by the approximate solutions of the Boltzmann transport equation (BTE). The approximate

solutions used in this thesis are based on lattice dynamics which we introduce in the next section before discussing the BTE.

2.3.1 Lattice dynamics

Using the harmonic approximation, the energy of a crystal within the Born-Oppenheimer (BO) approximation [40] can be written as [41]:

$$E^{harm} = \frac{1}{2} \sum_{jj', ll'} \sum_{\alpha\beta} u_{\alpha}(jl) \Phi_{\alpha\beta} u_{\beta}(j'l') \quad (2.3.1)$$

where j and j' are the indexes of atoms, l and l' are the indexes of unit cells, and α and β are the indexes of dimensions. The vector $\mathbf{u}(jl)$ is:

$$\mathbf{u}(jl) = \begin{pmatrix} u_x(jl) \\ u_y(jl) \\ u_z(jl) \end{pmatrix} \quad (2.3.2)$$

and the force constant matrix Φ is a 3×3 matrix, with elements:

$$\Phi_{\alpha\beta} \begin{pmatrix} jj' \\ ll' \end{pmatrix} = \frac{\partial^2 W}{\partial u_{\alpha}(jl) \partial u_{\beta}(j'l')} \quad (2.3.3)$$

In the general case, the equation of motion for the j th atom in the l th unit cell is given by:

$$m_j \ddot{\mathbf{u}}(jl, t) = - \sum_{j'l'} \Phi \begin{pmatrix} jj' \\ ll' \end{pmatrix} \cdot \mathbf{u}(j'l', t) \quad (2.3.4)$$

where m_j is the mass of the j th atom. The solution for $\mathbf{u}(jl, t)$ is a linear superposition of traveling harmonic waves with different wave vector \mathbf{k} and mode label ν :

$$\mathbf{u}(jl, t) = \sum_{\mathbf{k}, \nu} \mathbf{U}(j, \mathbf{k}, \nu) \exp(i[\mathbf{k} \cdot \mathbf{r}(jl) - \omega(\mathbf{k}, \nu)t]) \quad (2.3.5)$$

where $\mathbf{r}(jl)$ is the position of the atom (jl), $\mathbf{U}(j, \mathbf{k}, \nu)$ is the displacement vector of atom j in the reciprocal space. Substituting the wave Eq. 2.3.5 into the Eq. 2.3.4 gives:

$$m_j \omega^2(\mathbf{k}, \nu) \mathbf{U}(j, \mathbf{k}, \nu) = \sum_{j'l'} \Phi \begin{pmatrix} jj' \\ 0l' \end{pmatrix} \cdot \mathbf{U}(j', \mathbf{k}, \nu) \exp(i\mathbf{k} \cdot [\mathbf{r}(j'l') - \mathbf{r}(j0)]) \quad (2.3.6)$$

here the reference atom is in the unit cell $l = 0$. The equations of motion for a single solution can be expressed in vector form:

$$\omega^2(\mathbf{k}, \nu) \mathbf{e}(\mathbf{k}, \nu) = \mathbf{\Omega}(\mathbf{k}) \cdot \mathbf{e}(\mathbf{k}, \nu) \quad (2.3.7)$$

The column vector $\mathbf{e}(\mathbf{k}, \nu)$ is composed of the displacement vector \mathbf{U} weighted by the square root of the atomic mass, so that it has $3n$ elements (n is the number of

atoms per unit cell):

$$\mathbf{e}(\mathbf{k}, \nu) = \begin{pmatrix} \sqrt{m_1} U_x(1, \mathbf{k}, \nu) \\ \sqrt{m_1} U_y(1, \mathbf{k}, \nu) \\ \sqrt{m_1} U_z(1, \mathbf{k}, \nu) \\ \sqrt{m_2} U_x(2, \mathbf{k}, \nu) \\ \cdot \\ \cdot \\ \cdot \\ \sqrt{m_n} U_z(n, \mathbf{k}, \nu) \end{pmatrix} \quad (2.3.8)$$

We define the dynamical matrix $\mathbf{\Omega}(\mathbf{k})$ as the $3n \times 3n$ matrix with elements given by:

$$\Omega_{\alpha\beta}(jj', \mathbf{k}) = \frac{1}{\sqrt{m_j m_{j'}}} \sum_{l'} \Phi_{\alpha\beta} \begin{pmatrix} jj' \\ 0l' \end{pmatrix} \exp(i\mathbf{k} \cdot [\mathbf{r}(j'l') - \mathbf{r}(j0)]) \quad (2.3.9)$$

where $l = 0$ labels the reference unit cell.

Since $\mathbf{e}(\mathbf{k}, \nu)$ has $3n$ components, there are $3n$ solutions corresponding to the $3n$ branches in the dispersion diagram. Defining the frequency matrix $\mathbf{\Xi}(\mathbf{k})$ as the diagonal matrix of the squares of the angular frequencies, the general displacement

equations assume a compact form:

$$\Xi(\mathbf{k}) = \begin{pmatrix} \omega^2(\mathbf{k}, 1) & & & & & \\ & \omega^2(\mathbf{k}, 2) & & & & \\ & & \omega^2(\mathbf{k}, 3) & & & \\ & & & \ddots & & \\ & & & & \ddots & \\ & & & & & \omega^2(\mathbf{k}, 3n) \end{pmatrix} \quad (2.3.10)$$

$$\mathbf{e}(\mathbf{k}) \cdot \Xi(\mathbf{k}) = \Omega(\mathbf{k}) \cdot \mathbf{e}(\mathbf{k}) \quad (2.3.11)$$

The dynamical matrix is *Hermitian*,

$$\Omega(\mathbf{k}) = (\Omega^*(\mathbf{k}))^T \quad (2.3.12)$$

The eigenvalues of a Hermitian matrix are real, and the eigenvectors satisfy the following orthonormality and completeness relations:

$$(\mathbf{e}(\mathbf{k}))^T \cdot (\mathbf{e}(\mathbf{k}))^* = (\mathbf{e}(\mathbf{k}))^T \cdot \mathbf{e}(-\mathbf{k}) = 1 \quad (2.3.13)$$

$$(\mathbf{e}(\mathbf{k}, \nu))^T \cdot \mathbf{e}(-\mathbf{k}, \nu') = \delta_{\nu\nu'} \quad (2.3.14)$$

We will compute and diagonalize dynamical matrices in the evaluation of approximate solutions of the BTE, which we discuss next.

2.3.2 Approximate solutions for ordered systems

At the end of the nineteenth century, Boltzmann introduced a dynamical equation for the distribution function of rarefied gases:

$$\frac{\partial f}{\partial t} + v \cdot \frac{\partial f}{\partial r} + \frac{F}{m} \cdot \frac{\partial f}{\partial v} = \left(\frac{\partial f}{\partial t}\right)_{coll}. \quad (2.3.15)$$

The right-hand side expresses the variation per unit time of the distribution function $f(r, v, t)$ due to collisions. When out of equilibrium, a gas evolves toward an equilibrium state due to collisions. The nonlinear collision term in Eq. 2.3.15 is usually very difficult to explicitly compute. One may give a rough approximation of this term based on the so-called relaxation time model.

$$\left(\frac{\partial f}{\partial t}\right)_{coll} \simeq -\frac{f - f^{(0)}}{\tau} \quad (2.3.16)$$

here τ is a relaxation time which the system takes to return to equilibrium, $f^{(0)}$ is the equilibrium distribution function of the system. In the stationary regime, and without external fields, the Boltzmann equation in the relaxation time approximation leads to :

$$v \cdot \Delta_r f = -\frac{f - f^{(0)}}{\tau} \quad (2.3.17)$$

where v is the group velocity ($v = \frac{d\omega}{dk}$, where ω is the frequency defined in the previous section).

One may seek a solution of the BTE by using perturbation theory and a distribution function of the form:

$$f = f^{(0)} + \lambda \cdot f^{(1)} + \lambda^2 \cdot f^{(2)} + \dots \quad (2.3.18)$$

where λ is an expansion parameter. For small deviations from equilibrium, Eq. 2.3.18 can be rewritten as:

$$f = f^{(0)} + \delta f^{(0)} \quad (2.3.19)$$

here $\delta f^{(0)}$ is a small variation with respect to the equilibrium distribution $f^{(0)}$. Substituting Eq. 2.3.19 into Eq. 2.3.17, one finds:

$$\delta f^{(0)} = -\tau \frac{\partial f^{(0)}}{\partial T} v \cdot \Delta_r T \quad (2.3.20)$$

We now consider the phonons in a solid as a gas satisfying the Bose-Einstein statistics, and we use Eq. 2.3.20 to describe the deviations from equilibrium of the phonon distribution in the presence of a temperature gradient in the system.

Using a normal mode representation of the system vibrations described in Chapter 2.3.1, the heat flux, giving rise to the perturbation $\delta f^{(0)}$ (Eq. 2.3.19), is:

$$J = \sum_s \int_{BZ} \frac{d^3k}{8\pi^3} (\delta f^{(0)} + \frac{1}{2}) \hbar \omega_{k,s} \Delta_k \omega_s \quad (2.3.21)$$

Substituting Eq. 2.3.20 into Eq. 2.3.21, and using Fourier's law yields an expression of the thermal conductivity. Since $\Delta_k \omega_s$ is equal to the group velocity v , ignoring the zero energy contribution and assuming to consider an isotropic system, the lattice thermal conductivity κ is:

$$\kappa = \frac{1}{3} \sum_s \int_{BZ} \frac{d^3k}{8\pi^3} \tau v_{k,s}^2 \frac{\partial f^{(0)}}{\partial T} \hbar \omega_{k,s} \quad (2.3.22)$$

here, $v_{k,s}^2 = v_{x;k,s}^2 + v_{y;k,s}^2 + v_{z;k,s}^2$ ($v_{x;k,s} = v_{y;k,s} = v_{z;k,s}$). Rewriting Eq. 2.3.22 in the

single mode relaxation time approximation, yields:

$$\kappa_i = \frac{1}{3} \tau_i v_i^2 \frac{\partial f_i^{(0)}}{\partial T} \hbar \omega_i \quad (2.3.23)$$

The specific heat capacity per volume contributed by a mode i is:

$$c_{i,V} = \frac{\partial f_i^{(0)}}{\partial T} \hbar \omega_i \quad (2.3.24)$$

and Eq. 2.3.23 becomes:

$$\kappa_i = \frac{1}{3} \tau_i v_i^2 c_{i,V} \quad (2.3.25)$$

The total thermal conductivity is the sum of each mode's contribution:

$$\kappa = \frac{1}{3} \sum_i \tau_i v_i^2 c_{i,V} \quad (2.3.26)$$

Where v_i and τ_i are the group velocity and lifetime of mode i .

In our work we have used lattice dynamics to obtain the group velocities from phonon dispersion curves; we have computed the lifetimes from the normalized autocorrelation function of eigenmode energy ($E_i(\mathbf{q}, t)$) [42] using molecular dynamics:

$$\tau_i = \int_0^\infty \frac{\langle E_i(\mathbf{q}, t) E_i(\mathbf{q}, t) \rangle}{\langle E_i(\mathbf{q}, 0) E_i(\mathbf{q}, 0) \rangle} \quad (2.3.27)$$

$$E_i(\mathbf{q}, t) = \frac{\omega_i^2 S_i^*(\mathbf{q}, t) S_i(\mathbf{q}, t)}{2} + \frac{S_i'^*(\mathbf{q}, t) S_i'(\mathbf{q}, t)}{2} \quad (2.3.28)$$

$$S_i(\mathbf{q}, t) = \sqrt{N} \sum_j \sqrt{M_j} e^{-i\mathbf{q} \cdot \mathbf{r}_{j,0}} e_i^*(\mathbf{q}) \cdot \mathbf{u}_j(t) \quad (2.3.29)$$

where, S' is the time derivative of S , and \mathbf{u}_j is the displacement vector of atom j .

The validity of the Boltzmann transport equation depends on the characteristic length scales in the system. We define the characteristic length scale (i.e. the size of the system or the size of grain boundaries in the system) as L , and we introduce it into the Eq. 2.3.17, we obtain:

$$\frac{v}{L}v^* \cdot \frac{\partial f}{\partial r^*} = -\frac{f - f^{(0)}}{\tau} \quad (2.3.30)$$

Here the quantities marked with an asterisk are all dimensionless. By substituting Eq. 2.3.18 into Eq. 2.3.30 and keeping only the first order terms in λ , one has:

$$\frac{v}{L}v^* \cdot \frac{f^{(1)}}{\partial r^*} = -\frac{\lambda}{\tau}f^{(1)} \quad (2.3.31)$$

One can see that the variation of f is driven by the dimensionless number $\lambda = \frac{v\tau}{L} = \frac{l}{L}$, where l is the mean free path of the system vibrations.

Depending on the value of λ , we may identify three heat transport regimes:

- (1) if $\lambda \ll 1$, the regime is diffusive. The system is close to local thermodynamic equilibrium, and perturbation theory under linear response can be used to seek a solution.
- (2) if $\lambda \gg 1$, the regime is ballistic. In this regime, the particles are scattered mainly by the system boundaries, not by collisions. Perturbation theory may not be used.
- (3) if $\lambda \sim 1$, the regime is semi-ballistic. It is an intermediate regime in which it is very difficult to simplify the Boltzmann transport equation. In principle one should seek a solution of the full equation. Perturbation theory can not be used.

2.3.3 Approximate solutions for disordered systems

Eq. 2.3.26 is valid for propagating modes. The typical mean free path of phonons may become so short that its wavelength and even the mean free path itself are no longer well defined; in other words, not all modes are propagating in a disordered system. Allen and Feldman proposed an alternative theory for calculating the thermal conductivity of disordered materials [43] and to take into account heat transport by non-propagating modes. Assuming the dominant scattering is correctly described by a harmonic Hamiltonian, a Kubo formula is derived by using off-diagonal elements of the heat current operator. In the harmonic approximation, the heat current operator is:

$$\mathbf{S} = \frac{1}{2V} \sum_{l,m} \sum_{\alpha,\beta} (\mathbf{R}_l - \mathbf{R}_m) \frac{p_{l\alpha}}{m_l} \frac{\partial^2 W}{\partial u(l\alpha) \partial u(m\beta)} u(m\beta) \quad (2.3.32)$$

where V is the volume of system. W is the potential energy of the system. l and m are the indexes of atoms. α and β are the indexes of dimensions. \mathbf{R} is the position of atoms. $p_{l\alpha}$ is the momentum of atom l in α direction. $u_{m\beta}$ is the displacement of atom m along β direction.

Now considering a periodic system of N cells, with n atoms per cell, labeled by $b = 1, 2 \dots, n$:

$$\mathbf{S} = -\frac{1}{2V} \sum_{l,m} \sum_{b,b'=1}^n \sum_{\alpha,\beta=1}^3 (\mathbf{R}_{lb} - \mathbf{R}_{mb'}) \times \frac{p_{lb\alpha}}{m_b} \Phi_{\alpha\beta}^{bb'}(0, m-l) u_{mb'\beta} \quad (2.3.33)$$

where l and m are the index of the cell; $\Phi^{bb'}(0, m-l)$ is the force constant tensor

between atoms lb and mb' . In the normal mode coordinates:

$$u_{lb\alpha} = \frac{1}{\sqrt{m_b}} \sum_j e_\alpha(b; \mathbf{k}, j) \mathbf{Q}(\mathbf{k}, j) e^{i\mathbf{k} \cdot \mathbf{R}_l} \quad (2.3.34)$$

$$p_{lb\alpha} = \sqrt{m_b} \sum_j e_\alpha(b, \mathbf{k}, j) \mathbf{P}(\mathbf{k}, j) e^{i\mathbf{k} \cdot \mathbf{R}_l} \quad (2.3.35)$$

here $\mathbf{Q}(\mathbf{k}, j)$ and $\mathbf{P}(\mathbf{k}, j)$ are the position and momentum of vibrational mode with the band branch of j and wave vector \mathbf{k} , written in the terms of mode creation and annihilation operators [44]:

$$\mathbf{Q}(\mathbf{k}, j) = -i \sqrt{\frac{\hbar}{2\omega(\mathbf{k}, j)}} (a^\dagger(\mathbf{k}, j) - a(-\mathbf{k}, j)) \quad (2.3.36)$$

$$\mathbf{P}(\mathbf{k}, j) = \sqrt{\frac{\hbar\omega(\mathbf{k}, j)}{2}} (a(\mathbf{k}, j) + a^\dagger(-\mathbf{k}, j)) \quad (2.3.37)$$

Substituting these expressions into Eq. 2.3.33 gives:

$$\begin{aligned} \mathbf{S} = & -\frac{1}{2V} \sum_{j,j'} \sum_{\alpha\beta} \sum_{m,b,b'} \mathbf{P}(\mathbf{k}, j) \mathbf{Q}(-\mathbf{k}, j') e_\alpha(b; \mathbf{k}, j) \\ & \times e_\beta(b'; \mathbf{k}, j') \Omega_{\beta\alpha}^{b'b}(0, m) \\ & \times (\mathbf{R}_m + \mathbf{R}_{bb'}) e^{i\mathbf{k} \cdot \mathbf{R}_m} \end{aligned} \quad (2.3.38)$$

$\Omega_{\alpha\beta}^{k'k}(0, m)$ are mass-scaled elements of the force constants matrix Φ , namely:

$$\Omega_{\alpha\beta}^{bb'}(0, m) = \sqrt{m_b m_{b'}} \Phi_{\alpha\beta}^{bb'}(0, m) \quad (2.3.39)$$

Eq. 2.3.38 can be written in terms of mode creation and annihilation operators:

$$\mathbf{S} = \sum_{i,j} \mathbf{S}_{ij} a_i^\dagger a_j \quad (2.3.40)$$

$$\mathbf{S}_{ij} = \frac{\hbar}{2V} \mathbf{v}_{\mathbf{k},ij} (\omega_{\mathbf{k},i} + \omega_{\mathbf{k},j}) \quad (2.3.41)$$

$$\begin{aligned} \mathbf{v}_{\mathbf{k},ij} = \frac{i}{2\sqrt{\omega_{\mathbf{k},i}\omega_{\mathbf{k},j}}} \sum_{\alpha\beta} \sum_{m,b,b'} e_\alpha(b; \mathbf{k}, i) \Omega_{\beta\alpha}^{b'b}(0, m) \\ \times (\mathbf{R}_m + \mathbf{R}_{bb'}) e^{i\mathbf{k}\cdot\mathbf{R}_m} \\ \times e_\beta(b; \mathbf{k}, j) \end{aligned} \quad (2.3.42)$$

Eq. 2.3.41 defines the matrix elements S_{ij} of the heat current operator \mathbf{S} . It is then used to compute a microscopic, temperature-independent quantity, a “mode diffusivity” D_i :

$$D_i = \frac{\pi V^2}{3\hbar^2 \omega_i^2} \sum_{j \neq i} |\mathbf{S}_{ij}|^2 \delta(\omega_i - \omega_j) \quad (2.3.43)$$

The δ function may be described as a Lorentzian function:

$$\delta(\omega_i - \omega_j) = \frac{1}{\pi} \frac{\eta}{(\omega_i - \omega_j)^2 + \eta^2} \quad (2.3.44)$$

Where η is the Lorentzian width, specifying half width at the half-maximum.

The thermal conductivity of disordered systems can then be calculated from the

Table 2.4.1: Ability of the techniques used in this thesis in describing disorder, anharmonicity and in including the proper phonon statistics (Bose-Einstein) in the calculations of thermal conductivity. EMD and NEMD denote equilibrium and non-equilibrium molecular dynamics, respectively. BTE denotes solutions of the Boltzmann Transport Equation in the relaxation time approximation.

Physical Effect	EMD	NEMD	BTE
disorder	yes	yes	no
anharmonicity	yes	yes	approximate
Bose-Einstein	no	no	yes

diffusivity :

$$\kappa = \frac{1}{V} \sum_i c_{i,V}(T) D_i \quad (2.3.45)$$

here $c_{i,V}$ is the specific heat per volume contributed from mode i .

2.4 Summary

In the next chapters, we use the concepts and formulas described here to compute the thermal conductivity of ordered, disordered and nanostructured semiconducting systems. Tab. 2.4.1 shows a summary of the methods used in this thesis.

Equilibrium molecular dynamics simulations (EMD) were carried out with two codes: DLPOLY [45] and LAMMPS [46]. The calculation of the thermal conductivity in DLPOLY was developed by Dr. Davide Donadio, and it was used to study heat transport in small bulk systems ($< 10,000$ atoms). The author implemented the non-equilibrium molecular dynamics (NEMD) method in DLPOLY described in Chapter 2.2.2. The NEMD was used to study the thermal conductivity of crystalline Si film and of amorphous Si film.

Chapter 3

Heat transport in ordered bulk materials

3.1 Background and objectives

Before presenting the results of our simulations of Si, Ge and SiO₂, we summarize the existing experimental and theoretical results for these systems.

3.1.1 Silicon

Bulk crystalline silicon (c-Si) is not a good candidate material for thermoelectric power generation, due to its large lattice thermal conductivity, even though it has a larger Seebeck coefficient (few hundreds $\mu V/K$) than metals (few $\mu V/K$). Recent experimental and theoretical studies have showed that nanostructuring can enhance the thermoelectric efficiency of Si-based materials by reducing the lattice thermal conductivity without degrading the electronic properties [20, 21]. Since Si is a Earth abundant, cheap and nontoxic material, if nanostructuring may improve

the ZT, Si may then become a good candidate for thermoelectric applications. At room temperature, heat transport in silicon is mainly dominated by lattice vibrations (phonons) [47], and thus a quantity of interest is the lattice thermal conductivity.

The earliest value of κ of c-Si was reported by Koenigsberger and Weiss in 1911 [48] who found 84 W/mK at 290°K for a natural sample (92.23% ^{28}Si , 4.67% ^{29}Si and 3.1% ^{30}Si). Later Stuckes [49], Morris and Hust [50], Shanks et al. [51] and Glassbrenner and Slack [47] all measured the κ of natural Si by employing different techniques (see Tab.3.1.1). The measured value of κ was found to be 130~150 W/mK. In 1997, Capinski et al. [19] used an optical pump-and-probe technique to measure the κ of isotopically pure Si. The sample was made from 99.7% ^{28}Si and obtained by liquid phase epitaxy. They found $\sim 60\%$ increase in κ of isotopically pure silicon compared to that of the natural samples at 300K. Later Ruf et al. [52] re-measured the κ of highly enriched ^{28}Si (99.8588%) by means of a steady-state heat flow technique. They obtained a result consistent with that of Capinski [19] at room temperature. In 2004, Kremer and co-authors [53] measured the κ of isotopically enriched ^{28}Si independently in three laboratories on a total of four samples of different shape and degree of isotope enrichment. They claimed that the results in the different laboratories were in good agreement with each other. They indicated that at room temperature the thermal conductivity of isotopically enriched ^{28}Si exceeds the thermal conductivity of natural Si by $\sim 10 \pm 2\%$, but not $\sim 60\%$. This finding is in disagreement with the earlier reports from Capinski [19]. As of yet no complete consensus has been reached about the measured value of κ of isotopically enriched ^{28}Si .

On the theoretical side, the κ of c-Si was first computed by Volz and Chen [36] in 2000. By using direct integration of the heat current autocorrelation function obtained from the Green-Kubo formula, they computed κ using the Stillinger-Weber

(SW) potential [27] in equilibrium molecular dynamics simulations. They found a strong size-dependence of the computed κ . For example, the calculated κ at 500K could not be converged even when using cells with 8000 atoms. To obtain a converged value, they employed the spectral Green-Kubo formula with a model-based extrapolation. The fitted results at 300K are about 70% higher than the measured thermal conductivity of natural Si (150 W/mK) [47], but correspond very well to the experimental results for ^{28}Si [52](237 W/mK). However, using the same empirical potential (SW), several authors (e.g. Schelling [51]g et al. [54], Sellan et al. [55] and Goicochea et al. [56]) later reported that there is only a weak domain size effect on κ of c-Si. Schelling reported that the value of κ (≈ 66 W/mK at 1000K) can be obtained by performing EMD with only 1728 atoms. Goicochea showed that the value of κ of c-Si at 300 K was about 350 W/mK by using a system with 512 atoms. This result is 48 % higher than the measured thermal conductivity of enriched ^{28}Si (237 W/mK). A specific study of domain size effects on κ of c-Si was reported by Sun and Murthy [57]. Using the environment dependent interatomic potential (EDIP) [29], here authors claimed that a converged value of κ could be obtained using a small system with 216 atoms. Tab. 3.1.1 summarizes the values of κ of c-Si obtained from both experimental measurements and theoretical calculations using different empirical potentials.

To the best of our knowledge, there is no study of κ of c-Si using Tersoff potential [31]. By calculating κ using the full solution of the BTE with three different empirical potentials: Tersoff, Stillinger-Weber (SW) and EDIP, Broido et al. [58] showed that Tersoff may be a relatively accurate potential for the study of heat transport in silicon.

In this dissertation we employed the Tersoff potential to compute the κ of c-Si and compared the results with those obtained from other potential models and

Table 3.1.1: Experimental and theoretical values of κ of c-Si obtained by EMD, reported in the recent literature at 300K. (Natural Si: $\bar{m}=28$, $^{28}\text{Si}=92.23\%$, $^{29}\text{Si}=4.67\%$, $^{30}\text{Si}=3.10\%$)

Experimental method	κ (W/mK)	Sample	Ref.
	~ 84	natural	[48]
Absolute, steady-state, radial heat flow	~ 130	natural	[49]
Absolute, steady-state, radial heat flow	~ 130	natural	[50]
Variable state, thermal diffusivity	~ 142	natural	[51]
Absolute, steady-state, radial heat flow	~ 156	natural	[47]
Optical pump-and-probe technique	~ 240	^{28}Si	[19]
Absolute, steady-state, radial heat	~ 240	^{28}Si	[52]
Absolute, steady-state, radial heat	~ 165	^{28}Si	[53]
Empirical potential	κ (W/mK)	number of atoms	Ref.
Stillinger-Weber	~ 255	8000	[36]
Stillinger-Weber	~ 350	512	[56]
Environment dependent interatomic potential	~ 170	216	[57]

experiments. We also carried out extensive convergence studies using MD cells with million of atoms.

3.1.2 Germanium

In order to gain insight into the heat transport in silicon germanium alloys (see Chapter 4), and to generate reference results, the thermal conductivity of bulk crystalline germanium (c-Ge) has also been studied in this dissertation. The measured values of the κ of natural c-Ge (35.94 % ^{74}Ge , 27.66% ^{72}Ge , 21.23% ^{70}Ge , 7.73% ^{73}Ge and 7.44% ^{76}Ge) are about 50 \sim 60 W/mK [59, 60, 47] at room temperature. The measured κ of enriched ^{70}Ge is 78 W/mK at 300K [19] [19] (See Tab. 3.1.2). There is only one theoretical result reported in the literature of κ of Ge obtained using MD simulations: ~ 90 W/mK [61].

Table 3.1.2: Experimental results of κ of c-Ge at 300K. (Natural Ge: $\bar{m}=72.61$, $^{74}\text{Ge}=35.94\%$, $^{72}\text{Ge}=27.66\%$, $^{70}\text{Ge}=21.23\%$, $^{73}\text{Ge}=7.73\%$, $^{76}\text{Ge}=7.44\%$)

Experimental method	κ (W/mK)	sample	Ref.
Absolute, steady-state, longitudinal heat flow	~ 50	natural	[59]
Variable state, thermal diffusivity	~ 50	natural	[60]
Absolute, steady-state, radial heat flow	~ 60	natural	[47]
Optical pump-and-probe technique	~ 78	^{70}Ge	[19]

3.1.3 Silicon dioxide

Silicon dioxide (SiO_2) is the most abundant mineral in the Earth's crust. Because of its special chemical, electronic and optical properties, it has been used in a number of different applications. SiO_2 layers and surfaces are considered to be essential elements in modern electronic devices. Therefore, understanding heat transport in silicon dioxide is of great interest for heat management in electronic devices and to effectively optimize the efficiency of these devices.

There is only a limited amount of data on the thermal conductivity of the many forms of crystalline silica due to their complex structures. Recently many experimental studies have only focused on the thermal conductivity of zeolites [62, 63, 64, 65]. To the best of our knowledge, there is no available experimental value of κ for crystalline α -cristobalite.

On the theoretical side, the NEMD approach has been widely used to compute the thermal conductivity of crystalline and amorphous silica [66, 67, 68, 69, 70]. McGaughey and Kaviany [71] found that it was very difficult to compute κ of crystalline silica by using EMD simulations, where κ is obtained by integrating the computed heat current autocorrelation functions $\langle J(t)J(0) \rangle = C J(T)$ (See Chapter 2). They observed large oscillations in $C J(t)$ of crystalline silica samples, and such oscillations

made it difficult to perform either a direct integration or an exponential fitting to obtain κ . The oscillations were attributed to the relative motion of bonded atoms with different masses [72].

In this dissertation, the κ of bulk crystalline α -cristobalite (α -SiO₂) was calculated by directly integrating $CJ(t)$ in EMD simulations. A simple strategy (see Chapter 3.4) was employed to effectively eliminate the large oscillations in the computed $CJ(t)$. Our goal in studying crystalline α -SiO₂ is to generate reference results with which to compare our simulations for amorphous silica, and interpret the effect of amorphous silica present on the surfaces of Si nanowires.

In order to interpret our MD simulations, we carried out lattice dynamics calculations for all three solids: c-Si, c-Ge and α -SiO₂. The calculated mean free paths and group velocities obtained by using the Boltzmann transport equation provided insight into understanding the fundamental physics of heat transport in these materials.

3.2 Thermal transport in bulk crystalline silicon

At room temperature and low pressure, silicon has a diamond structure, as shown in Fig. 3.2.1. In this study, the initial configurations of all bulk crystalline silicon (c-Si) samples are supercells obtained from the replicated diamond cubic unit cell with lattice constant $a=5.4 \text{ \AA}$ (experimental value). We carried out EMD simulations using the LAMMPS code and the Tersoff potential [33]. Periodic boundary conditions were applied to all three directions. The chosen time step is 0.5fs. Each sample has been first heated to 300K for 400ps by using NPT and NVT ensemble simulations, and then equilibrated at this temperature for 200ps within NVE (constant number of particles N, volume V and energy E). After equilibration, computation of the heat current was started and the heat current was obtained using Eq. 2.2.28. The thermal

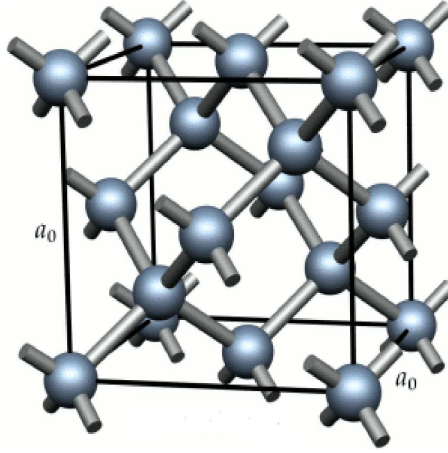


Figure 3.2.1: Schematic diagram of the diamond structure adopted by Si and Ge (Figure from <http://worldscheaper.com>).

conductivity was calculated using the Green-Kubo formula (see Eq. 2.2.22). The heat current autocorrelation function was evaluated with fast Fourier transforms [24]. The convergence of κ of c-Si as a function of simulation time was carefully tested. Our results show that 10 ns simulations are necessary to obtain converged value of κ . All MD runs for c-Si were carried out for 10ns (see Tab. 3.2.1).

The convergence of κ with respect to the truncation time used in the integration of the heat current autocorrelation function $\langle J(t)J(0) \rangle = CJ(t)$ in Eq. 2.2.22 was also tested. Fig. 3.2.2 shows the computed $CJ(t)$ and κ for a silicon sample with 4096 atoms. A truncation time of 200 ps yielded well converged values. In order to test size effects, we carried out simulations for various supercells containing 64(2x2x2), 216(3x3x3), 512 (4x4x4), 1000(5x5x5), 1728(6x6x6), 2744 (7x7x7), and 4096 (8x8x8), 27000(15x15x15), 64000(20x20x20), 216000 (30x30x30), 1000000(50x50x50) atoms (see Tab. 3.2.1). We find that to obtain a reliable value of κ of c-Si, one has to use cells with at least 27000 atoms. As shown in Fig. 3.2.3, the calculated values of κ using supercell with 64000, 216000 and 1000000 atoms are the same within error bars.

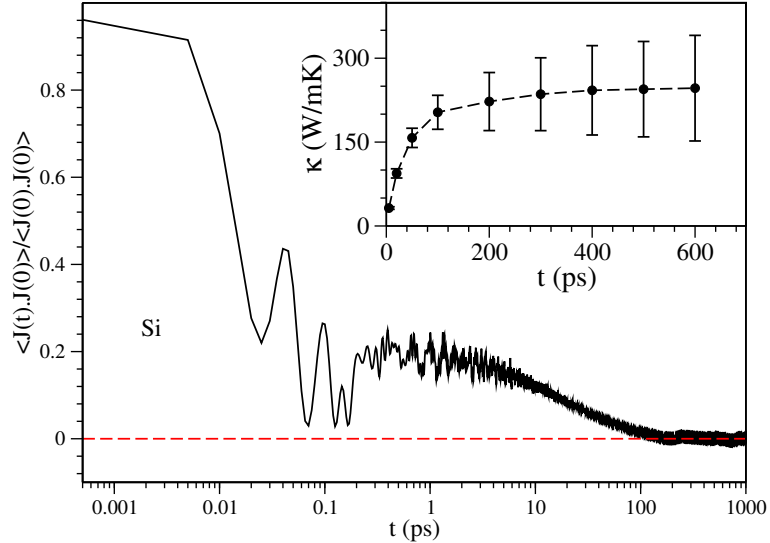


Figure 3.2.2: The normalized heat current autocorrelation function of a crystalline silicon sample with 4096 atoms at room temperature. The in-set shows the calculated thermal conductivity as a function of different truncation times.

Our results on size convergence may explain the conflicting results for κ reported in the literature [36, 56, 57]. Our converged value of κ of c-Si is about 200 W/mK. Given the complexity of real silicon materials (including defects, grain boundaries, and impurities), we consider the agreement with experiment as satisfactory.

We also computed κ of c-Si using NEMD simulations (see Chapter 2.2.2). This approach is analogous to experimental methods, where a temperature gradient is created within the material, and the thermal conductivity is obtained by the ratio between the measured heat flow and the temperature gradient. In order to use Fourier's law (Eq. 2.2.31) to calculate the thermal conductivity, one has to find the linear response regime in which the inverse of the thermal conductivity linearly depends on the inverse of the simulation sample length. Sellan et al. [55] pointed out that a linear extrapolation procedure is only accurate when the minimum size used in NEMD simulations is comparable to the largest mean-free-paths of the phonons that

Table 3.2.1: Computed thermal conductivity of bulk crystalline silicon from equilibrium molecular dynamics (MD) as a function of the number of atoms in the simulation supercells at room temperature. For each cell size we carried out five independent runs, each 10ns long. All values of the thermal conductivity are calculated by integrating the heat current autocorrelation function (Green-Kubo formula) with a 200 ps truncation time. The density of all samples is $\sim 2.31g/cm^3$. n_1 , n_2 and n_3 denote the number of times a unit cell is repeated along the x, y, z direction, respectively.

Number of atoms in MD cell	κ (W/mK)	$n_1 \times n_2 \times n_3$
64	94.18 \pm 3.75	2 \times 2 \times 2
216	214.44 \pm 21.65	3 \times 3 \times 3
512	253.31 \pm 14.22	4 \times 4 \times 4
1000	204.27 \pm 42.14	5 \times 5 \times 5
1728	210.29 \pm 30.65	6 \times 6 \times 6
2744	248.89 \pm 18.92	7 \times 7 \times 7
4096	220.72 \pm 20.02	8 \times 8 \times 8
27000	225.38 \pm 30.29	15 \times 15 \times 15
64000	198.39 \pm 20.86	20 \times 20 \times 20
216000	205.38 \pm 24.99	30 \times 30 \times 30
1000000	198.39 \pm 20.86	50 \times 50 \times 50

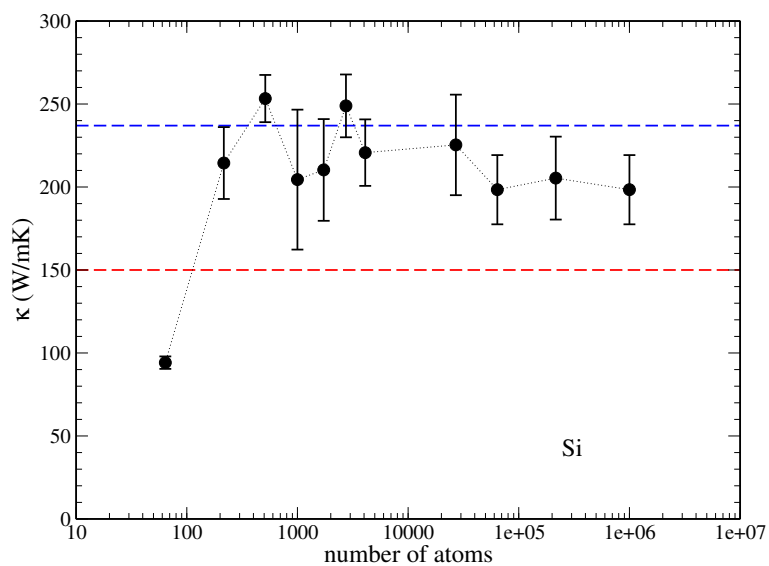


Figure 3.2.3: Thermal conductivity of crystalline silicon as a function of the number of atoms in the simulation supercell at 300 K, computed within equilibrium molecular dynamics, using the Green-Kubo formula (Eq. 2.2.22). The red dashed line is the experimental result for natural silicon [47]. The blue dashed line is the experimental result for enriched ^{28}Si [52].

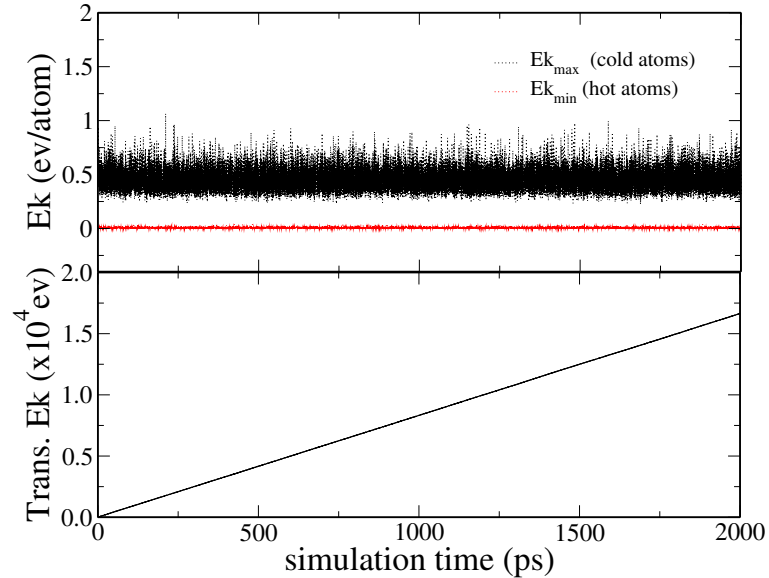


Figure 3.2.4: The exchange of kinetic energy between an atom in the cold slab and a atom in the hot slab in non-equilibrium molecular dynamics simulations of crystalline Si. A cell with 11520 atoms was used in this case. Top panel: The black curve shows the kinetic energy of atoms with the largest kinetic energy in the cold slab. The red curve shows the kinetic energy of atoms with the smallest kinetic energy in the hot slab. Bottom panel: accumulation of transferred kinetic energy between the two sets of atoms as a function of simulation time.

dominate the thermal transport. In general, this condition has not been satisfied in previous works [54, 73, 74, 75].

In this work, we chose samples with the cross section of $2.17\text{nm} \times 2.17\text{nm}$ for calculations of the thermal conductivity at both 300K and 1000 K. For the same cross section, the artificial heat current is inversely proportional to w , where w is the number of time steps by which the kinetic energy is exchanged (see Fig. 3.2.4). By computing κ with various values of w ($w=20, 40, 60, 80, 100, 140$ and 180) for a sample of dimensions $2.17 \times 2.17 \times 16.57\text{nm}$, we found that linear temperature profiles can be obtained by using $w=100$ steps i.e. 50fs.

In order to check whether a steady state was reached in our simulations, we

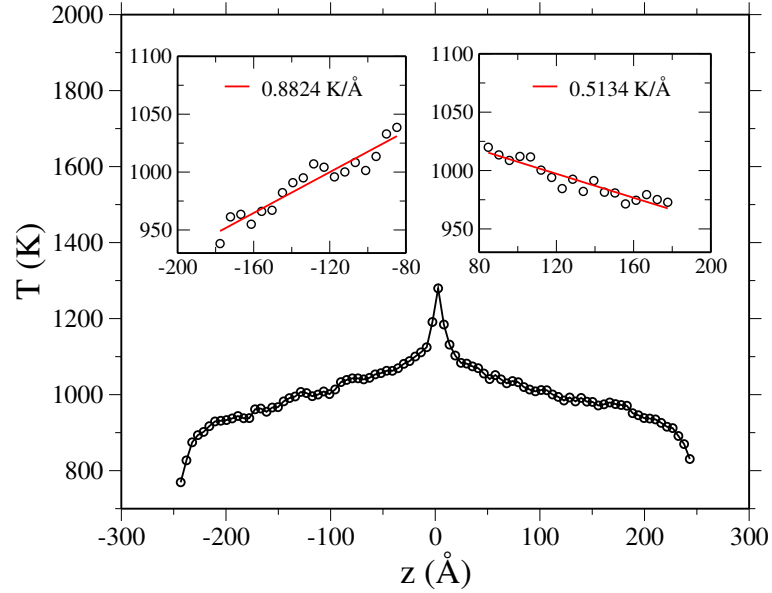


Figure 3.2.5: The temperature profile for a bulk silicon sample simulated using non-equilibrium molecular dynamics in a cell of dimensions $2.17 \times 2.17 \times 16.57 \text{ nm}$ at 1000 K. The simulation was run for 500ps. The heat source is located in the middle of the simulation box, and the heat sinks are placed at two ends of the simulation box. The insets show the linear fits of the temperature gradient on the left and right of the heat source, respectively.

computed the temperature profile of the systems for two different simulation time, as shown in Fig. 3.2.5. and Fig. 3.2.6. Before the system reaches a steady state, the temperature profile calculated from the instantaneous local kinetic temperature in each slab is changing abruptly as a function of the simulation time. After the steady state is reached, the temperature profile becomes smooth, and shows an equal value of the temperature gradient on both sides of the heat source.

Once the heat current is obtained from the transferred kinetic energy and the temperature gradient is obtained from the temperature profile, the thermal conductivity can be calculated based on Fourier's law: $\kappa = \lim_{\partial T / \partial z \rightarrow 0} \lim_{t \rightarrow \infty} -\frac{\langle J_z(t) \rangle}{\partial T / \partial z}$. Fig. 3.2.7 shows the calculated κ of c-Si for various lengths of the simulation cell

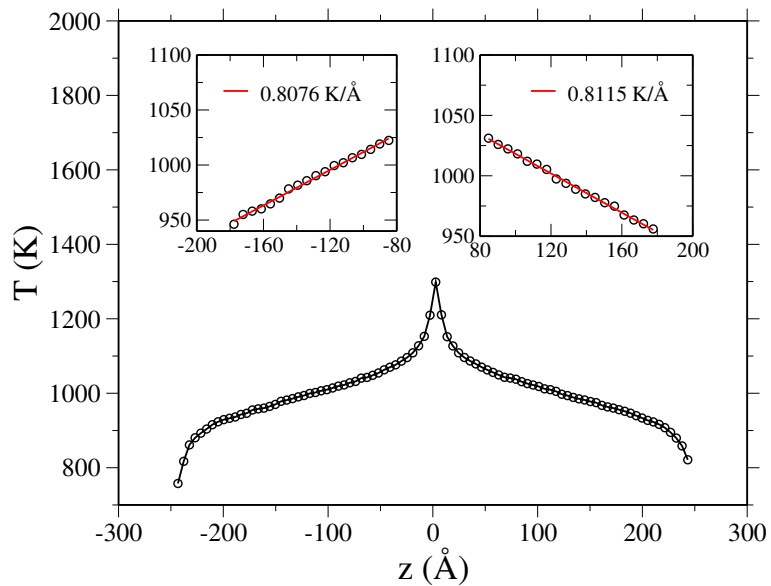


Figure 3.2.6: The temperature profile for a bulk silicon system simulated using non-equilibrium molecular dynamics in a cell of dimensions $2.17 \times 2.17 \times 16.57 \text{ nm}$ at 1000 K. The simulation was run for 2 ns. The heat source is located in the middle of simulation box, and the heat sinks are placed at two ends of the simulation box. The insets show the linear fits of temperature gradient on the left and right of the heat source, respectively.

at $T=300\text{K}$ ($L=48.88\text{nm}, 65.17\text{nm}, 86.90\text{nm}, 119.48\text{nm}, 195.52\text{nm}, 249.82\text{nm}$) and $T=1000\text{K}$ ($L=97.76\text{nm}, 152.07\text{nm}, 195.52\text{nm}$). The linear fit was done following Schelling's work [54]. At 300K , only the values obtained for the four largest cells were used in our fitting procedure. We can see that $1/\kappa$ is not linear as a function of $1/L$ when using small simulation cells. The extrapolated value of κ from the linear fits of Fig. 3.2.7 yields 58.45 ± 3.1 W/mK at 1000K , and 295.81 ± 20.06 W/mK at 300K . Both results are larger than those obtained from EMD calculations. For equilibrium MD calculations, the κ of silicon at 1000K is 48.85 ± 8.60 W/mK, and at 300K is 253.31 ± 14.22 W/mK when considering systems of size comparable to that used in our NEMD (with size $2.17 \times 2.17 \times 2.17\text{nm}$). We note that values of κ for silicon samples with same sizes in both equilibrium and non-equilibrium simulations are compared, to avoid possible domain size effects due to periodic boundary conditions. Sellan et al. [55] predicted that to obtain accurate κ of bulk silicon using NEMD, one need to simulate systems with length of $3.3\ \mu\text{m}$ at 500K , and $1.5\ \mu\text{m}$ at 1000K . Therefore, the lengths of our simulation cells may not be large enough to give consistent results with equilibrium MD calculations. We find that κ is overestimated with respect to equilibrium MD calculations, while Sellan et al. [55] found that κ was underestimated with small samples. In addition, the rate of change of $1/\kappa$ with $1/L_z$ is not temperature-dependent, which is different from the finding of Schelling et al. [54] using a Stillinger-Weber potential.

In order to understand the microscopic properties of heat carriers in bulk crystalline silicon, lattice dynamics calculations (see Chapter 2.3.1) were carried out using cells ($2.17 \times 2.17 \times 2.17\text{nm}$) with $N = 512$ atoms. We used the Γ point only. Although this system is small and results will not be fully converged as a function of size, these calculations can provide us a qualitative picture of lattice vibrations. The dynamical

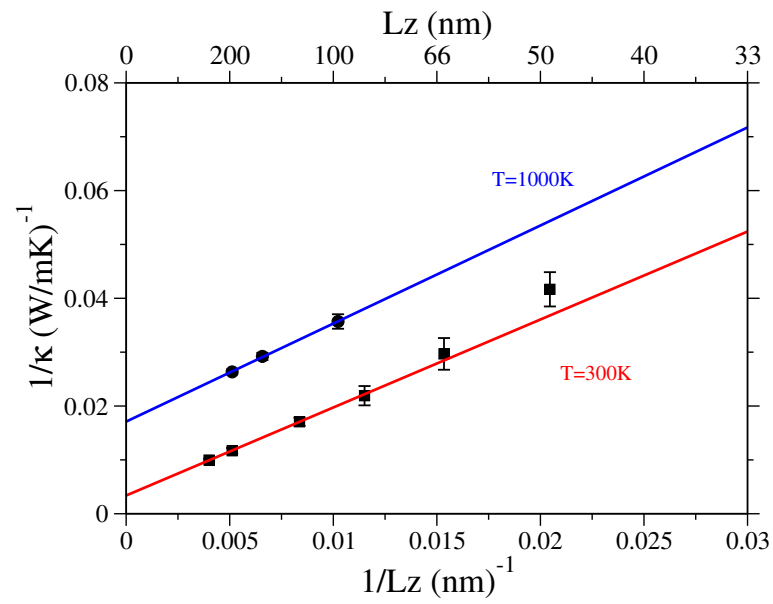


Figure 3.2.7: Calculated inverse of the thermal conductivity (κ) in bulk silicon as a function of the inverse of the size of simulation cell (L_z) along the heat flow direction. Black circles correspond to 1000K simulations and black squares to 300K. Blue and red lines are linear fits to the 1000K and 300K results, respectively.

matrix Ω was obtained by computing derivatives of forces acting on atoms as finite differences. Ω was then diagonalized to obtain $3N$ eigenvectors (\mathbf{e}) and $3N$ eigenvalues (ω) for the Γ point ($\mathbf{q}=0$) and a number of small wave vectors \mathbf{q} close to the Γ point, in the supercell Brillouin zone. The group velocities were computed by a linear fit around Γ with five \mathbf{q} points, according to the definition $\mathbf{v}_{\mathbf{q}=0} = \frac{\Delta\omega}{\Delta\mathbf{q}}$. The lifetime of mode i was calculated from the normalized autocorrelation function of the eigenmode energy ($E_i(\mathbf{q}, t)$)(see Chapter 2) [42].

Fig. 3.2.8 and 3.2.9 show the calculated group velocities (v_g) and lifetimes (τ) of vibrational modes in bulk crystalline silicon, respectively. The estimated speed of sound from longitudinal and transverse group velocities is 6347 m/s by the formula $v = \frac{v_L+2v_T}{3}$ which is larger than the experimental value (5639 m/s). The advantage of calculating lifetimes from eigenmodes' energies in molecular dynamics is that it includes the full description of anharmonic effects without any approximations. As shown in Fig. 3.2.9, the calculated lifetime in bulk silicon scale as $\nu^{-1.6}$ over a broad spectrum range, while at low frequencies, it approaches the Klemen's prediction of $\tau \propto \nu^{-2}$ [76].

The mean free paths were computed from group velocities and lifetimes: $\lambda = v_g \cdot \tau$. We find that the mean free paths in silicon are strongly dependent on frequencies (see Fig. 3.2.10). At low frequencies, they are of the order of a micrometer, and gradually decrease to nanometer at very high frequencies. The micron long mean free paths observed here confirm that the sizes of simulation cells used in our non-equilibrium molecular dynamics simulations are too small to fully account for the thermal conductivity of c-Si by a linear fitting procedure.

Using lattice dynamics calculations, we computed the thermal conductivity of bulk silicon using the Boltzmann transport equation (BTE) under the single mode

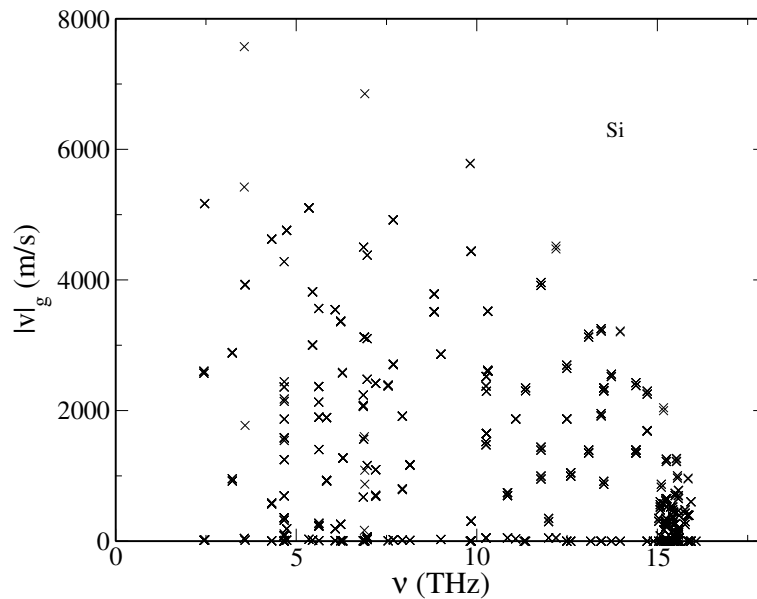


Figure 3.2.8: The magnitude of group velocities of vibrational modes as a function of frequency for a crystalline silicon sample with 512 atoms, as obtained by anharmonic lattice dynamics calculations.

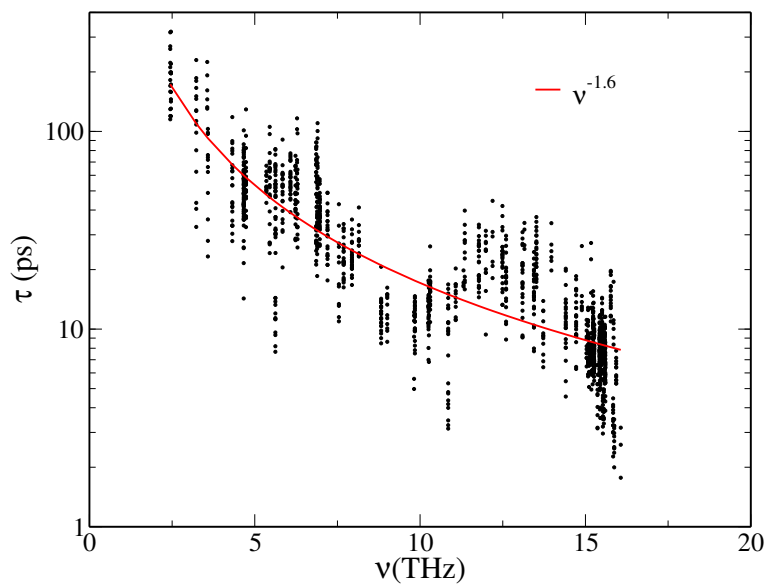


Figure 3.2.9: Lifetime of vibrational modes as a function of frequency for a crystalline silicon sample with 512 atoms, as obtained by anharmonic lattice dynamics calculations.

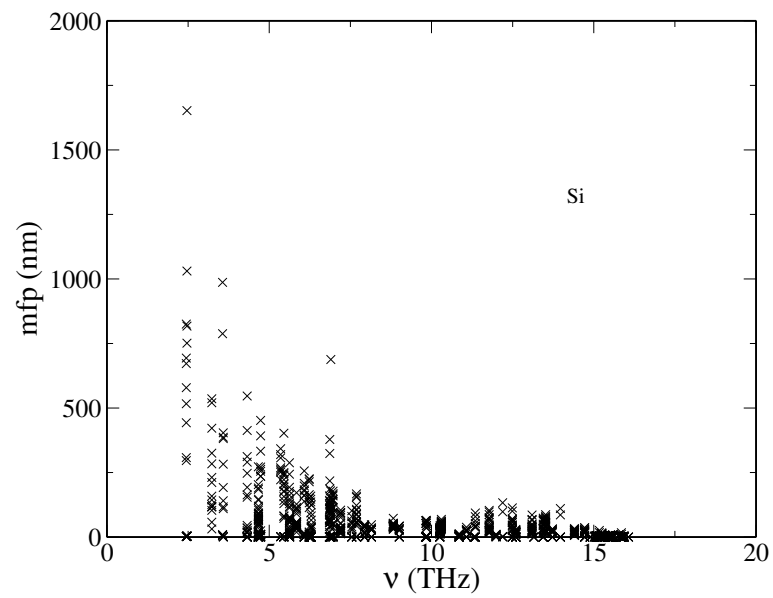


Figure 3.2.10: Mean free paths of vibrational modes as a function of frequency for a crystalline silicon sample with 512 atoms, as obtained by anharmonic lattice dynamics calculations.

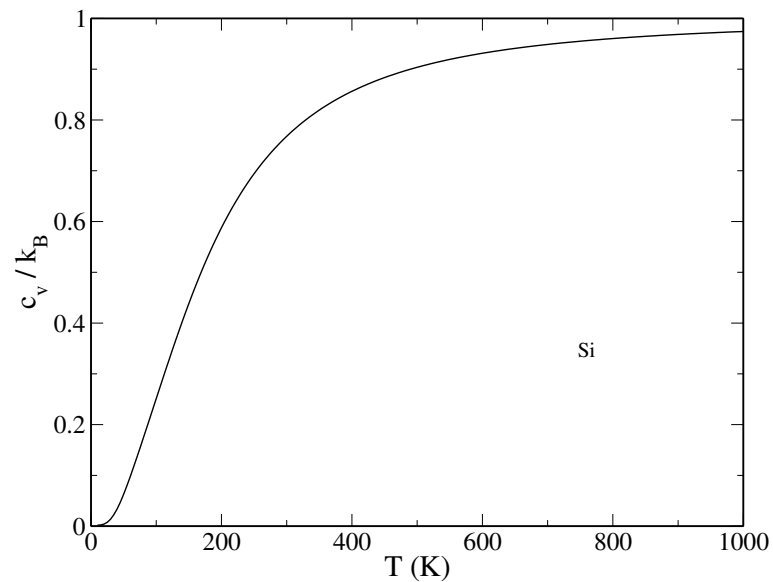


Figure 3.2.11: The ratio between quantum and classical values of the heat capacity of bulk crystalline silicon as a function of temperature.

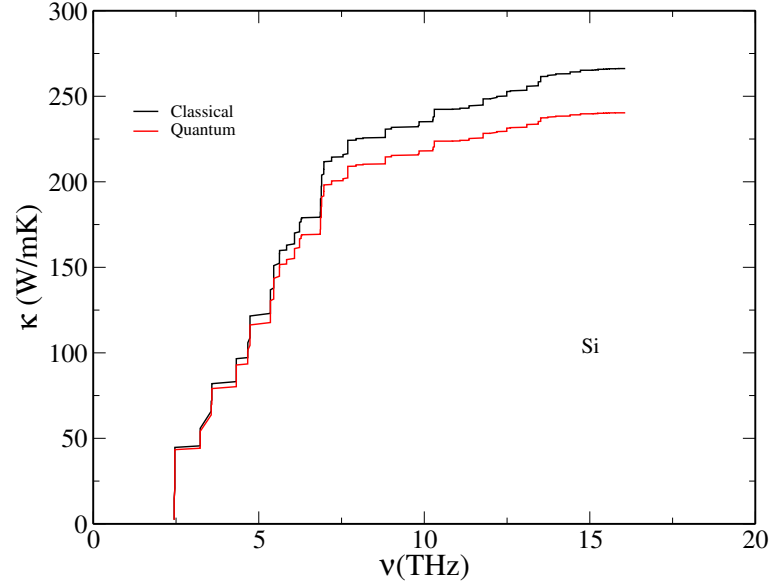


Figure 3.2.12: Contribution to the thermal conductivity of bulk crystalline silicon from vibrational modes as a function of their frequency, computed using cells with 512 atoms. The black (red) curve denotes results obtained using the classical (quantum) distribution for the specific heat.

relaxation time approximation [42] from the formula:

$$\kappa = \frac{1}{3} \sum_i \tau_i v_i^2 c_{i,V} \quad (3.2.1)$$

where, τ_i is the lifetime, v_i is the group velocity and $c_{i,V}$ is the specific heat per volume of mode i .

Fig. 3.2.11 shows the calculated ratio between quantum and classical values ($C = k_B$) of the heat capacity at constant volume. The quantum value is computed by using the Bose-Einstein distribution:

$$C = \sum_i c_V(i) = \sum_i k_B x^2 \frac{e^x}{(e^x - 1)^2} \quad (3.2.2)$$

with $x = \frac{\hbar\omega(i)}{k_B T}$; k_B is Boltzmann constant, and T is temperature.

As shown in Fig. 3.2.12, the calculated classical value is 20% higher than the quantum one. We note that here we only considered the quantum effects arising from the specific heat. If quantum effects on lifetimes are also taken into account, then the difference between classical and quantum values of κ should be smaller than 20%. Finally the classical value obtained by the BTE is compared with the results calculated by equilibrium MD. The BTE value is only compared to that of κ obtained with a cell of size $2.17 \times 2.17 \times 2.17$ nm to avoid discrepancies due to size effects. The classical value of κ computed from BTE is 266 W/mK, and it is in good agreement with the results of equilibrium MD (253.31 ± 14.22 W/mK for a cell of $2.17 \times 2.17 \times 2.17$ nm).

3.3 Thermal transport in bulk crystalline germanium

Germanium (Ge) crystallizes in the diamond structure, as Si. In this work, the initial configurations of all bulk crystalline germanium (c-Ge) samples are obtained from replicas of the diamond cubic unit cell with lattice constant $a=5.66$ Å (experimental value). The EMD simulations were carried out using LAMMPS code and the Tersoff potential [33] with periodic boundary conditions in all three directions. The chosen time step is 0.5fs. Each sample has been first heated up to 300K for 400ps in NPT and NVT ensemble simulations, and then equilibrated at this temperature for 200ps within the NVE ensemble. After equilibration, the calculations of the heat current was started and the heat current was obtained through Eq. 2.2.28. The thermal conductivity was calculated using the Green-Kubo formula (see Eq. 2.2.22) and fast Fourier transforms [24]. All MD simulations for c-Ge were run for 10ns (see

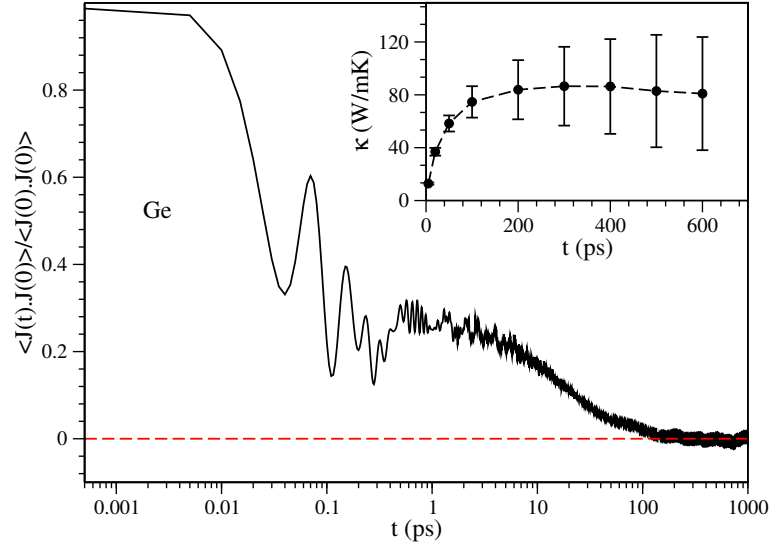


Figure 3.3.1: The normalized heat current autocorrelation function of a crystalline germanium sample with 4096 atoms at room temperature. The in-set shows the calculated thermal conductivity as a function of different truncation times.

Tab. 3.3.1).

The truncation time was chosen as 200ps according to the tests shown in Fig. 3.3.1. Size effects were also carefully tested. In order to do so, we carried out simulations for various supercells containing 64 (2x2x2), 216 (3x3x3), 512 (4x4x4), 1000 (5x5x5), 1728 (6x6x6), 2744 (7x7x7), and 4096 (8x8x8), 27000 (15x15x15), 64000 (20x20x20) and 216000 (30x30x30) atoms (see Tab. 3.3.1). We find that to obtain a converged value of κ of c-Ge, one has to consider cells with at least 27000 atoms. The value of κ averaged over the three largest sizes is 69.73 ± 12.45 W/mK. Compared with c-Si, the calculated κ of c-Ge is in better agreement with the experimental results. This is understandable given the Debye temperature of the two systems. The Debye temperature of silicon is 645 K, and that of germanium is 360 K. Therefore, we believe that EMD simulations for c-Ge at 300 K are more accurate than those for c-Si.

Similar to our study of Si, to understand the microscopic properties of heat carriers

Table 3.3.1: Computed thermal conductivity of bulk crystalline germanium from equilibrium molecular dynamics (MD) as a function of the number of atoms in the simulation supercells at room temperature. For each cell size we carried out five independent runs, each 10ns long. All values of the thermal conductivity are calculated using integration of the heat current autocorrelation function (Green-Kubo formula) with 200 ps truncation time. The density of all samples is 5.3 g/cm^3 . n_1 , n_2 and n_3 denote the number of times a unit cell is repeated along the x, y, z direction, respectively.

Number of atoms in MD cell	κ (W/mK)	$n_1 \times n_2 \times n_3$
64	50.64 ± 5.30	$2 \times 2 \times 2$
216	111.14 ± 15.91	$3 \times 3 \times 3$
512	87.30 ± 9.77	$4 \times 4 \times 4$
1000	89.78 ± 7.10	$5 \times 5 \times 5$
1728	74.67 ± 10.94	$6 \times 6 \times 6$
2744	81.25 ± 15.27	$7 \times 7 \times 7$
4096	83.86 ± 3.39	$8 \times 8 \times 8$
27000	70.27 ± 6.01	$15 \times 15 \times 15$
64000	73.42 ± 11.12	$20 \times 20 \times 20$
216000	65.50 ± 12.26	$30 \times 30 \times 30$

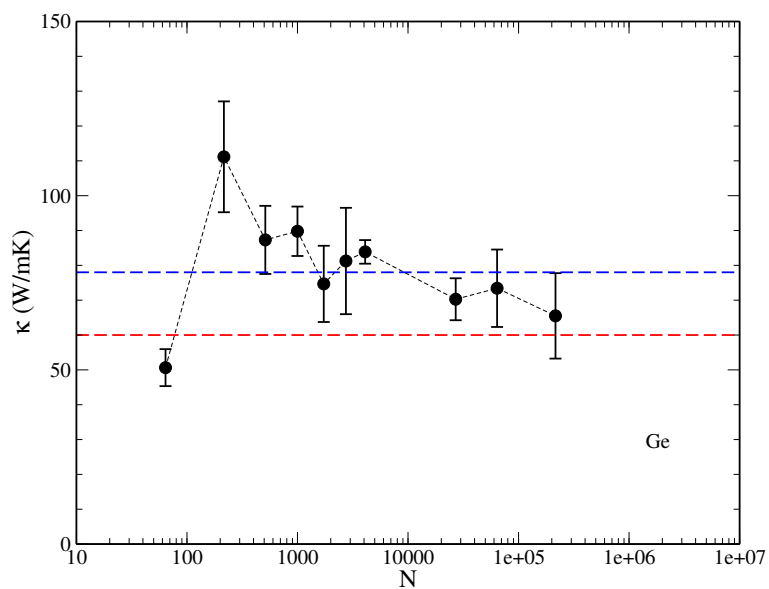


Figure 3.3.2: Thermal conductivity of crystalline germanium as a function of the number of atoms in the simulation supercell at 300 K, computed with equilibrium molecular dynamics, using the Green-Kubo formula (Eq. 2.2.22). The red dashed line is the experimental result for natural germanium [47]. The blue dashed line is the experimental result for ^{70}Ge [19].

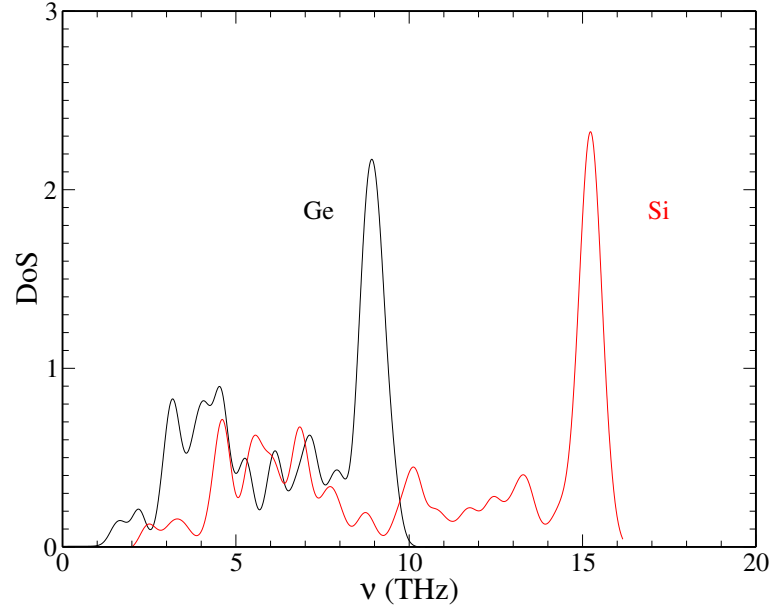


Figure 3.3.3: Density of states for bulk crystalline germanium (black) and bulk crystalline silicon (red), computed from Fourier transforms of the velocity-velocity auto-correlation function in MD simulation at 300K. Cells with 512 atoms were used for both Si and Ge.

in c-Ge, lattice dynamics calculations were carried out using germanium supercells of size $(2.26 \times 2.26 \times 2.26\text{nm})$ with $N = 512$ atoms. Velocities and lifetimes were computed following the same procedure as the one described in the case of crystalline Si.

The computed phonon spectrum of c-Ge (see Fig. 3.3.3) in MD simulations at 300K is similar to that independently calculated by lattice dynamics. There is no strong dependence of the phonon spectrum on temperature observed in this work, especially at low frequency.

Fig. 3.3.4 shows the calculated group velocities (v_g) of the vibrational modes of c-Ge. Compared to c-Si, all values of v_g are reduced. The estimated speed of sound obtained from longitudinal and transverse modes is 4056 m/s, in good accord with the experimental value of 4003 m/s. Unlike c-Si, the computed lifetimes (τ) (see Fig.

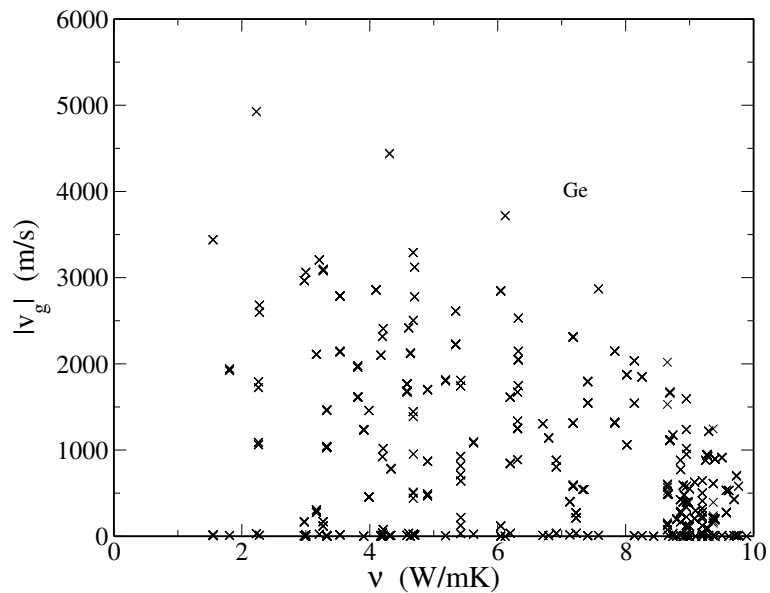


Figure 3.3.4: The magnitude of group velocities of vibrational modes as a function of frequency for a crystalline germanium sample with 512 atoms, as obtained by anharmonic lattice dynamics calculations.

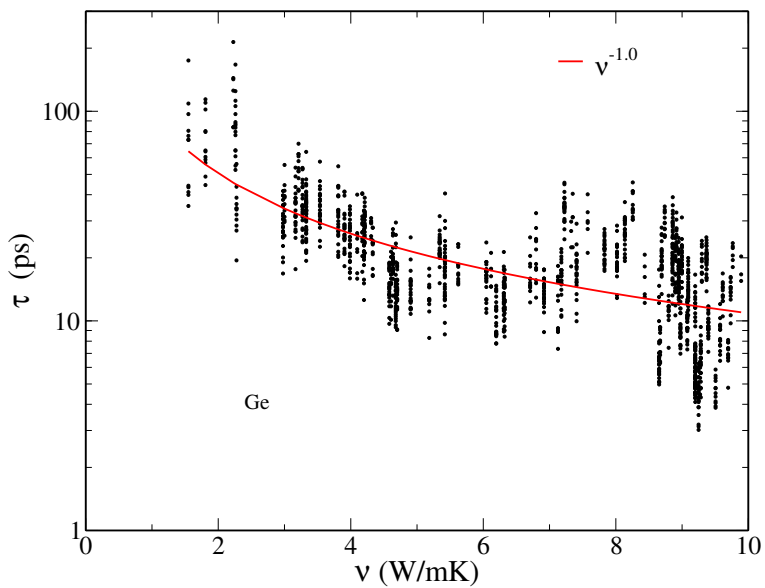


Figure 3.3.5: Lifetime of vibrational modes as a function of frequency for a crystalline germanium sample with 512 atoms, as obtained by anharmonic lattice dynamics calculations.

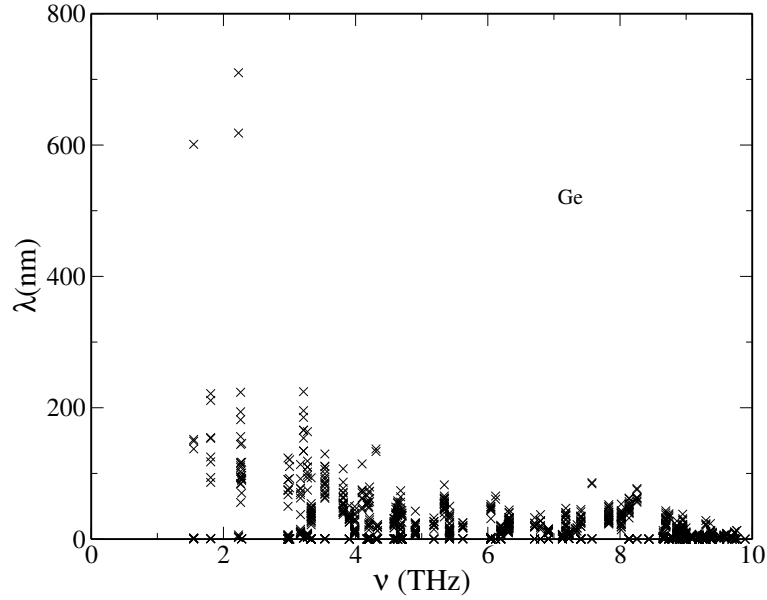


Figure 3.3.6: Mean free paths of vibrational modes as a function of frequency for a crystalline germanium sample with 512 atoms, as obtained by anharmonic lattice dynamics calculations.

3.3.5) in Ge behave as $\nu^{-1.0}$, and at low frequency, they do not exhibit like $\tau \propto \nu^{-2}$ predicted by Klemen [76].

The mean free paths in c-Ge were calculated as $\lambda = v_g \tau$, and they are shown in Fig. 3.3.6. Most modes have values of $\lambda < 200$ nm, except for some low frequency modes, which have λ of about 700 nm.

We then computed the κ of c-Ge at 300K using the BTE under the single mode relaxation time approximation. The specific heat of vibrational modes was computed using both the classical and quantum distributions (see Fig. 3.3.7). We find that the classical value of κ is 10% larger than the quantum one as shown in Fig. 3.3.8. Again, here we only considered the quantum effects arising from the specific heat. If the quantum effects on lifetimes are taken into account, the quantum value of κ for c-Ge is expected to be closer to that obtained with EMD. The classical value of κ from

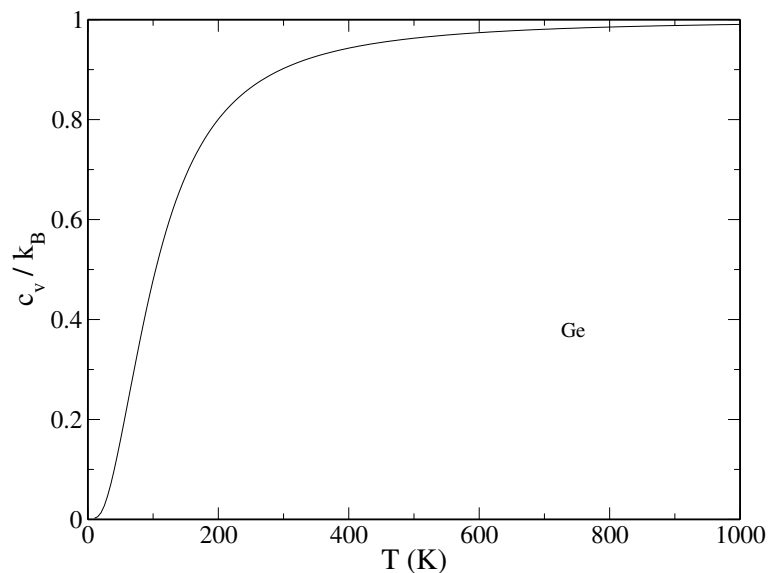


Figure 3.3.7: The ratio between quantum and classical values of the heat capacity of bulk crystalline germanium as a function of temperature.

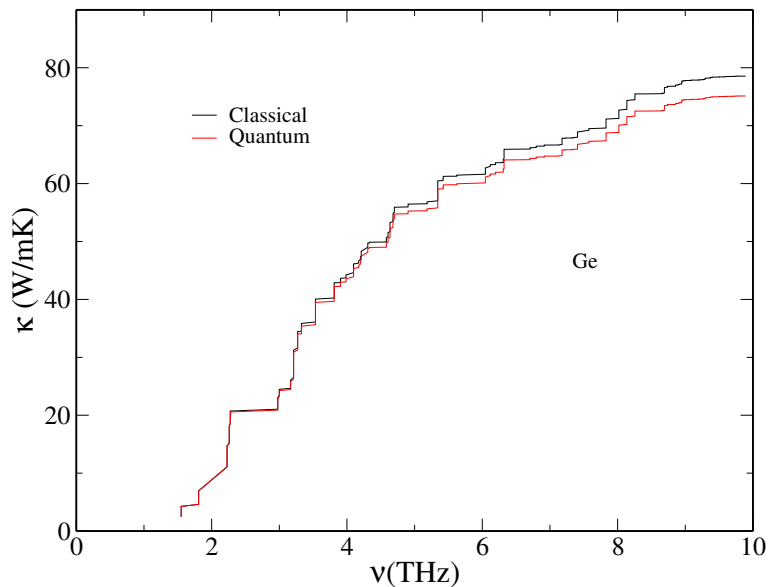


Figure 3.3.8: Contribution to the thermal conductivity of bulk crystalline germanium from vibrational modes as a function of their frequency, computed using cells with 512 atoms. The black (red) curve denotes results obtained using the classical (quantum) distribution for the specific heat.

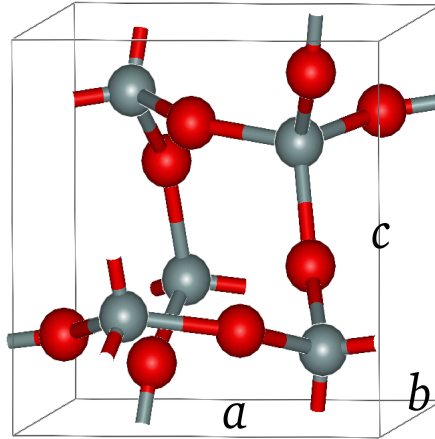


Figure 3.4.1: Tetragonal unit cell of crystalline α -cristobalite. Red spheres represent oxygen atoms and gray spheres are silicon atoms (Figure from <http://en.wikipedia.org>).

BTE is 78.56 W/mK, and it is consistent with the EMD result (87.30 ± 9.77 W/mK) within error bars. This EMD result was computed with a cell of $2.26 \times 2.26 \times 2.26$ so as to carry out a consistent comparison.

3.4 Thermal transport in bulk crystalline silicon dioxide

Silica has a number of distinct crystalline forms, which are all built from SiO_4 tetrahedra. In this work, the bulk crystalline α -cristobalite ($\alpha\text{-SiO}_2$) structure is studied, which has a tetragonal crystal structure with lattice constants $a=b=4.9717$ Å and $c=6.9223$ Å (experimental values), as shown in Figure 3.4.1. The initial configurations of all $\alpha\text{-SiO}_2$ supercells were obtained from replicas of the tetragonal unit cell. The EMD simulations were carried with the LAMMPS code and a parameterized Tersoff potential [77]. Periodic boundary conditions were applied to X, Y and

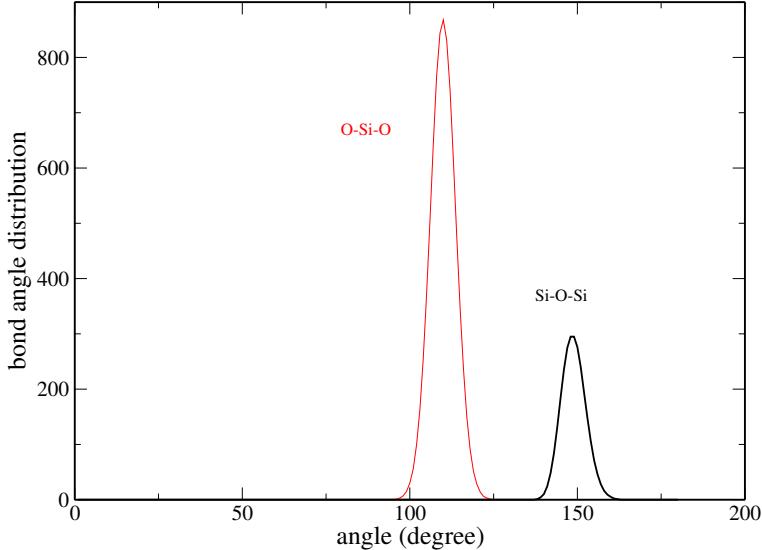


Figure 3.4.2: Computed bond angle distribution of Si-O-Si (black) and O-Si-O (red) in a sample of crystalline α -cristobalite with 4116 atoms, generated by EMD simulations.

Z directions. The chosen time step is 0.2fs. Each sample has been first heated up to room temperature for 500ps in NPT and NVT ensemble simulations, and then equilibrated at 300K for 200ps within NVE. To investigate our simulation samples, we calculated several structural properties. Fig. 3.4.2 shows that the average bond angles of Si-O-Si and O-Si-O are 148° and 109° , respectively. The average bond of Si-O is 1.62 \AA (see Fig. 3.4.3). These calculated structural properties are in fairly good agreement with the experimental measurements [78, 79]. In addition, the computed coordination number in Fig. 3.4.4 shows that in our α -cristobalite samples, the oxygen bridges between the two silicon atoms and the silicon is perfectly coordinated by four oxygen neighbors. The estimated average density of the equilibrated samples is 2.1 g/cm^3 to be compared with the experimental value of 2.3 g/cm^3 [78].

As described in Chapter 2.2.1, in EMD simulations, κ is computed using the

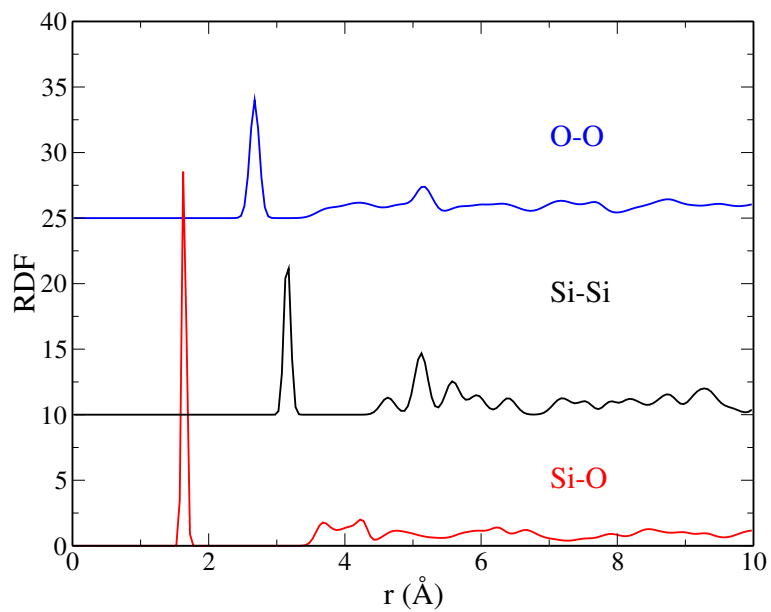


Figure 3.4.3: Partial radial distribution functions for a crystalline α -cristobalite sample with 4116 atoms, generated by EMD simulations.

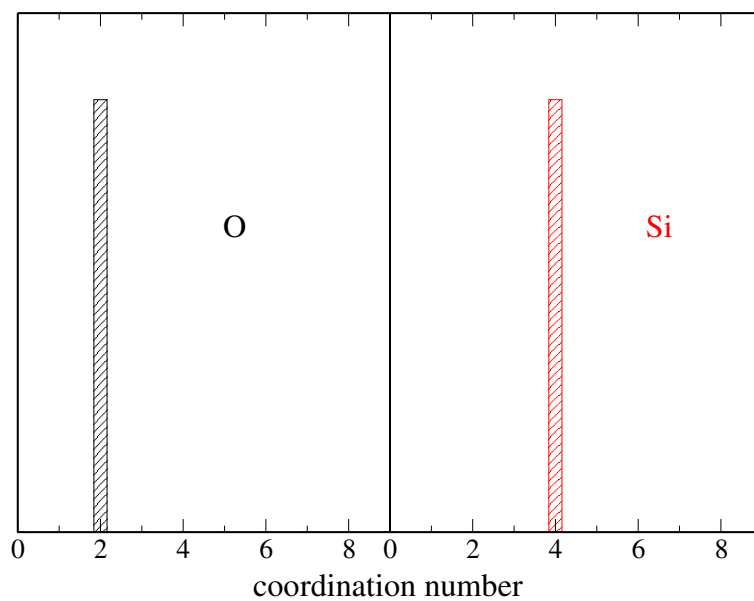


Figure 3.4.4: Computed coordination numbers of oxygen atoms (left) and silicon atoms (right) in a crystalline α -cristobalite sample with 4116 atoms, generated by EMD simulations.

Green-Kubo formula:

$$\kappa_\alpha = \frac{V}{k_B T^2} \int_0^\infty \langle J_\alpha(t) J_\alpha(0) \rangle dt, \quad (3.4.1)$$

In general, the heat current vector is computed by the following expression:

$$\mathbf{J} = \frac{1}{V} \left[\sum_i^N \epsilon_i \mathbf{v}_i - \sum_i^N \mathbf{S}_i \cdot \mathbf{v}_i \right] \quad (3.4.2)$$

here \mathbf{v} is the velocity vector. ϵ_i is the total energy (potential and kinetic) of atom i . \mathbf{S}_i is the 3×3 stress tensor of atom i . The first term of Eq. 3.4.2 represents the convective heat current, and the second term is the conductive heat current. Convective heat transfer occurs if matter is displaced within the sample; for example in a liquid matter may be displaced due to density fluctuations. In a solid, conduction is the most significant means of heat transfer by the lattice vibrations. To understand the contributions of these two mechanisms to the κ of α -SiO₂, we computed the κ of a sample with 768 atoms by evaluating the convective (J_v) and conductive (J_c) heat flux separately:

$$\mathbf{J}_v = \frac{1}{V} \left(\sum_i^N \epsilon_i \mathbf{v}_i \right) \quad (3.4.3)$$

and

$$\mathbf{J}_c = \frac{1}{V} \left(\sum_i^N \mathbf{S}_i \cdot \mathbf{v}_i \right) \quad (3.4.4)$$

Five simulations with five statistically independent configurations were carried out. The samples were first equilibrated at room temperature, and then the calculation of the heat current was started using Eq. 3.4.3 and 3.4.4. All five MD

Table 3.4.1: Thermal conductivity of bulk crystalline α -cristobalite as a function of the number of atoms in the simulation supercell at room temperature, in the xy-plane (κ_{xy}) and in the z direction (κ_z), respectively. Each value of the conductivity is obtained from averages over the results of 5 runs, each 5ns long. All values are calculated using integration of heat current autocorrelation function according to the Green-Kubo formula, with a 20 ps truncation time. The density of all α -SiO₂ samples is 2.1 g/cm³. n_1 , n_2 and n_3 denote the number of times a unit cell is repeated along the x, y, z direction, respectively.

Number of atoms in the MD cell	κ_{xy} (W/mK)	κ_z (W/mK)	$n_1 \times n_2 \times n_3$
768	3.00±0.43	3.39±0.39	4 × 4 × 4
4116	4.51±0.30	4.83±0.38	7 × 7 × 7
8748	4.24±0.22	4.74±0.20	9 × 9 × 9
20736	4.53±0.12	4.88±0.45	12 × 12 × 12
49152	4.71±0.32	4.50±0.26	16 × 16 × 16
96000	4.50±0.23	4.75±0.47	20 × 20 × 20

simulations were run for 5ns which is a time long enough to obtain a converged value of κ according to our tests.

We found that the large oscillations in $CJ(t)$ are caused by the convection term (see Fig. 3.4.5). The contribution of the convective term to κ is extremely small ($\sim 10^{-3}$), and can be neglected (see Fig. 3.4.6). Our results show that the conductive term is sufficient to predict the κ in the solid. After removing the convective heat flux component, we find that the computed κ has no oscillations as shown in Fig. 3.4.6. Therefore, in this study all calculations of κ of α -cristobalite samples were carried out using only the conductive heat flux term (Eq. 3.4.4) according to the Green-Kubo formula (Eq. 2.2.22). The values of κ in both the xy-plane and the z direction were calculated (see Tab. 3.4.1).

To check size effects, we carried out simulations for various supercells contain-

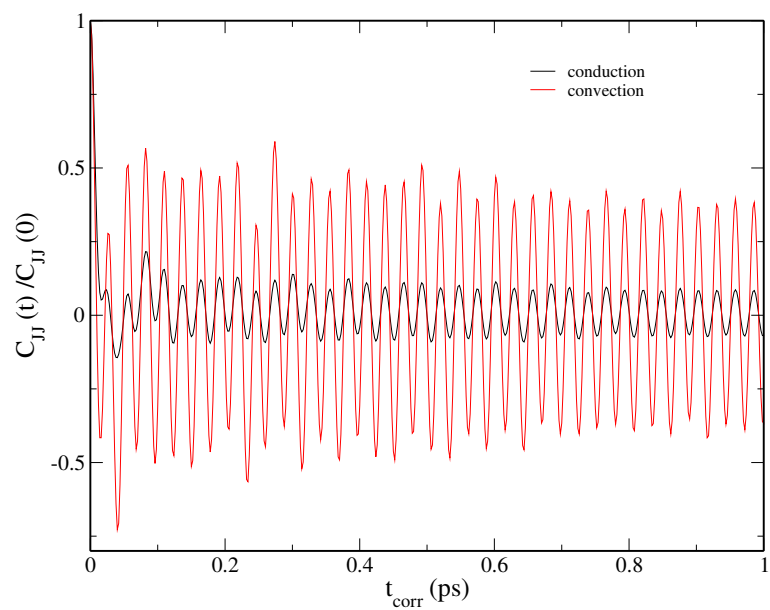


Figure 3.4.5: The normalized heat current autocorrelation functions of crystalline α -cristobalite simulated with 768 atoms on the xy-plane; contributions from convective (red) and conductive (black) terms are shown. Calculations were carried out at room temperature.

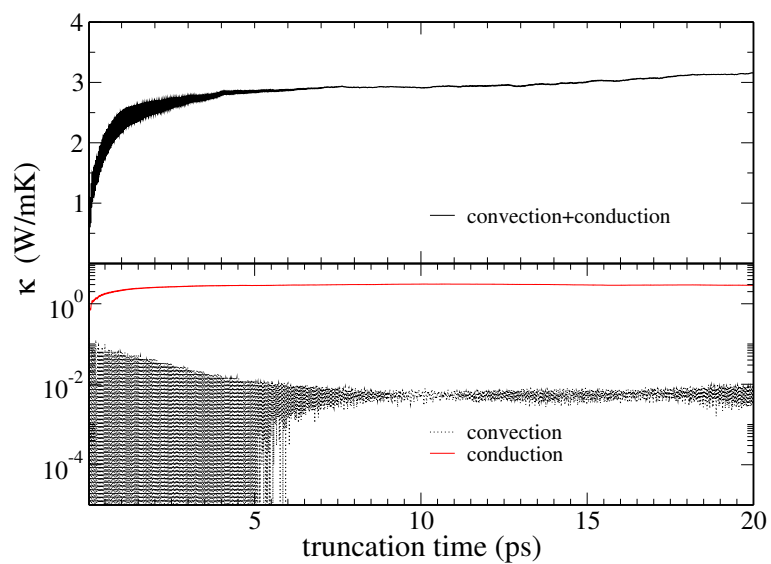


Figure 3.4.6: Thermal conductivity of crystalline α - cristobalite with 768 atoms along the xy-plane as a function of truncation time used in MD simulations. Top panel: Contributions from both convective and conductive terms. Bottom panel: The black curve shows the contribution from the convective term; the red curve shows the contribution from the conductive term.

ing 768(4x4x4), 4116(7x7x7), 8748 (9x9x9), 20736(12x12x12), 49152(16x16x16), 96000 (20x20x20)(see Tab. 3.4.1). Unlike c-Si and c-Ge whose computed κ strongly depends on the size of the simulated system, Fig. 3.4.7 shows that the κ of α -cristobalite becomes size-independent for box sizes larger than 4116 atoms, both in the xy-plane and in the z directions. The average values of κ over the five largest systems (N=4116, 8748, 20736, 49152, 96000) is 4.50 ± 0.27 W/mK in the xy-plane and 4.74 ± 0.41 W/mK in the z direction. To the best of our knowledge, there is no theoretical value of α -cristobalite reported in the literature. Domingues et al. [80] computed κ of β -cristobalite at 1800 K using EMD by fitting the heat current autocorrelation function. They obtained a value of $\kappa=5.5$ W/mK. Later, by using NEMD simulations, Huang et al. [69] studied the κ of β -cristobalite films, and found that κ appears to be thickness-independent and temperature-independent for thicknesses > 5.5 nm. They found that κ of a 7.2nm thick film is about 4.2 W/mK at 300K. These calculated values of κ in β -cristobalite are consistent with that of α -cristobalite computed here, since these two materials have similar crystal structures.

To understand the microscopic properties of heat carriers in α -cristobalite, lattice dynamics calculations were carried out using a cristobalite supercell of dimension $3.48 \times 3.48 \times 4.84$ nm with $N = 4116$ atoms. The dynamical matrix, frequencies, velocities and lifetimes were obtained using the same approach as discussed in the case of Si. We also computed the vibrational density of states (DoS) using the velocity-velocity autocorrelation functions obtained in MD simulations (see Fig. 3.4.8). The frequency spectra independently predicted by MD and by lattice dynamics are consistent with each other. We find that the computed DoS of α -cristobalite is analogous to that of α quartz [80, 81] obtained at room temperature using the Beest-Kramer-Santen (BKS) potential [82]. This is consistent with the experimental finding of

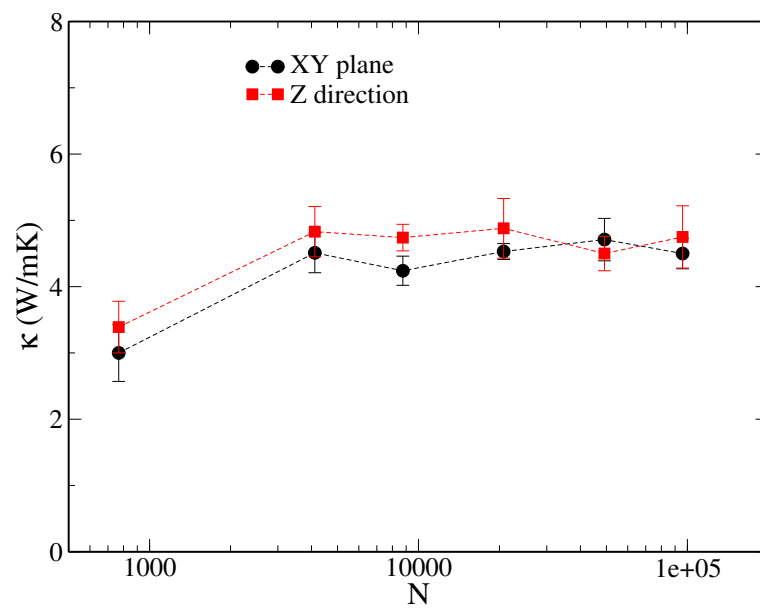


Figure 3.4.7: Thermal conductivity of crystalline α -cristobalite as a function of the number of atoms (N) in the MD cell ($N = 768, 4116, 8748, 20736, 49152, 96000$) at 300 K. Red squares and black dots denote the conductivity in the z direction and the xy -plane, respectively.

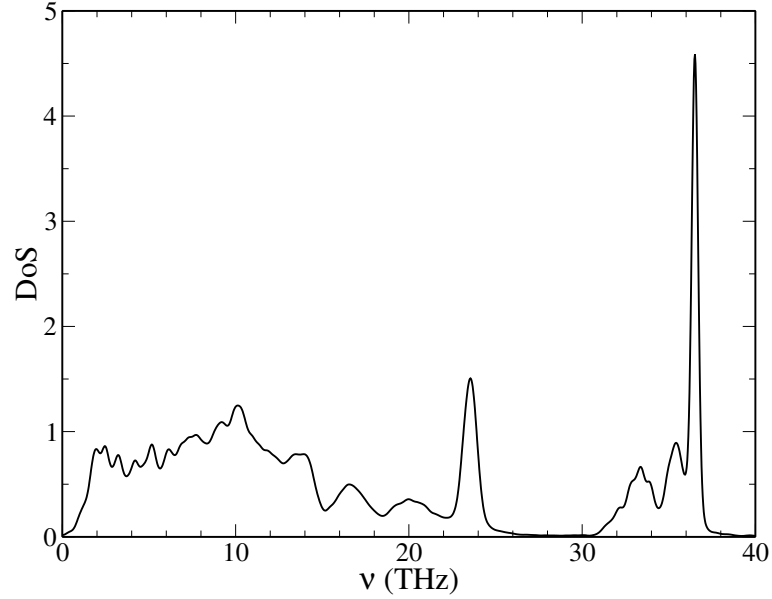


Figure 3.4.8: Vibrational density of states (DoS) of a crystalline α -cristobalite sample computed from the velocity-velocity autocorrelation function obtained in molecular dynamics simulation with a cell of 4116 atoms.

similar force constants for the two SiO_2 polymorphs. [83]. Fig. 3.4.9 shows that in cristobalite, most of the vibrational modes have large group velocities compared to those of c-Si and c-Ge. However, the computed lifetimes τ are much smaller than those in Si and Ge (see Fig. 3.4.10). The calculated mean free paths ($\lambda = v_g \tau$) turn out to be quite small (about few nanometer) except for several low frequency modes whose λ are few hundred nanometers (see Fig. 3.4.11). The presence of mostly small mean free paths may be related to the crystal structure of cristobalite. In α -cristobalite, the arrangement of SiO_4 tetrahedra around Si sites is locally disordered. The local disorder has a minor effect on the group velocities, but a major effect on lifetimes.

Fig. 3.4.12 shows the κ contributions as a function of their mean free paths computed using the BTE. We find that there are 4% of propagating modes which

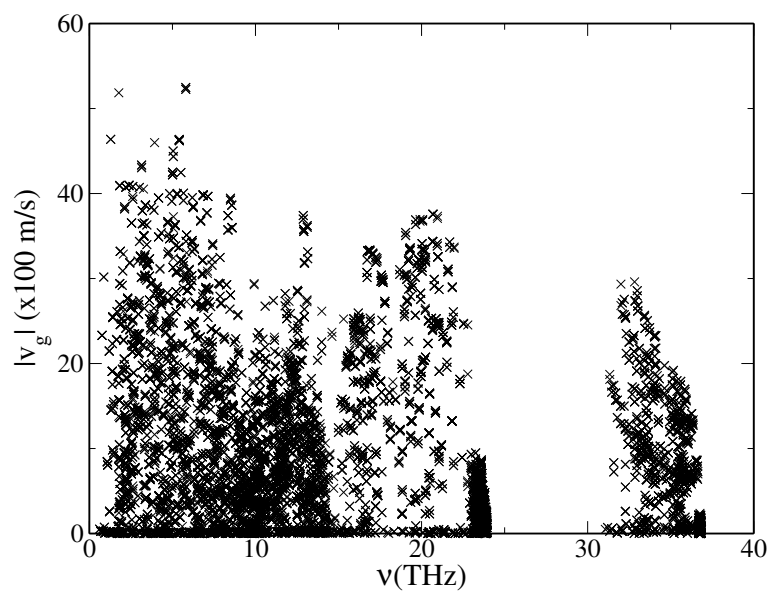


Figure 3.4.9: Calculated magnitude of the group velocities of vibrational modes as a function of frequency for a crystalline α -cristobalite sample, computed with cells of 4116 atoms.

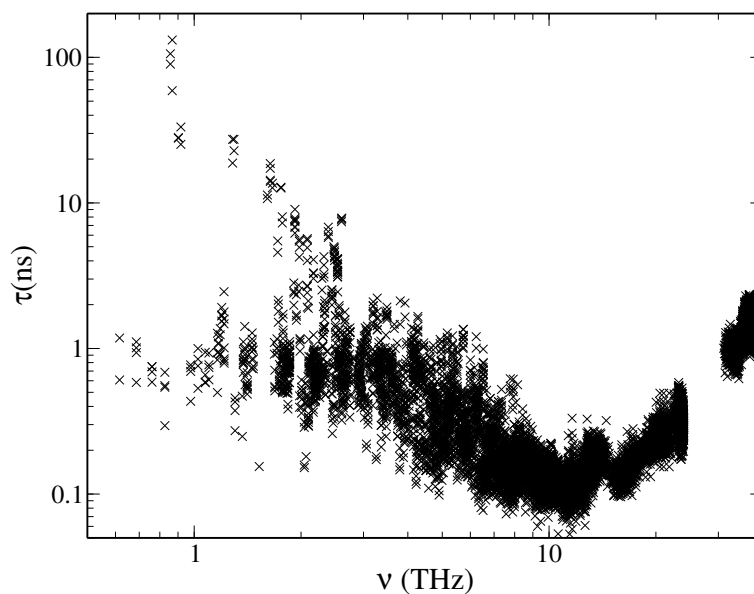


Figure 3.4.10: Calculated lifetimes of vibrational modes as a function of frequency for a crystalline α -cristobalite sample, computed with cells of 4116 atoms.

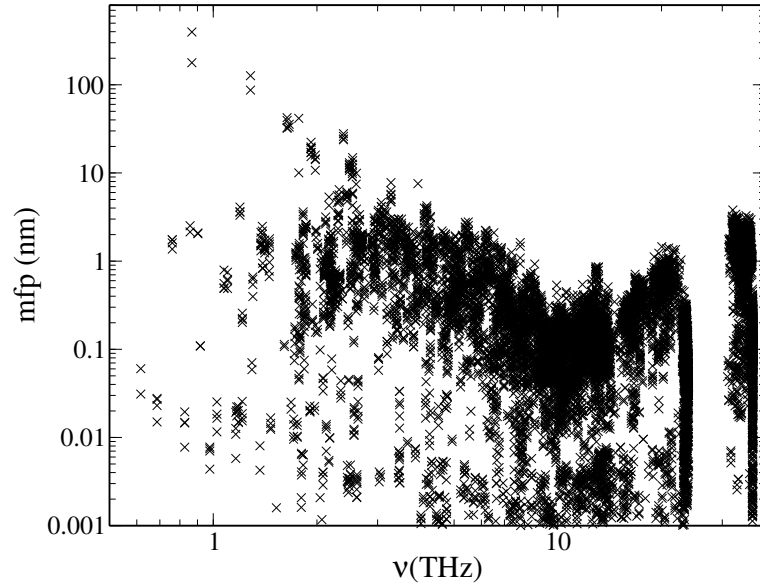


Figure 3.4.11: Calculated mean free paths of vibrational modes as a function of frequency for a crystalline α -cristobalite sample, computed with cells of 4116 atoms.

contribute to 60% of κ , where we have defined modes with $\lambda > 2\text{\AA}$ as propagating modes; non-propagating modes contribute to the remaining 40% of the conductivity.

The solutions of the BTE under the single mode relaxation time approximation may not effectively describe the vibrational modes with λ smaller than interatomic distances. These modes are non-propagating, and usually found in disordered systems. Consistent with our results, also McGaughey and Kaviany [71] found that there are two independent thermal transport mechanisms in quartz, giving rise to two contributions to the thermal conductivity, one which is temperature-independent and the other one which is temperature-dependent. They suggested to develop a model for the conductivity of crystalline silica based on the Allen-Feldmann theory [43] described in Chapter 2.3.3. However we found here that the use of the Allen-Feldman approximation is not straightforward for SiO_2 . Unlike the case of amorphous silicon, Fig 3.4.13 shows that the κ of α -cristobalite is very sensitive to the Lorentzian

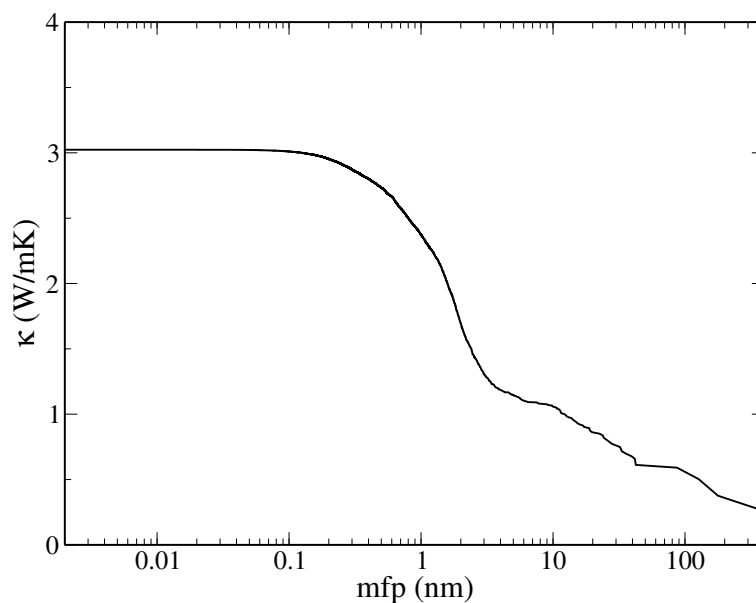


Figure 3.4.12: Thermal conductivity of a crystalline α -cristobalite sample at 300K computed from the formula $\sum_{mfp}^{\infty} c_i v_i \lambda_i$, as a function of the maximum mean free path (mfp), included in the summation: the index i denotes vibrational modes. Calculations were performed in a cell with 4116 atoms.

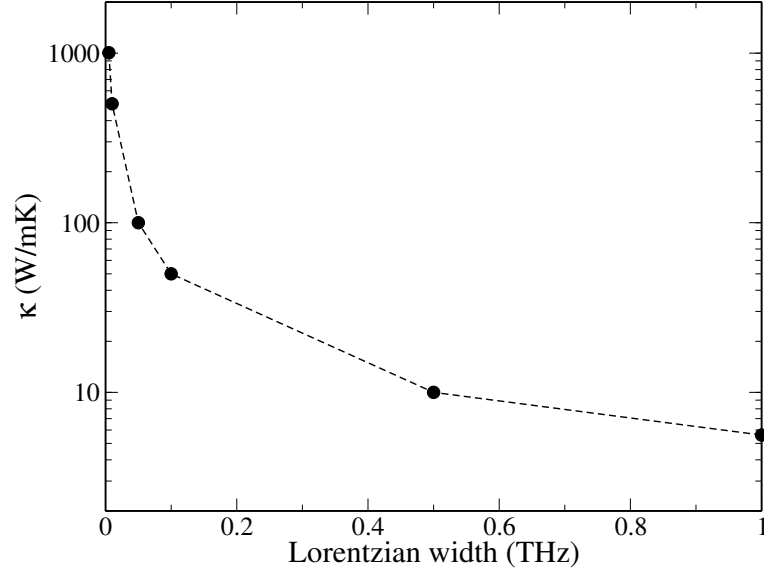


Figure 3.4.13: Thermal conductivity of a crystalline α - cristobalite sample calculated for a sample with 4116 atoms, using the Allen-Feldman formula, as a function of the Lorentzian width used to evaluate the diffusivity.

width η used in the calculation of the diffusivity (see Eq. 2.3.43). The κ obtained by choosing η larger than the maximum spacing of the frequency spectrum is about 10 W/mK, which is much larger than the value calculated by EMD. Therefore, the AF model may not be suitable to describe the heat transport in crystalline α -cristobalite.

Chapter 4

Heat transport in disordered bulk materials

4.1 Background and objectives

The study of thermal transport in disordered systems is much less advanced, from a theoretical standpoint, than that of ordered systems. Different types of modes contribute to the conductivity of disordered solids, not only phonons (that is propagating vibrations) as in ordered systems. In this chapter we describe our study of disordered materials, in particular amorphous Silicon, SiGe alloys and amorphous silica and we analyze the microscopic origin of their thermal conductivity.

4.2 Thermal transport in amorphous silicon

Thermal transport in amorphous silicon (*a*-Si) has been extensively investigated. Numerous experiments have appeared in the literature [84, 85, 86, 87, 88, 89, 90, 91], along with several theoretical studies [92, 93, 94, 95, 96, 97, 98], motivated not only by

thermoelectric and solar applications, but also by the broader goal of understanding heat propagation in glasses [99]. However, fundamental questions on the microscopic properties of heat carriers remain unanswered, and the apparent differences between various experimental results [84, 85, 86, 87, 88, 89, 90, 91] have not been understood.

This section presents a series of molecular dynamics (MD) and lattice dynamics calculations aimed at characterizing heat transport in *a*-Si. As shown by Allen and Feldman (AF) [93, 97, 92], the majority of heat carriers are non-propagating modes, usually called diffusive modes or diffusons. Our work showed that these carriers contribute only to about half the value of the total conductivity. A minority (3%) of long-wavelength, propagating vibrations accounts for the remaining half. In amorphous silicon, by either reducing the material thickness (below several tens of a micron), or etching holes in bulk samples, the mean free path of low frequency vibrations may be modified so as to substantially reduce κ of the bulk system. Our results were used to interpret several experiments [85, 86, 84, 91, 90] and show that a simple kinetic model is not applicable to describe thermal transport in *a*-Si at room temperature.

The κ of *a*-Si was computed using equilibrium (EMD) [35] and non-equilibrium (NEMD) molecular dynamics [39] using the DLPOLY code with the empirical potential proposed by Tersoff [30]. All *a*-Si samples were independently generated by quenching from the melt. The amorphous silicon (*a*-Si) samples were generated using an approach similar to that proposed by Bording [100]. We carried out both EMD and NEMD simulations. We first describe EMD results. We generated four samples with the following number of atoms in the unit cell: 512, 4096, 13824 and 17576. In equilibrium molecular dynamics simulations, a bulk crystalline silicon sample was heated up to 3500K within a NPT ensemble [101](constant pressure and temper-

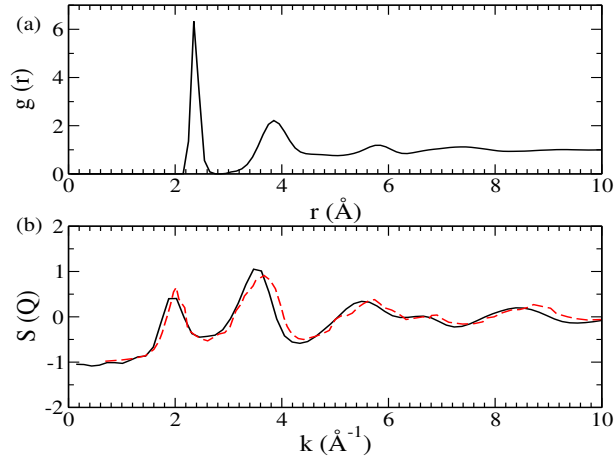


Figure 4.2.1: (a) Radial distribution function ($g(r)$) of a -Si (4096 atoms) generated by MD simulations (b) Structure factors of the MD generated a -Si model (4096 atoms), obtained by the Fourier transform of the $g(r)$ (black solid curve), and of evaporated a -Si measured by neutron diffraction (red dashed curve) [103]

ature). We note that the melting temperature for silicon modeled by the Tersoff potential is about 2500K, this is greatly overestimated compared to the experimental value (the experimental value of the melting temperature of Si is 1683K). The molten state was first cooled down to 1400K, and annealed for a time (20ns) long enough to avoid being trapped into a supercooled states. The experimental value of the density (ρ_a) of a -Si is estimated to be 97 % of that of bulk crystalline silicon (ρ_c) [102]. The density of the all generated amorphous silicon samples in our MD is 2.26 g/cm^3 , which is 97.5 % of the density of the crystalline silicon sample optimized using the same Tersoff potential. Fig. 4.2.1(a) shows the calculated pair correlation function $g(r)$ of a -Si model generated in our MD simulation with 4116 atoms. Fig. 4.2.1(b) shows a comparison between the structure factors $S(k)$ obtained in our simulations and the one measured by neutron diffraction[103].

The agreement between computed and measured $S(k)$ is good, considering the fast cooling rate [100] used in our MD simulations and the approximation introduced by

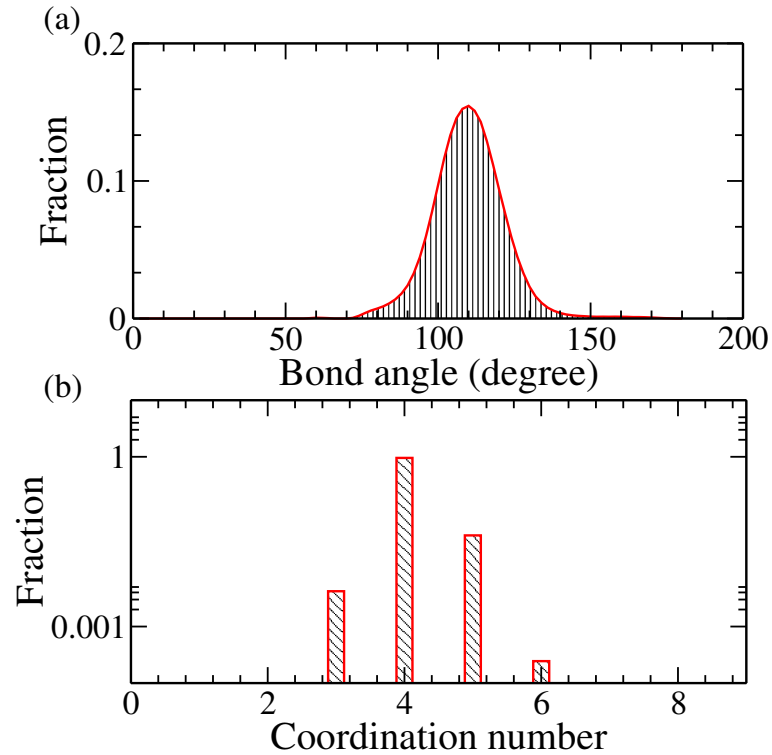


Figure 4.2.2: (a) Angle distribution function of the *a*-Si model obtained using MD simulations with cells with 4096 atoms; (b) Coordination number distribution of the generated *a*-Si model.

the use of a model of interatomic potential [30].

Fig. 4.2.2 shows the calculated bond angle distribution and coordination numbers of our model sample. The peak of the bond angle distribution is at 109.33° , which is consistent with the bond angle in a regular tetrahedral structure. We find that 95.5 % of atoms are fourfold coordinated in our *a*-Si sample as shown in Fig. 4.2.2 (b), indicating that the sample is indeed a tetrahedrally coordinated amorphous semiconductor. All the physical properties were calculated by averaging over five statistically independent *a*-Si samples (each one with 4096 atoms), corresponding to five statistically independent runs.

In EMD simulations, κ was obtained from the time integral of the heat current(\mathbf{J})

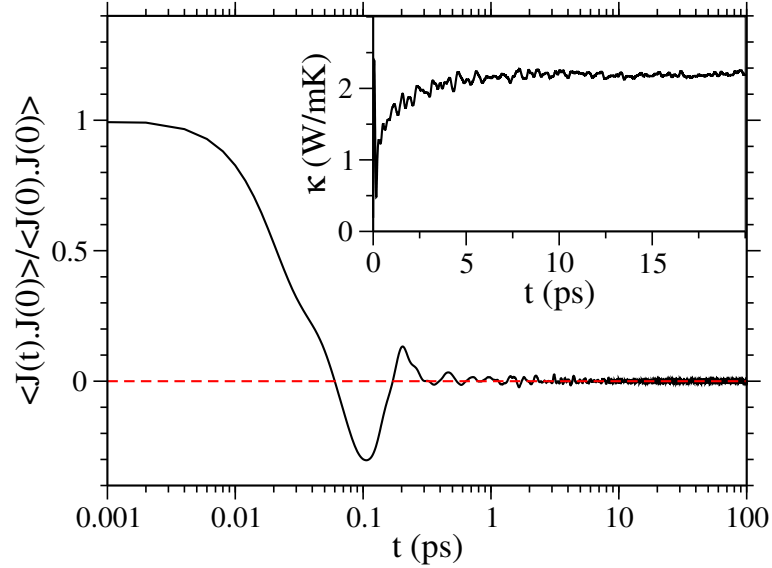


Figure 4.2.3: The time variation of the normalized heat current autocorrelation function and the thermal conductivity of an *a*-Si sample (4116 atoms) as a function of truncation time.

autocorrelation function (HCACF), using the Green-Kubo relation (Eq. 2.2.22) based on the fluctuation, dissipation theorem [35]. Fig. 4.2.3 shows a normalized HCACF and an accumulated κ for the *a*-Si sample with 4096 atoms. The time dependence of HCACF and its integral (κ) are consistent with findings reported by McGaughey and Kaviani in Lennard-Jones amorphous argon [42]. In amorphous systems, the HCACF shows a very different behavior than in crystals. It drops below zero in its initial decay, then converges to zero with oscillations between positive and negative values. The integral of HCACF converges with 10ps truncation time as shown in Fig. 4.2.3. Our results showed that it is necessary to consider samples with about 20,000 atoms to obtain a reasonably well converged value of κ from EMD (see Fig. 4.2.5 (a)).

We also carried out NEMD simulations (see Fig. 4.2.5 (b)) and independently generated five samples with 7680, 12800, 23040, 46080 and 58880 atoms each. Fig.

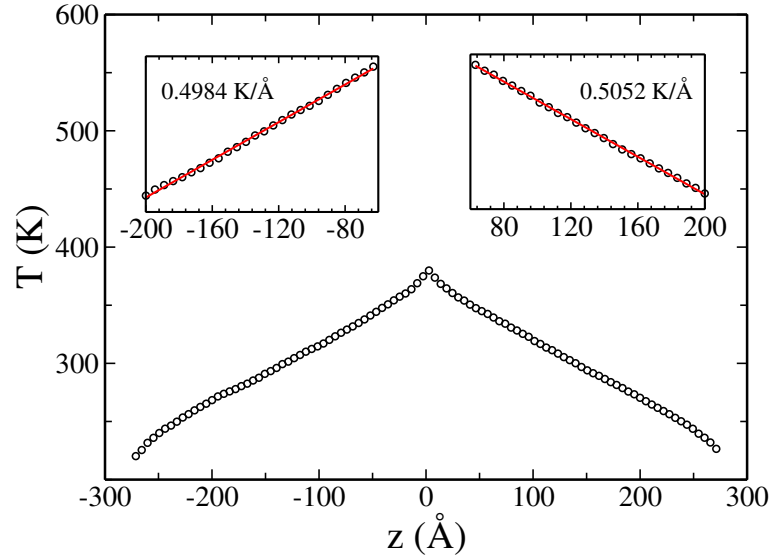


Figure 4.2.4: Temperature profile of an *a*-Si sample with 12800 atoms at 300 K. Insets show the least square fits of temperature profiles.

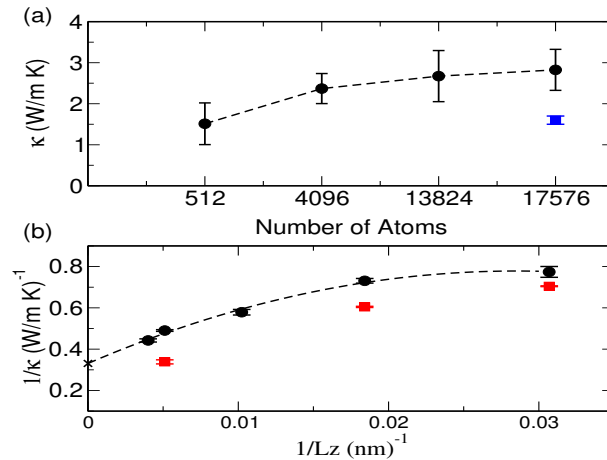


Figure 4.2.5: (a) Thermal conductivity (κ) of *a*-Si computed using equilibrium molecular dynamics (MD) as a function of the number of atoms in the supercell. Each point is an average over 5 independent samples. The blue square corresponds to a sample with holes (see text). (b) Inverse of κ computed using non-equilibrium MD, as a function of the inverse lateral dimension (L_z) of the sample used in our simulations. Circles and squares denote results for fully amorphous systems, and for systems obtained by periodically repeating a 512 supercell, respectively. For the five annealed samples, from right to left, the number of atoms and thickness of the system range from 7680, to 58880, and from 33nm to 250nm, respectively.

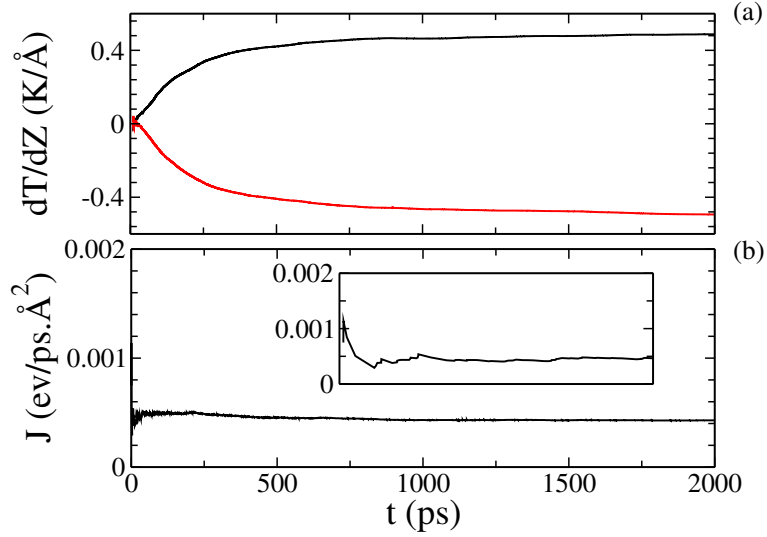


Figure 4.2.6: (a) Computed temperature gradient as a function of simulation time in the same a -Si sample as the one reported in Figure 4.2.5. The black solid curve shows the fitted temperature gradient on the left of the temperature profile. The red solid curve shows the fitted temperature gradient on the right of the temperature profile. (b) Computed heat flux as a function of simulation time. The inset shows the heat flux in the first 20ps of the simulation.

4.2.4 shows the calculated temperature profile of an a -Si sample with 12800 atoms (unit cell size : $2.17 \times 2.17 \times 54.3$ nm). The calculated heat current and temperature gradient in the same sample are shown in Fig. 4.2.6.

In order to use the Fourier's law to calculate κ , one has to find a linear response regime, which is affected by the amount of imposed heat flux in the simulations. In our approach, the imposed heat flux is determined by the interval w (number of steps) between kinetic energy exchanges and the cross section ($L_x \times L_y$) of the system. A unit cell of $2.17 \times 2.17 \times 10.8$ nm was chosen to check the relationship between the heat flux and temperature gradient using several w values ($w=20, 40, 60, 80, 100$). The results show that a linear relationship between heat flux and temperature gradient is found even for the small value of $w = 20$ corresponding to $J = 6.4 \text{ W}/m^2$. Hence, in

all of NEMD simulations for *a*-Si, we chose the cross-section of 2.17x2.17 and $w=20$.

In NEMD, the mean free path of heat carriers is limited to about half of the cell size (L_z) in the direction of heat propagation, due to boundary scattering at heat reservoirs. Therefore to obtain the macroscopic limit of the thermal conductivity (κ_∞), it is necessary to extrapolate the computed values (κ_{MD}) as a function of increasing L_z . In general $1/\kappa_{MD}$ is a non linear function of $1/L_z$; however a linear extrapolation of the type $1/\kappa_{MD} = 1/\kappa_\infty + \frac{A}{L_z}$, (where A depends on the density and speed of sound of the material) may be justified in cases where an average mean free path of majority carriers, all of the same type, may be defined, i.e. in cases where there is one type of majority carriers with frequencies falling in a narrow range; the extrapolation may also be justified when L_z is larger than the longest vibrational mean free path [55]. As discussed below, in *a*-Si two distinct types of modes are present (propagating and quasi-stationary) and thus a linear extrapolation may lead to an underestimate of the value of κ obtained by NEMD. Therefore, several simulations with large systems are needed, with thickness up to about $0.25 \mu m$ (60,000 atoms), so as to have a significant MD data set to fit by using a quadratic fit. We obtained $\kappa \simeq 3.0$ W/m K which is fully consistent with our EMD result (κ : 2.8 ± 0.5 W/m K). The size converged MD simulations yield a value of κ in much closer agreement with experiments on bulk samples (see Tab. 4.2.1) than former studies based on lattice dynamics [92], and/or using smaller MD cells [94] ($\kappa \sim 1$ W/m K).

The NEMD data provide interesting information on the dependence of κ on order at the mesoscopic level, and on the sample thickness. The results represented by the red squares in Fig. 4.2.5(b) have been obtained with supercells built by periodically repeating a 512 atoms *a*-Si cell, instead of generating the sample by quenching from the melt for each system size. These values of κ are systematically higher than those

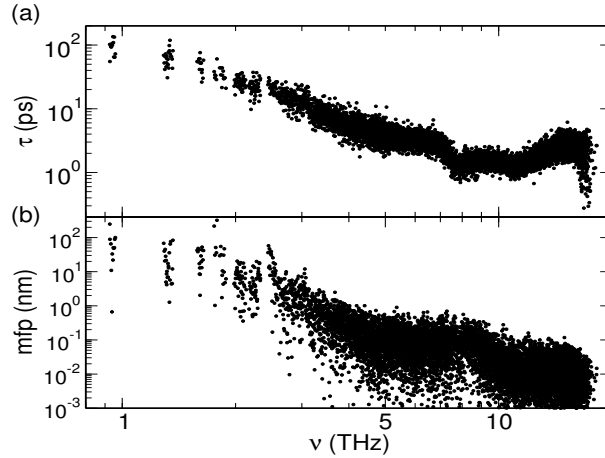


Figure 4.2.7: (a) Lifetimes τ (b) and effective mean free path (mfp) of the vibrational modes of an a -Si sample with 4096 atoms as a function of frequency ν . The sample is one of those used in equilibrium MD simulations (see Fig. 4.2.5).

of fully annealed systems (black dots), indicating that medium range order (over few nm) contributes to increasing the thermal conductivity of a -Si. The increase found in the specific case of the simulation is substantial: from 3 to 4.1 W/m K. Fig. 4.2.5(b) also shows that κ of a 0.1 μm film ($L_z = 100$ nm) is lower (1.7 W/mK) than that of a bulk sample (~ 3.0 W/mK), indicating a dependence of κ on film thickness (t_f), consistent with several measurements. A strong dependence on t_f up to $2\mu m$ was reported by Kuo et al. [88], but it was later dismissed by several authors (e.g. Ref [104]), who however investigated $\kappa(t_f)$ for $t_f \geq 2 \mu m$. Several experimental results for low H content a -Si are reported in Tab. 4.2.1. Samples with $t_f \leq 1\mu m$ appear to have conductivity of ~ 2 W/mK or lower, whereas κ of thicker films may reach values between 4 and 6 W/mK, depending, presumably, on the amount of order both at the atomistic and mesoscopic scale.

To analyze the physical origin of κ and the reasons for the observed thickness dependence, lattice dynamics calculations were carried out, which can yield effective

Table 4.2.1: Measured values of the thermal conductivity κ as a function of film thickness (t_f) and preparation conditions, compared to the results obtained in our simulations. Chemical vapor deposition (CVD) and low pressure CVD (LPCVD) data are shown. Hydrogen content (between brackets) is believed to be negligible when not specified.

κ (W/mK)	t_f (μm)	Prep.Cond.(H-cont.)	Ref.
1.8	0.1~0.3	sputtered	[84]
2	0.13	e-beam	[85]
~2	0.2	HWCVD	[86]
~1.8	0.27	e-beam	[85]
≤ 2.0	0.52	sputtered(1%)	[87]
1~4	0.4~2.0	sputtered	[88]
1.5~2.4	0.5~2	LPCVD	[89]
~ 4	1.2	thermal evap.	[91]
4~6	1.6~2.8	HWCVD	[86]
4.8 \pm 0.5	2~3.6	CPCVD	[91]
~ 4	80	HWCVD (1%)	[90]
1.7	0.1	melting-annealing	this work
3.0	bulk	melting-annealing	this work

group velocities (v), lifetimes (τ) and effective mean free paths (λ) of vibrational modes. The elements of the $3N \times 3N$ dynamical matrix were obtained by computing the derivatives of atomic forces by finite differences, and eigenvectors and eigenvalues were computed by direct diagonalization. Effective group velocities ($\frac{\Delta\omega}{\Delta q}$) were calculated by differentiating dispersion curves $\omega(q)$ over a grid of about 20 points close to the Γ point. In a disordered system, at Γ $v_g = 0$, except for the three acoustic modes; however in the case of *a*-Si, inspection of dispersion curves shows that low frequency modes are indeed propagating and one can define an interval $\Delta\omega(q)$ in close proximity of Γ over which $\frac{d\omega(q)}{d(q)}$ is well defined and finite. We therefore defined effective group velocities as $\frac{\Delta\omega}{\Delta q}$, without taking the limit $q \rightarrow 0$.". Lifetimes were obtained from the normalized autocorrelation function of the eigenmode energies [105](Eq. 2.3.27).

Fig. 4.2.7 (a) and (b) show the computed lifetimes and effective mean free paths of all the vibrational modes of an *a*-Si sample with 4096 atoms, respectively. Such a number of atoms is sufficient to yield a reasonably well converged density of vibrational states as shown in Fig. 4.2.8. At low frequency ($\nu \leq 3$ THz), the minority of modes have effective mean free paths larger than 10 nm, with some up to about 0.5 μm (possibly up to 1 or several μm , if computed with larger supercells). These are propagating vibrations whose mean free paths (λ_{ph}) is determined by phonon-phonon scattering, in the absence of defects and boundaries in the system. The majority of vibrations above 3 THz, have instead effective mean free paths smaller than interatomic distances and thus they are effectively non propagating or quasi-stationary modes, also called diffusons, following Ref. [97]. Diffusons are very weakly localized and overlap with each other and hence they transport heat, although in a manner much less efficient than propagating vibrations, and by a different mechanism (energy transfer). In qualitative agreement with AF [97], we find that the majority (95%) of heat carriers are quasi-stationary modes in *a*-Si, while only a small proportion of carriers (3%) are propagating (the rest are localized high frequency modes not contributing to thermal transport). The contribution of diffusons (κ_{AF}) to the total value of κ can be evaluated by using the theory proposed by AF [97], and that of propagating modes (κ_{BTE}) by using non self-consistent solutions of the Boltzmann transport equation (BTE): $\kappa_{AF} = \sum_i c_i D_i$ where c_i is the specific heat per unit volume and the diffusivity of mode i is given by: $D_{i\alpha} = \frac{V^2}{8\pi^2 \hbar^2 \nu_i^2} \sum_{j \neq i} | \langle \mathbf{e}_i | J_\alpha | \mathbf{e}_j \rangle |^2 \delta(\nu_i - \nu_j)$, where ν denotes the mode frequency, $\langle \mathbf{e}_i | J_\alpha | \mathbf{e}_j \rangle$ is the α -th component of the heat current operator projected on eigenvectors \mathbf{e}_i and \mathbf{e}_j . Within a single mode relaxation time approximation, $\kappa_{BTE} = \sum_i c_i v_i^2 \tau_i$. The relative contributions of κ_{AF} and κ_{BTE} are shown in Fig. 4.2.9, where it is seen that propagating vibrations contribute to

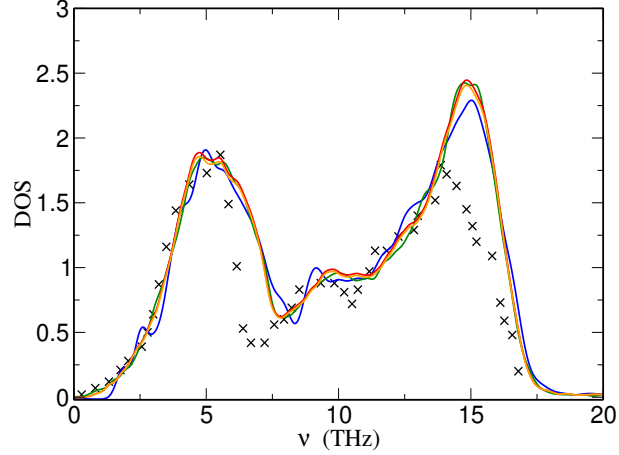


Figure 4.2.8: Vibrational density of states (DOS) of *a*-Si computed from velocity-velocity correlation functions for several system sizes, compared with experimental results (black line) [106]. Orange, green, red and blue curves are for samples with 17576, 13824, 4096 and 512 atoms, respectively. Note the absence of low frequency (ν) modes in the DOS of the 512 atoms sample.

about half of the value of the total thermal conductivity, and diffusons account for the remaining half. The contribution of propagating modes is much more substantial than predicted in previous simulations based on small MD cells or by previous lattice dynamics calculations [94, 97, 92]. The same results were approximately obtained for κ_{AF} when using the 512 or 4096 atoms sample: $\kappa_{AF} \simeq 1/2\kappa$, where κ is the converged value from our MD simulations (see Fig. 4.2.5 (a)). Therefore, the convergence of κ_{MD} as a function of cell size is mainly determined by the convergence of κ_{BTE} .

The presence of long- λ waves in *a*-Si is responsible for the observed dependence of κ on t_f , and the observed decrease of the thermal conductivity for $t_f \leq 1\mu m$. The results are in agreement with those of Ref. [90], showing that modes with λ up to 0.6 micron contribute to κ , and that Time Domain Thermo-reflectance data depend on frequency. Our findings are also in accord with those of Ref. [85], reporting data for samples 0.1-0.27 μm thick (see Tab. 4.2.1). These authors find values of $\simeq 2$

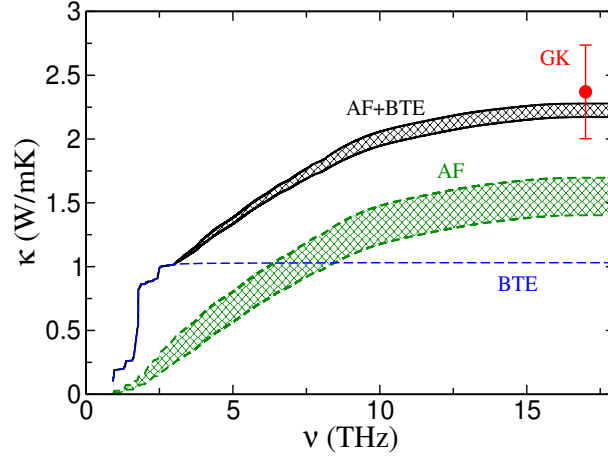


Figure 4.2.9: Contributions to the thermal conductivity of vibrational modes as a function of frequency ν for the *a*-Si sample with 4096 atoms. GK denotes the value obtained using equilibrium Molecular Dynamics. The total conductivity obtained by lattice dynamics is computed as: $\kappa = \kappa_{AF} + \kappa_{BTE}$ (see text) [107]. The AF, BTE and AF+BTE curves denote $\kappa_{AF}(\nu)$, $\kappa_{BTE}(\nu)$ and $\kappa(\nu)$, respectively. The dashed areas represent the uncertainties associated with the calculation of κ_{AF} .

W/mK, consistent with the results in this work for a 0.1 μm thin film (see Fig. 4.2.5 (b)). However, comparison with experiment is not completely straightforward. For example, the macroscopic density ρ of experimental samples is not known with great accuracy, and one might expect that varying ρ and the medium-range structure of *a*-Si may lead to some variation of its thermal conductivity.

Another possibility of decreasing κ of bulk *a*-Si may come from etching nano-holes in the sample. Building on the recent study of nanoporous crystalline Si [108], The MD simulations were carried out for samples with porosity $\phi=0.07$ (diameter of pore $d_p=2.2$ nm; distance between pore $d_s=4.8$ nm), where ϕ is defined as $\phi=\pi d_p^2/(2d_p+2d_s)^2$. With respect to bulk samples, the conductivity of nanoporous *a*-Si is decreased by almost a factor of 2 in the direction perpendicular to the pores (see Fig. 4.2.5 (a)) while it is only weakly affected in the parallel direction. The presence of pores affects again the mean free path of propagating modes, greatly decreasing the κ_{BTE}

contribution to the total conductivity.

4.3 Thermal transport in silicon germanium alloy

Silicon germanium (SiGe) alloys are systems with structural order but mass and chemical bond disorder. They are promising candidates for thermoelectric applications due to their low thermal conductivity. As mentioned in the introduction, they have long been used to build thermoelectric modules for the international Solar Polar mission to convert radio-isotope heat into electricity [109, 110]. However, the efficiency of thermoelectric devices built from bulk SiGe alloys is still not large enough to make them competitive with conventional generators, and they can only work efficiently at high temperature. Recent progress in nanotechnology has triggered interest in trying to reduce the thermal conductivity of bulk silicon germanium alloys by using low dimensional and nano-confined structures.

NEMD simulations have been used to estimate the thermal conductivity of bulk silicon germanium [111], but failed to yield results in good agreement with experiments. On the other hand, a recent anharmonic lattice dynamics study, based on first principle density functional perturbation theory [112] has successfully reproduced the experimental κ of bulk silicon germanium. However the cell used in the first principle study are of moderate sizes. In our work we carried out equilibrium molecular dynamics (EMD) calculations of the thermal conductivity of bulk silicon germanium at stoichiometric compositions, and an analysis using lattice dynamics. Our goal is twofold: (i) to establish the validity of MD in predicting the conductivity of SiGe; (ii) to analyze the microscopic origin of κ in mass disordered systems.

Our work mainly focuses on the study of thermal transport in $\text{Si}_{0.5}\text{Ge}_{0.5}$. The heat current was computed using Eq. 2.2.28 in LAMMPS code with 10ns long sim-

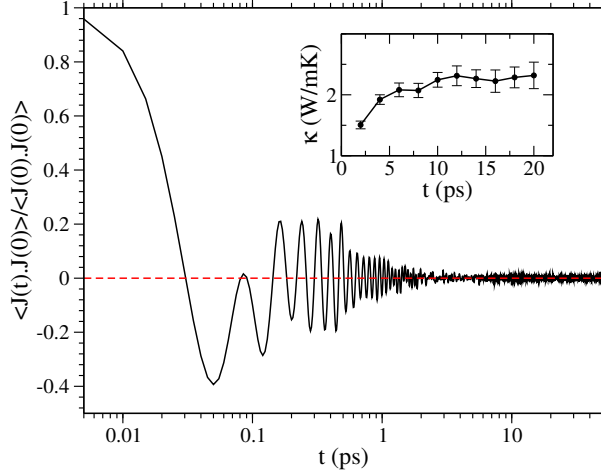


Figure 4.3.1: The normalized heat current auto-correlation function for a stoichiometric SiGe sample with 4096 atoms at 300K. The inset shows the calculated thermal conductivity as a function of the truncation time.

ulations in the NVE ensemble with a time step of 0.5fs. The thermal conductivity was calculated using the Green-Kubo formula (Eq. 2.2.22). Contrary to c-Si and c-Ge, where the truncation time was found to be independent on the size of the system, we find that in $\text{Si}_{0.5}\text{Ge}_{0.5}$, the truncation time strongly depends on the size of the simulation cell, varying from 20ps to 400ps for systems with 1000 through 2 million atoms. Fig. 4.3.1 shows the calculated heat current auto-correlation function (HCACF) for a $\text{Si}_{0.5}\text{Ge}_{0.5}$ sample with 4096 atoms. To test the convergence of κ of $\text{Si}_{0.5}\text{Ge}_{0.5}$ with respect to the system size, we carried out simulations with supercells containing 1000(5x5x5), 4096 (8x8x8), 8000 (10x10x10), 64000 (20x20x20), 216000 (30x30x30) and 1728000 (60x60x60) atoms (see Fig. 4.3.2). The larger cells mean also more disordered and realistic systems. We find that we can not obtain a fully converged thermal conductivity of $\text{Si}_{0.5}\text{Ge}_{0.5}$ even when using an extremely large cell with about 2 million atoms. However, our extrapolated value is consistent with existing measurements contrary to the results reported using NEMD [113].

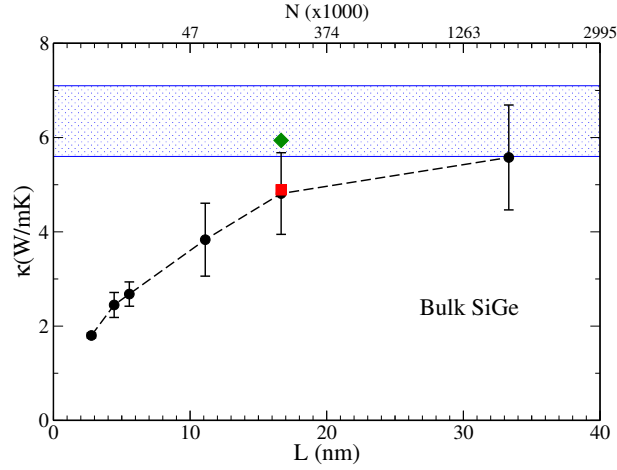


Figure 4.3.2: Thermal conductivity of $\text{Si}_{0.5}\text{Ge}_{0.5}$ alloy as a function of supercell sizes at 300 K, computed using Green-Kubo simulation. Black circles represent results for true $\text{Si}_{0.5}\text{Ge}_{0.5}$ with different masses and different bond descriptions; Red square represents system with different masses, but the same bond description using the Ge Tersoff potential (GeGe); Green diamond represents system with different masses, but the same bond description using the Si Tersoff potential (SiSi); Blue shaded region indicates the range of measured κ of $\text{Si}_{1-x}\text{Ge}_x$ in experiments, $x=0.2\sim 0.3$ [114, 115].

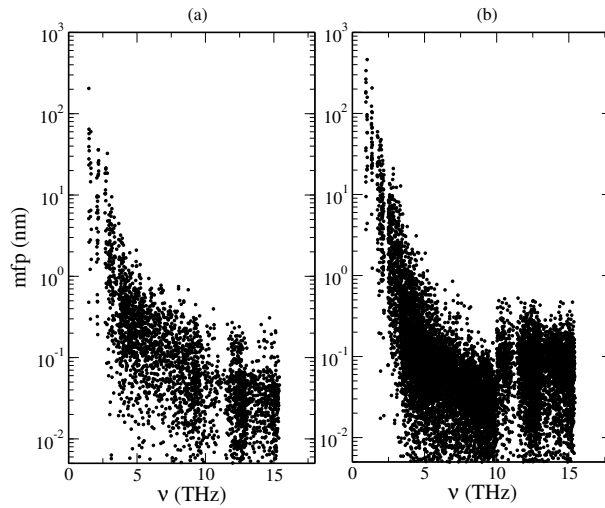


Figure 4.3.3: Mean free paths of vibrational modes in $\text{Si}_{0.5}\text{Ge}_{0.5}$ computed with cells with 1000 atoms (a) and cells with 4096 atoms (b)

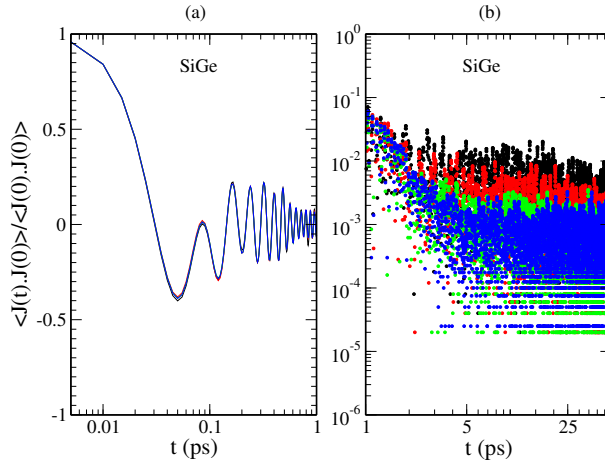


Figure 4.3.4: The normalized heat current autocorrelation function of $\text{Si}_{0.5}\text{Ge}_{0.5}$ samples with various sizes. The black, red, green and blue curves represent cells with 1000, 8000, 216000 and 1728000 atoms, respectively. (a) and (b) show the correlation function between 0 and 1 ps and between 5 and 25 ps, respectively.

To understand the convergence issues encountered in MD simulations, and the microscopic properties of heat carriers in $\text{Si}_{0.5}\text{Ge}_{0.5}$, lattice dynamics (LD) calculations were carried out on samples with two different sizes, 1000 and 4096 atoms. The calculated mean free paths of the two systems (see Fig. 4.3.3) show that when the size of the simulation cell is increased, an increasing number of low frequency modes is explored, and these low frequency modes have quite large mean free paths, while the mean free paths of high frequency modes in both systems are very similar and much smaller than at low frequency. These results indicate that the low frequency modes are responsible for the size-dependence observed in our MD results. Another way to analyze the size effect is to compare the decay rates of HCACF [42] for different cell sizes. The short time scale found in HCACF is associated with high frequency vibrations. The longer one is associated with low frequency vibrations.

Fig. 4.3.4 shows that the decay rate of the short time scale is similar for the different system sizes. However, the decay rate of longer time scale is significantly

different, and gradually increases as the size of the systems increases. Since the decay rate of HCACF is proportional to the lifetime of vibrations, our results indicate that the vibrations at low frequencies are responsible for the size-effect on κ observed for MD simulations of $\text{Si}_{0.5}\text{Ge}_{0.5}$. This result is consistent with our lattice dynamics (LD) studies (see Fig. 4.3.3). Both MD and LD results suggest that systems even larger than 2 million atoms should be simulated in order to achieve a converged κ of $\text{Si}_{0.5}\text{Ge}_{0.5}$. However this rises a second issue. The truncation time of HCACF in $\text{Si}_{0.5}\text{Ge}_{0.5}$ is size-dependent. For simulation cells larger than 2 million atoms, the truncation time must be larger than 400ps. Unfortunately, the density of low frequency modes in large $\text{Si}_{0.5}\text{Ge}_{0.5}$ systems is not large enough to correct for the statistical noise in the long tail of HCACF. This problem represents an open issue.

Most experimental values of κ are evaluated for $\text{Si}_{1-x}\text{Ge}_x$ samples with $x=0.2\sim 0.3$. In order to compare with experimental results, the κ of $\text{Si}_{1-x}\text{Ge}_x$ as a function of Ge fraction x was computed by using a small system with 4096 atoms, which can be used to probe the effect of Ge mass disorder on κ . We first computed lattice constants as a function of the Ge fraction x . We found that the simulated lattice constants are linearly dependent on composition, except for a small positive deviation with respect to experimental results (see Fig. 4.3.5).

Our results for the thermal conductivity (see Fig. 4.3.6) show that κ of $\text{Si}_{1-x}\text{Ge}_x$ alloy becomes composition-independent at $0.2 < x < 0.5$. Therefore, the calculated κ of $\text{Si}_{0.5}\text{Ge}_{0.5}$ is representative of and compatible with experimental results [114, 115].

To investigate whether mass disorder is the main effect in determining the low thermal conductivity of $\text{Si}_{0.5}\text{Ge}_{0.5}$, two simulations were carried out: we considered one system with the same mass disorder as in $\text{Si}_{0.5}\text{Ge}_{0.5}$, but whose Si bonds and Ge bonds are described by the Si Tersoff potential (SiSi); we then considered a system

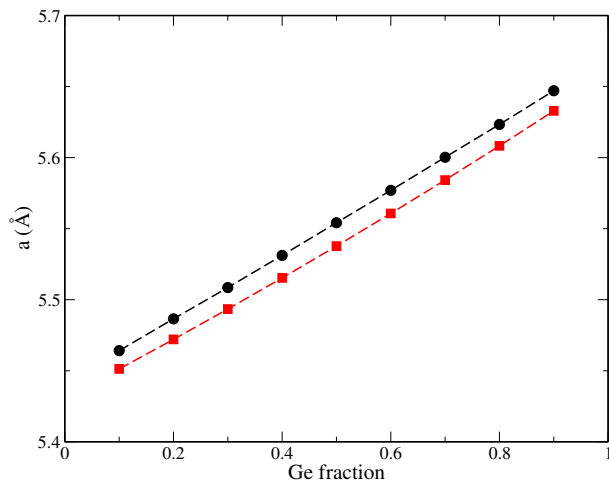


Figure 4.3.5: Lattice constant of $\text{Si}_{0.5}\text{Ge}_{0.5}$ as a function of composition. The black circles are simulation results, and the red squares are experimental results [116]

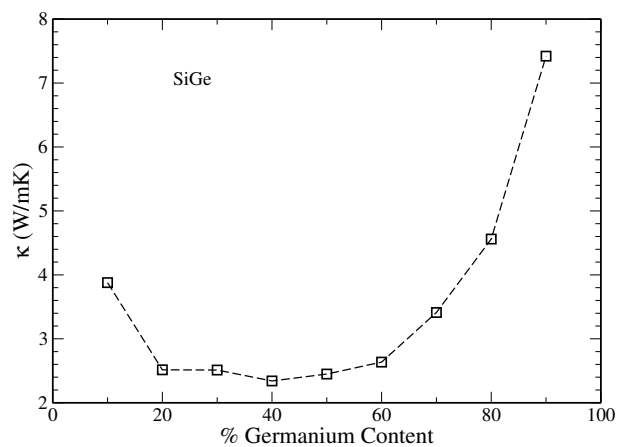


Figure 4.3.6: Composition dependence of the thermal conductivity of $\text{Si}_{1-x}\text{Ge}_x$ alloys, computed in MD simulations, using 4096 atoms at 300K.

with the same mass disorder as in $\text{Si}_{0.5}\text{Ge}_{0.5}$, but whose Si bonds and Ge bonds are described by the Ge Tersoff potential (GeGe). The results show that the difference in chemical bonds between Si and Ge plays a minor role in determining the reduction of the value of κ , while mass disorder has a major effect (see Fig. 4.3.2).

4.4 Thermal transport in amorphous silicon dioxide

Amorphous silicon dioxide ($a\text{-SiO}_2$) is a common glass material. It has been widely used in the production of optical fibers, water filtrations and DNA purification. In addition $a\text{-SiO}_2$ plays an important role in microelectronics. It is a high-quality electrical insulator and has been extensively used as a barrier material for electrical isolation of semiconductor devices, such as MOS transistors, or as an interlayer dielectric in multichip modules. As the microelectronic industry has driven toward smaller and smaller devices, thermal management of electronic devices is becoming more challenging in order to maintain the reliability of devices. Therefore, it is crucial to understand heat transport in each component substance of the devices. Since $a\text{-SiO}_2$ is an important constituent in microelectronics, understanding the heat transport in $a\text{-SiO}_2$ is of considerable interest.

Recently, various silicon-based nanostructures were fabricated, such as silicon nanowires. When the surfaces are exposed to air, an amorphous silica layer forms at the surface. This layer may significantly affect the thermal properties of the wires. Therefore, understanding the heat transport mechanisms in $a\text{-SiO}_2$ is also important to interpret the observed thermal conductivity reduction in silicon nanowire with respect to bulk Si.

Table 4.4.1: Experimental measured values of the thermal conductivity κ of amorphous silica at room temperature. t_f denotes the thickness of the film for which the measurement was performed

κ (W/mK)	t_f (μm)	density (g/cm^3)	Ref.
0.8~1	32~190nm	2.1	[119]
1.25	511 nm		[120]
1.1~1.2	1 μm		[121]
1.23	bulk	2.2	[122]
1.35	bulk		[123]

Thermal transport in a -SiO₂ has been studied by several experiments, and the measured values of the thermal conductivity are in good agreement with each other (see Tab. 4.4.1), and they appear to weakly depend on the thickness of the film. There are a few theoretical results for κ of a -SiO₂ [117, 118, 70]. In all previous theoretical studies, the thermal conductivity of a -SiO₂ was predicted by using non-equilibrium molecular dynamics. This study reports, for the first time, a series of equilibrium molecular dynamics and lattice dynamics calculations of the thermal transport properties in amorphous silica, aimed at understanding thermal transport in a -SiO₂ at the microscopic level.

All a -SiO₂ samples were independently generated by quenching from the melt following the same procedure as for amorphous silicon. We heated bulk crystalline α -cristobalite up to 6000K. The calculated mean square displacement showed that the systems have become completely liquid. We first cooled down the molten state to 1500K, and annealed it at this temperature for 30 ns. We then sequentially cooled the system down to room temperature, with a cooling rate of $\sim 10^{12}$ K/s (experimental quenching rate for amorphous material is typically 10^{3-8} K/s). The calculated density of our generated amorphous silica (a -SiO₂) is $2.28 g/cm^3$, which is similar to

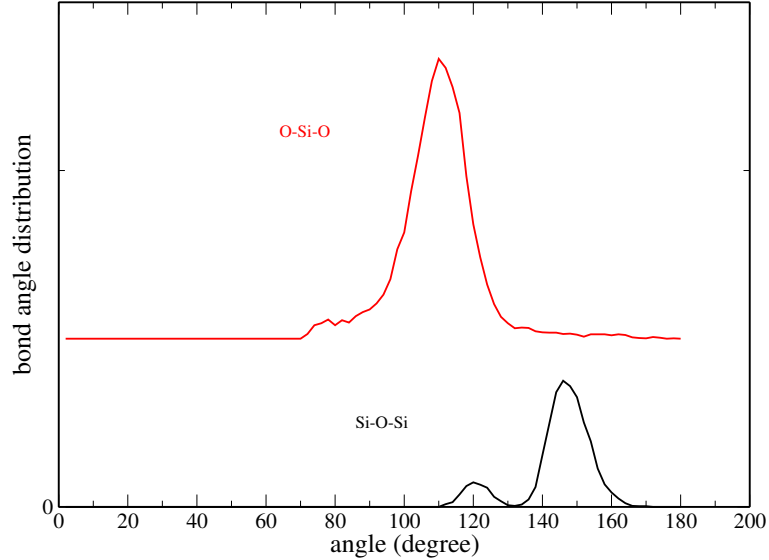


Figure 4.4.1: Computed bond angle distribution functions, Si-O-Si (black) and O-Si-O (red), for an amorphous silica sample generated in a MD simulation with 4116 atoms in the cell.

that of experimental samples (2.2 g/cm^3) [122]. To investigate the structure of the generated amorphous samples, we calculated bond angle distributions, partial radial distribution functions and coordination numbers, as shown in Fig. 4.4.1, Fig 4.4.2 and Fig. 4.4.3, respectively for a sample with 4116 atoms. All computed data are in good agreement with previous studies [124, 125, 126]. The structure factor computed from the Fourier transform of the full radial distribution function is in accord with experiment [127] (see Fig. 4.4.4).

The κ of $a\text{-SiO}_2$ was calculated using the Green-Kubo formula [35] (Eq. 2.2.22) and fast Fourier transforms. The heat current was computed via EMD simulation in the LAMMPS code and a parameterized Tersoff potential [77]. Periodic boundary conditions were applied in all three directions. The chosen time step is 0.2fs. Each sample has been first equilibrated at 300K for 500ps in the NVE ensemble. After equilibration, the computation of heat current was started using Eq. 2.2.28. The

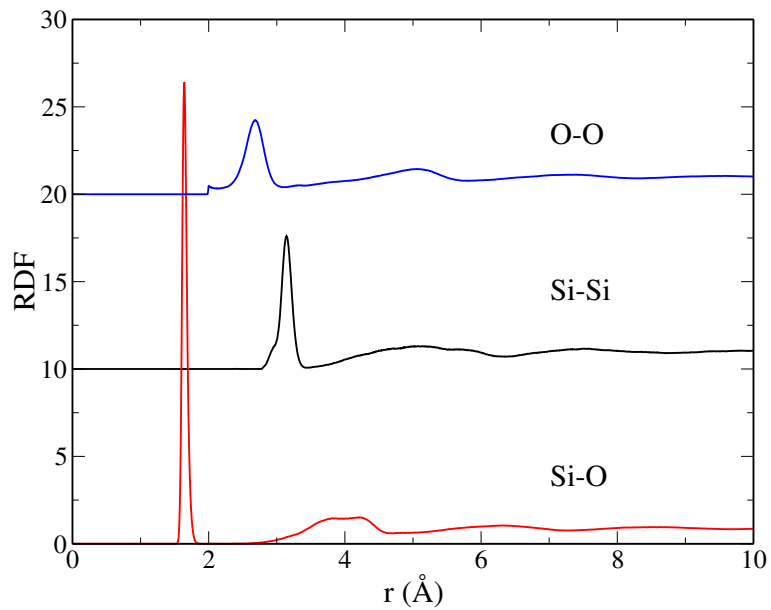


Figure 4.4.2: Computed partial radial distribution functions for an amorphous silica sample generated in a MD simulation with 4116 atoms in the cell.

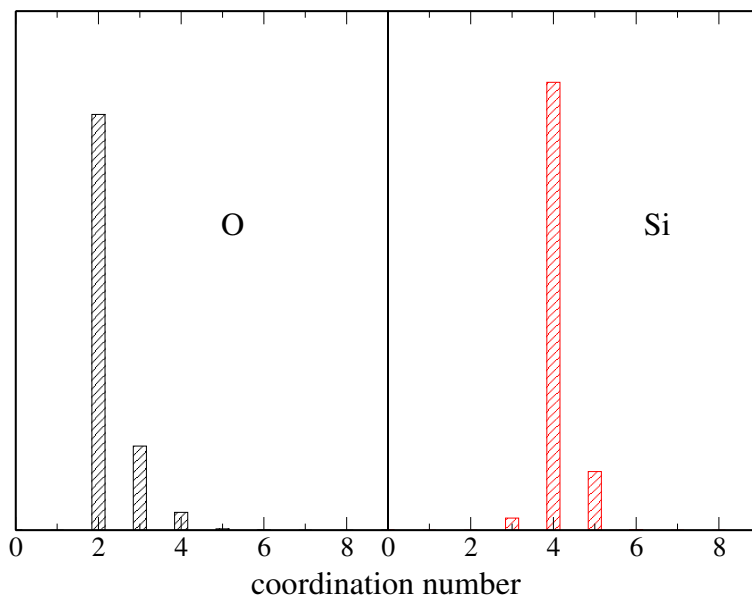


Figure 4.4.3: Computed coordination number of oxygen atoms (black) and silicon atoms (red) for an amorphous silica sample generated by MD simulations with 4116 atoms in the cell.

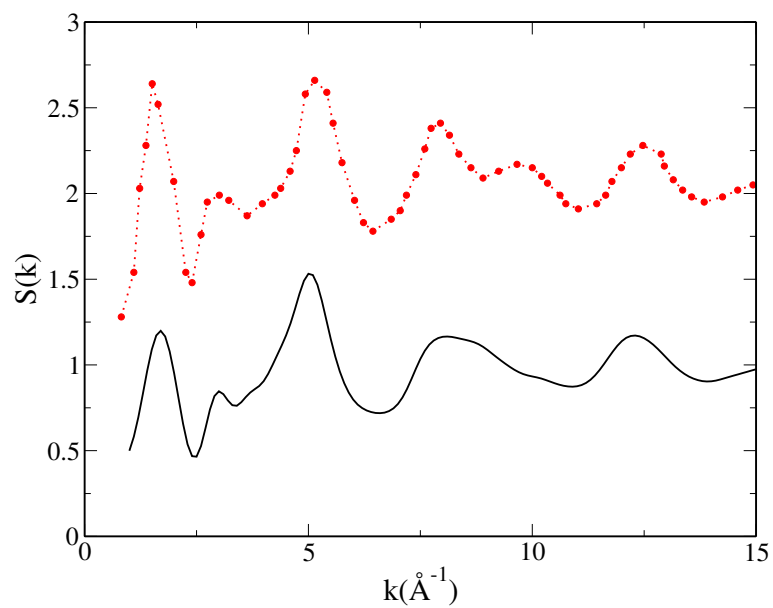


Figure 4.4.4: The structure factor ($S(k)$) of amorphous silica computed by the Fourier transform of the radial distribution function obtained in a molecular dynamics simulation with 4116 atoms (black line). The experimental $S(k)$ (D. L. Price and J. M. Carpenter, *Journal of Non-Crystalline Solids*, 92 (1987) 153-174) is shown by the red curve.

Table 4.4.2: Computed thermal conductivity of amorphous silica from equilibrium molecular dynamics (MD) as a function of the number of atoms in the simulation supercells at room temperature. For each cell size we carried out five independent runs, each 10ns long. All values of the thermal conductivity are calculated using integration of the heat current autocorrelation function (Green-Kubo formula) with 10 ps truncation time. The density of all samples is 2.3 g/cm^3 . n_1 , n_2 and n_3 denote the number of times a unit cell is repeated along the x, y, z direction, respectively.

Number of atoms in MD cells	κ (W/mK)	$n_1 \times n_2 \times n_3$
768	0.93 ± 0.04	$4 \times 4 \times 4$
4116	1.01 ± 0.01	$7 \times 7 \times 7$
8748	1.05 ± 0.04	$9 \times 9 \times 9$
20736	1.03 ± 0.02	$12 \times 12 \times 12$
49152	1.04 ± 0.03	$16 \times 16 \times 16$
96000	1.05 ± 0.01	$20 \times 20 \times 20$

convergence of κ as a function of the simulation time was carefully tested. The results show that 5 ns are sufficient to obtain a converged value of κ for amorphous silica. All MD simulations for a -SiO₂ were run for 5ns.

Fig. 4.4.5 shows a normalized heat current autocorrelation function (HCACF), and the integrated κ for an a -SiO₂ sample with 4116 atoms. The time dependence of HCACF is similar to the one found in amorphous silicon, but shows stronger oscillations. The integral of HCACF converges very fast (1 ps) with respect to that of a -Si (10ps). The calculated κ as a function of the number of atoms (N) shows that, unlike a -Si, κ of a -SiO₂ is nearly size-independent for $N > 4116$ (see Fig. 4.4.6).

To analyze the physical origin of the small value of κ obtained in EMD and the reasons for the observed thickness-independence, lattice dynamics (LD) calculations were carried out by using a system with $N=4116$ atoms. The elements of the $3N \times 3N$ dynamical matrix were obtained by computing the derivatives of atomic

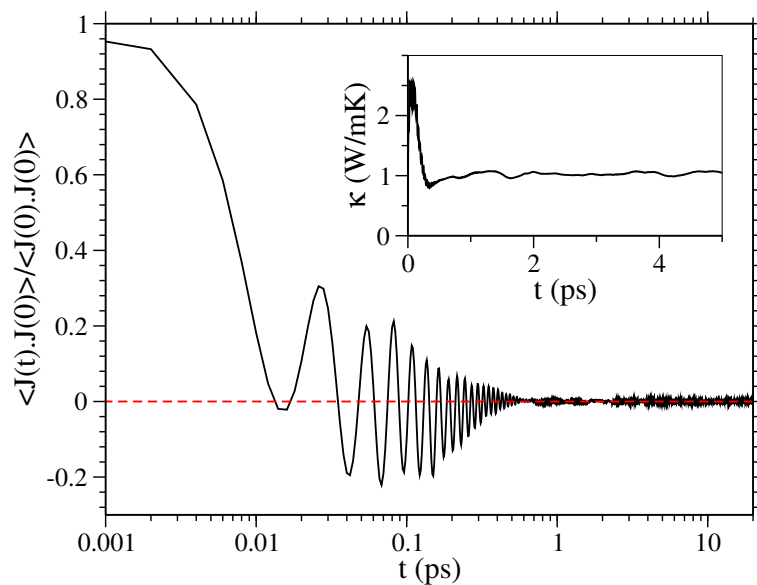


Figure 4.4.5: The normalized heat current autocorrelation function of amorphous silica as a function of correlation time at 300K. The inset shows the calculated thermal conductivity as a function of the truncation time. Simulations were carried out with cells with 4116 atoms.

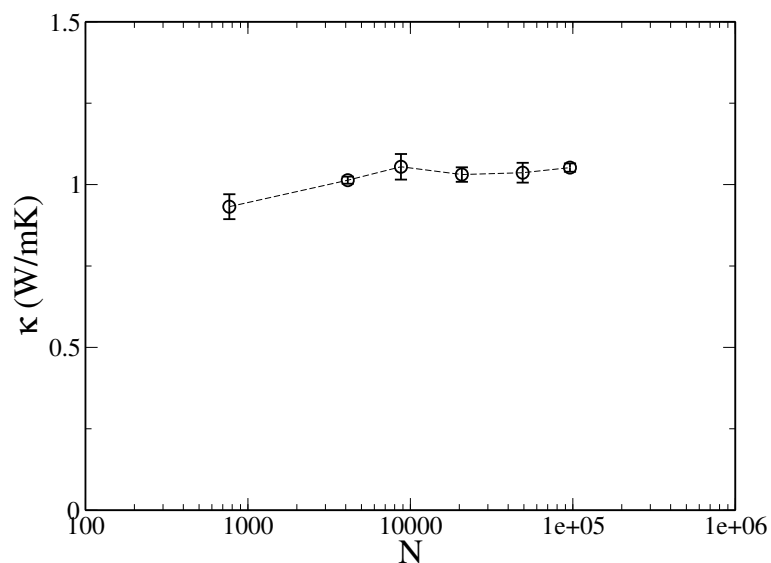


Figure 4.4.6: Thermal conductivity of amorphous silica as a function of the number of atoms in the MD cell ($N = 768, 4116, 8748, 20736, 49152, 96000$) at 300 K.

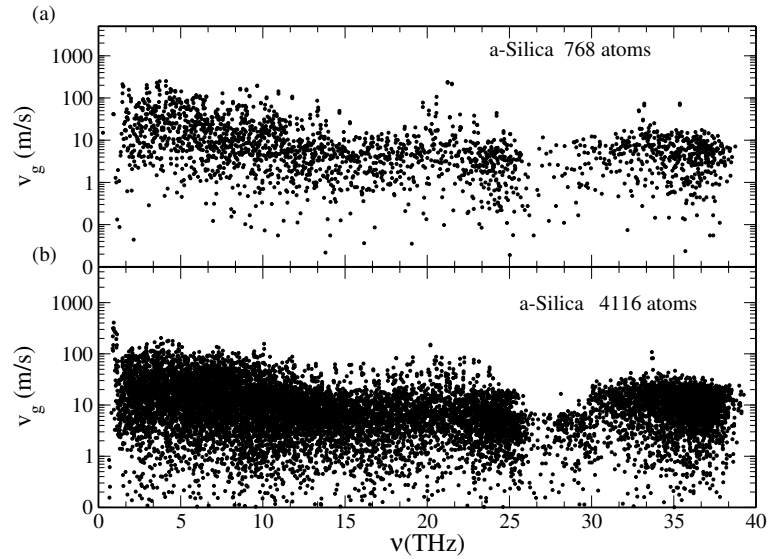


Figure 4.4.7: Calculated magnitude of the group velocities of vibrational modes as a function of frequency for amorphous silica samples with 768 atoms (a) and 4116 atoms (b), respectively.

forces by finite differences, and eigenvectors and eigenvalues were computed by direct diagonalization, following the same procedure as used for ordered solids and for *a*-Si. We find that the frequency spectra calculated from two independent methods (MD and LD) are consistent with each other. Fig. 4.4.10 shows the vibrational density of states (DoS) of our *a*-SiO₂ sample with 4116 atoms obtained by MD, which is in good agreement with experiment.

Fig. 4.4.7 shows the computed effective group velocities v_g for two systems with 768 atoms and 4116 atoms. Unlike *a*-Si where the computed v_g of the low frequency modes are strongly dependent on the size of systems, the v_g at the low frequencies in *a*-SiO₂ appear to be size-independent. A similar behavior was found for lifetime distributions (see Fig. 4.4.8) and effective mean free paths (see Fig. 4.4.9). We find that in the sample with 4116 atoms, the maximum mean free path at low frequencies is smaller than 1 nanometer. Therefore, the κ of *a*-SiO₂ computed by EMD simulations

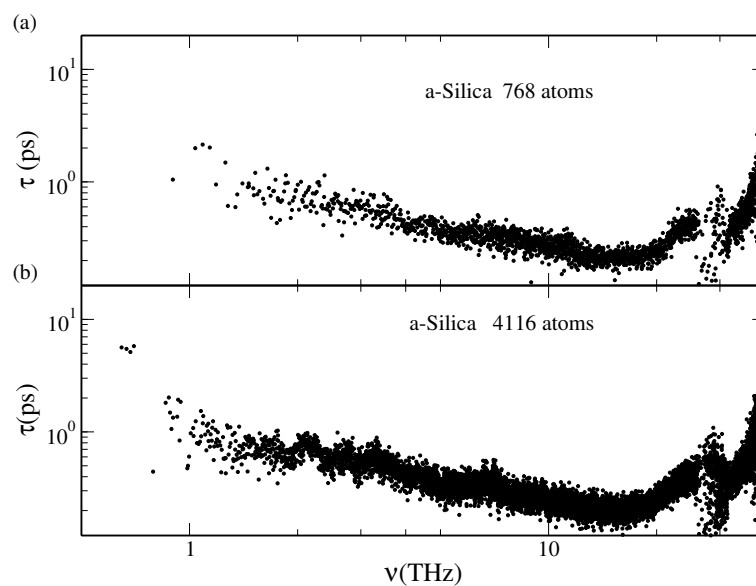


Figure 4.4.8: Calculated lifetimes of the vibrational modes as a function of frequency for amorphous silica samples with 768 atoms (a) and 4116 atoms (b), respectively.

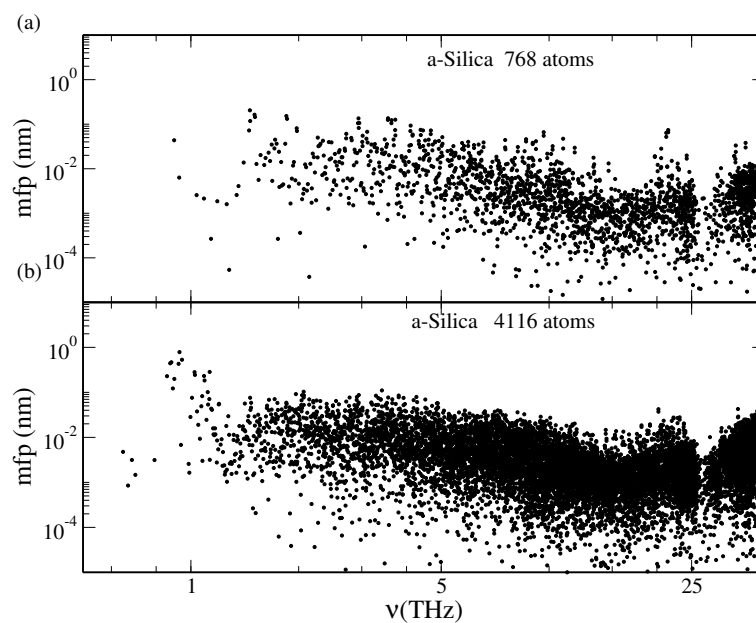


Figure 4.4.9: Calculated mean free paths of the vibrational modes as a function of frequency for amorphous silica samples with 768 atoms (a) and 4116 atoms (b), respectively.

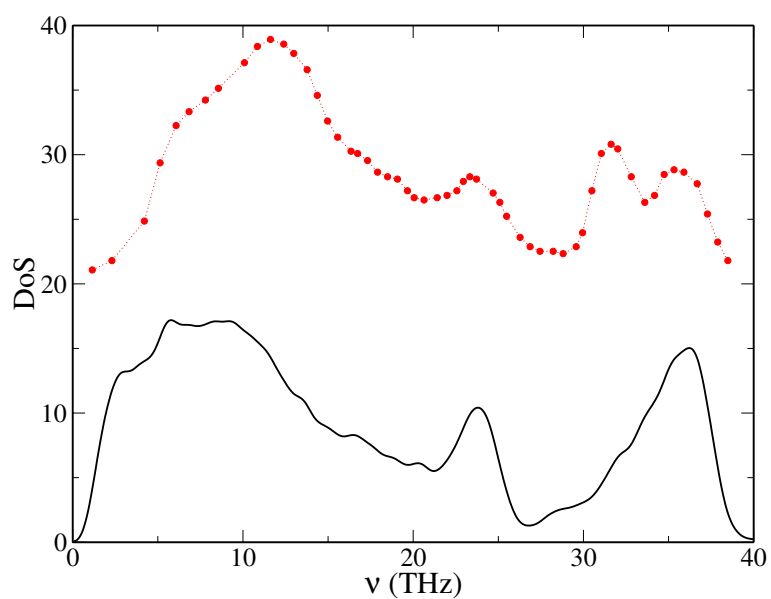


Figure 4.4.10: Vibrational density of states (DoS) of amorphous silica (computed with a cell with 4116 atoms) obtained from the velocity-velocity autocorrelation function (black line), compared with experimental results (red line) from D. L. Price and J. M. Carpenter, *Journal of Non-Crystalline Solids*, 92 (1987) 153-174.

is size-independent. This is consistent with our previous finding for *a*-Si, which shows that the propagating modes with long mean free path at low frequencies are responsible for the convergence behavior of κ . In addition, the κ of *a*-SiO₂ computed using NEMD simulations with very small cells (L=2.1nm) by Jund and Jullien [117] is in agreement with experiments. This may also indicate that there are no or very few propagating modes in *a*-SiO₂.

To understand these non-propagating modes in *a*-SiO₂, and to estimate how much they contribute to the heat transport, we calculated the κ of *a*-SiO₂ using the harmonic diffusive model proposed by Allen and Feldman [97] (Eq. 2.3.45). Fig. 4.4.11 shows that the computed κ very much depends on the chosen value of the Lorentzian width. This result was also reported by Shenogin et al. [128]. By using a width exceeding the mean energy-level spacing in Ref. 128, they obtained a value of κ which is underestimated by a factor of about 2 with respect to experiments. Based on their studies on several inorganic and polymeric glasses, these authors concluded that the AF model works well for amorphous materials with one atomic species and identical interaction potentials between all atoms, but not for complex compositions like the one of amorphous silica or of organic polymer glass.

Our previous study of amorphous silicon showed that the AF model is very sensitive to whether the system is fully disordered or not. To verify if the generated *a*-SiO₂ is fully disordered, we computed the phase quotient (Q_i) of phonon modes, which can be used to distinguish between ordered and disordered systems: [129]:

$$Q_i = \frac{\sum_{n,m} \sum_{\alpha} u_{n\alpha,i} u_{m\alpha,i}}{\sum_{n,m} |\sum_{\alpha} u_{n\alpha,i} u_{m\alpha,i}|} \quad (4.4.1)$$

where, $u_{n\alpha,i}$ is the component of the polarization vector (e_i), the displacement of atom n from its equilibrium position at α direction. n and m are nearest neighbors. The

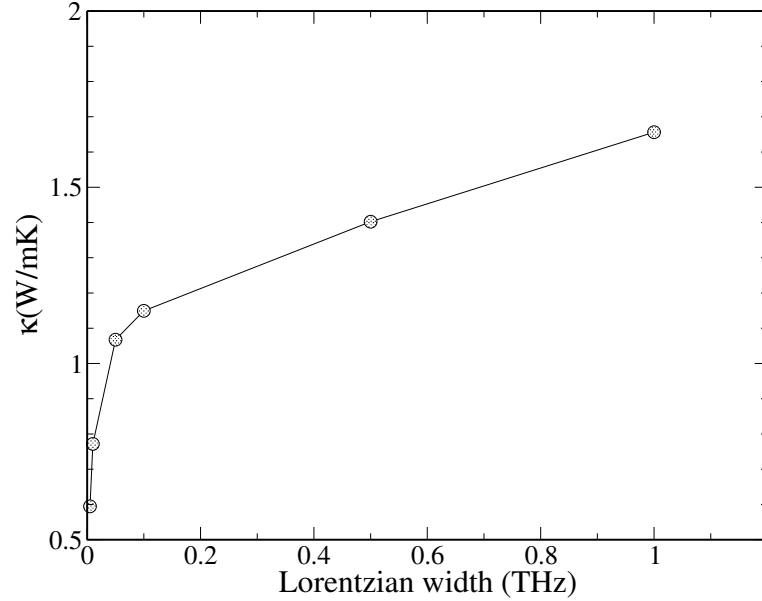


Figure 4.4.11: Thermal conductivity calculated using the Allen-Feldman model, as a function of the Lorentzian width used in the calculation of the diffusivity, for an amorphous silica sample with 4116 atoms.

calculated phase quotient displayed in Fig. 4.4.12 shows that the generated a -SiO₂ is fully disordered similar to the fully disordered amorphous silicon sample generated by a melting-annealing procedure in Chapter 4.2. Therefore, we conclude that the width-dependent found in the calculation of the diffusivities is not caused by the type of disorder in the systems, but due to the existing different species in the a -SiO₂ samples.

Previous numerical studies showed that 3% of modes at high frequencies are localized in amorphous silicon [129]. To study whether localized vibrational states are present in amorphous silica, two quantities were calculated: the inverse participation ratio and the spatial decay of vibrational states. The inverse participation is defined

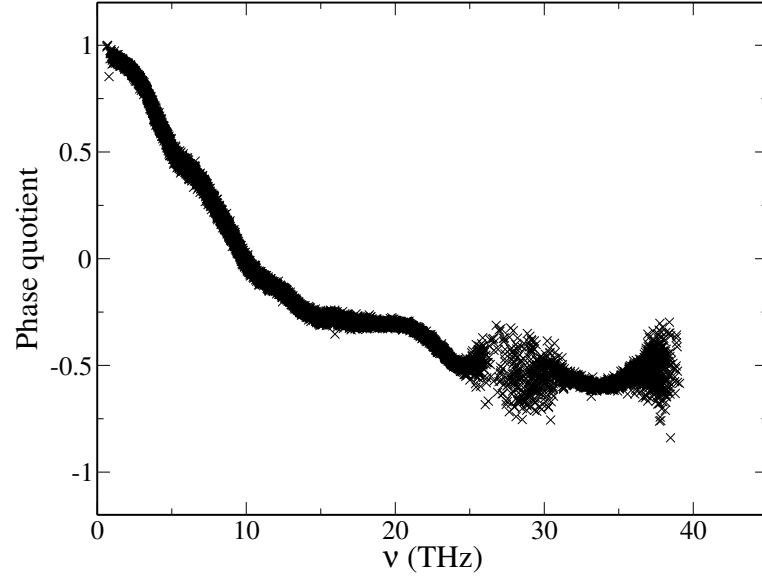


Figure 4.4.12: Phase quotient as a function of frequency for an amorphous silica sample with 4116 atoms.

as:

$$p_i^{-1} = N \sum_n \left(\sum_\alpha u_{n\alpha,i}^* u_{n\alpha,i} \right) \quad (4.4.2)$$

where, $u_{n\alpha,i}$ is the component of the polarization vector (e_i), the displacement of atom n from its equilibrium position at α direction. If the vibrations were localized on a single atom, p_i^{-1} will be 1, whereas if the vibration were equally distributed on all atoms, the result will be $1/N$.

The spatial decay of vibrational states is defined as :

$$|\epsilon_i(\mathbf{R})| \propto \exp(-|\mathbf{R} - \mathbf{R}_0|/\xi_i) \quad (4.4.3)$$

Fig. 4.4.13 shows the spatial decay of vibrational eigenvectors for selected modes. For each mode i the atom with the largest displacement was located, and taken as

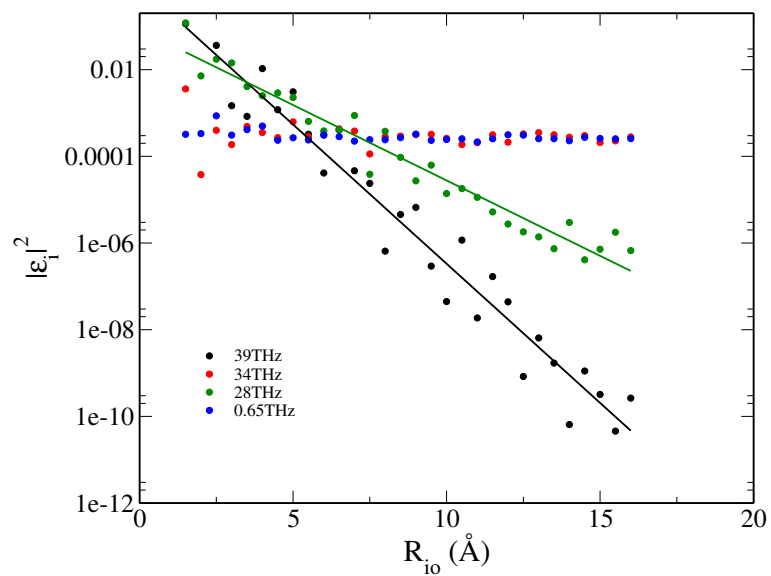


Figure 4.4.13: Spatial decay of vibrational eigenvectors of an amorphous silica sample with 4116 atoms as a function of frequencies. Solid lines are guides to the eye.

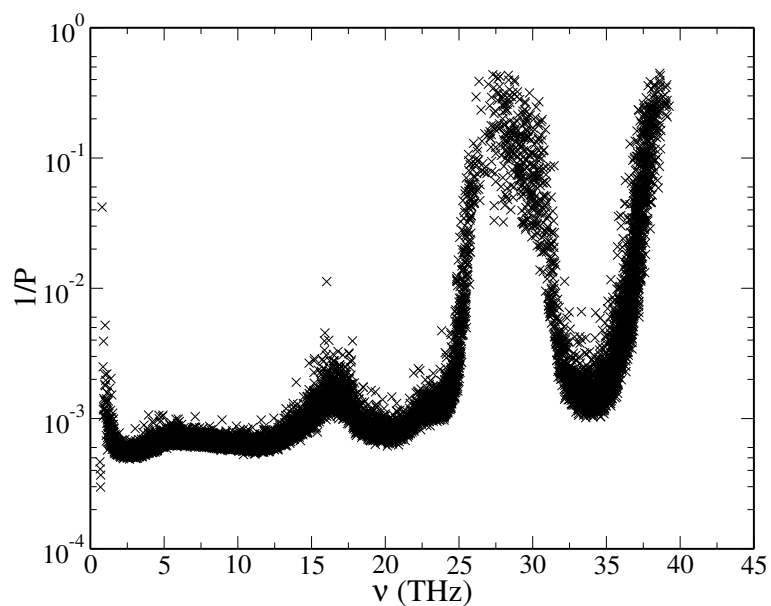


Figure 4.4.14: Inverse Participation ($1/P$) as a function of frequency for an amorphous silica sample with 4116 atoms.

the origin (R_0). The averaged displacement (ϵ) over spherical shells with width= 0.2\AA around the origin (R_0) was then calculated as a function of distance (R) to the origin. We did not find any localized states at low frequencies in $a\text{-SiO}_2$. The decay of high frequency modes is similar to that of high frequency localized modes in amorphous silicon [129]. In Fig. 4.4.14, the calculated inverse participation ratio shows that localized states are present in two frequency ranges: one for $25\text{ THz} < \omega < 30\text{ THz}$, the other one for $\omega > 35\text{ THz}$. This result is consistent with our finding about the spatial decay of vibrational eigenvectors for the modes with $\omega = 28\text{ THz}$ and $\omega = 39\text{ THz}$. However, a sharp boundary between these localized modes and extended modes can not be easily defined.

Chapter 5

Heat transport in nanostructured bulk materials

5.1 Background and objectives

As mentioned in the introduction (Chapter 1), Thermoelectric materials which can both generate electricity from waste heat and use electricity for solid-state Peltier cooling [130, 131] are to date inefficient, compared to conventional generators and refrigerators. To have an efficiency superior to that of conventional generators and refrigerators, thermoelectric materials should have $ZT \geq 3$. One way to obtain systems with improved efficiency is to engineer nanostructured semiconductors, so as to reduce the thermal conductivity of the crystalline material, while preserving its electronic properties. Such a strategy has been recently applied to Si, an earth abundant, cheap and non toxic material, and promising results have been obtained for Si nanowires and thin films of nanoporous Si (np-Si), i.e. nanomeshes. Si wires have been fabricated [20, 132, 107, 133] that have κ up to 100 times smaller than that of

c-Si (κ_{c-Si}), and $ZT \simeq 0.6$. The thermal conductivity of nanomeshes has been made even smaller than that of nanowires for specific choices of the pore size and spacing, without degrading the electronic properties of c-Si. Both the thermal conductivity reduction reported in np-Si and the preservation of bulk Si electronic properties have been predicted by atomistic and electronic structure calculations reported in the literature few years ago, though the surface to volume ratio studied theoretically was higher than that obtained experimentally [134, 135], and the microscopic origin of the reduction of κ has not yet been addressed.

In addition to nanostructuring, mass disorder may help to decrease the thermal conductivity of Si based materials. For example, Silicon Germanium (SiGe) alloys have long been used to convert heat into electricity, e.g. in thermocouples employed in several of NASA space missions [109, 110]. Although very reliable and long-lasting, such thermocouples are inefficient, especially at room temperature. Recent experimental and theoretical studies have shown that a promising way of improving ZT of SiGe alloys is through reduction of κ at the nanoscale, and encouraging results have been reported for nanograined [136, 131] and nanoporous SiGe [137], SiGe superlattices [138], and SiGe thin wires [139]. However, as in the case of np-Si the microscopic mechanisms leading to such reductions are not fully understood; in addition the dependence of κ on morphology and temperature, and the interplay between structural disorder, mass disorder and nanostructuring are still open questions. In the following we report our investigations of np-Si and np-SiGe and the understanding we gained, at the microscopic level, of the heat transport mechanisms in these systems.

5.2 Thermal transport in nanoporous silicon

We carried out molecular and lattice dynamics calculations of the thermal conductivity of nanoporous silicon (np-Si) and established the role of and the interplay between several effects contributing to thermal transport, including film thickness, porosity, surface-to-volume ratio, and the presence of amorphous surface layers. np-Si samples were considered with porosity similar to that of recently engineered nanomeshes [21], and the results show that the presence of nano-meter sized holes may lead to values of κ 10 to 20 times smaller than in c-Si, depending on the degree of order at their surfaces. Additional reduction of about one order magnitude is obtained in thin (20 nm) nanoporous films, in agreement with experiment. The results also show that by combining mesoscopic (presence of pores) and atomic scale disorder at surfaces, one may engineer a nanostructured Si material with much reduced thermal conductivity in both the direction perpendicular and parallel to the pores.

The thermal conductivity of np-Si (κ_{np-Si}) was computed by using EMD and the empirical potential proposed by Tersoff [30] (see Eq. 2.2.22) in the DLPOLY code. The calculations were carried out for systems with both ordered and disordered surfaces, and for bulk and thin film samples.

The geometry of np-Si is described by porosity $\phi = \pi d_p^2 / (2d_p + 2d_s)^2$, and surface-to-volume ratio $\rho = \pi d_p / (d_p + d_s)^2$, where d_s and d_p are pore spacing and pore diameter. Fig. 5.2.1 gives a pictorial representation of the type of systems studied here. Tab. 5.2.1 shows $\frac{\kappa_{c-Si}}{\kappa_{np-Si}}$ for a np-Si sample with porosity of 0.07 (and pores in the 100 direction), as a function of surface-to-volume ratio. The values of ϕ for the nanomeshes studied experimentally [21] are 0.08 and 0.16. At fixed porosity, κ appears to depend weakly on ρ in the range 0.16-0.07; however, it does decrease for larger values of ρ and it is known from our previous study [134] that in the range $0.3 < \rho < 0.8$ the

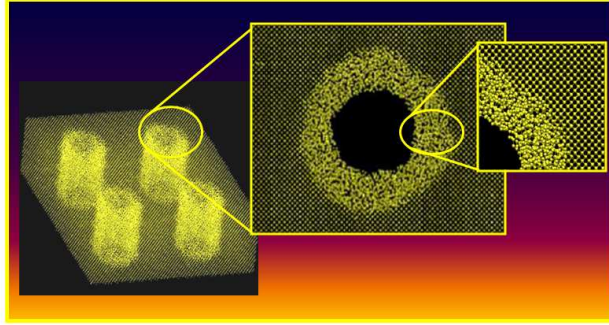


Figure 5.2.1: Representative microscopic picture of nanoporous materials investigated in the present work. The samples with both ordered and disordered surfaces were studied, as indicated by the insets.

Table 5.2.1: Ratio between thermal conductivity (W/mK) computed for bulk Si (κ_{c-Si}) and for nanoporous Si (κ_{np-Si}) with ordered surfaces (OS) and disordered surfaces (DS), as a function of the surface-to-volume ratio (ρ) for a sample with porosity $\phi=0.07$. The porosity was chosen to be similar to that of recently fabricated nanomeshes [21]. For each sample, we also give the distance (nm) between pores (d_s) and the pore diameter (d_p).

ρ 1/nm	$\kappa_{c-Si}/\kappa_{np-Si}$ (OS)	$\kappa_{bulk}/\kappa_{np}$ (DS)	d_s	d_p
0.3	28	68	2.3	1
0.16	12	34	4.4	2.3
0.07	7	19	10	4.4
0.07 mis.	10		10	4.4

ratio $\frac{\kappa_{c-Si}}{\kappa_{np-Si}}$ becomes roughly constant and close to two orders of magnitude. Even for relatively small ρ (0.07), κ is 7 times smaller than that in the bulk.

The results show that if atomistic disorder is present at the pore surfaces, the thermal conductivity of np-Si further decreases to a value about 20 times smaller than κ_{c-Si} . In our simulations, disorder at the pore surfaces was obtained by heating the ordered sample up to 2800 K and then cooling it down to 300 K, while allowing a small region close to the surface to amorphize. The values of κ for samples with disordered surfaces correspond to 18% disordered sites in the sample, where disorder was defined by an order parameter usually adopted for tetrahedrally bonded materials. [140, 141]. Increasing disorder from 18 to 26 % (corresponding to 6 and 8 disordered atomic layers, respectively) lowers κ by approximately 20 to 30 %. It is interesting to note that in the presence of disordered surfaces, the thermal conductivity is considerably lowered also in the direction parallel to the pores. Samples with disordered surfaces exhibit thermal conductivity in the direction parallel to the pores (κ_{\parallel}) at least 10 times smaller than the corresponding ones with ordered surfaces.

Since experimental samples are likely to exhibit a certain degree of misalignment between pores, for the system with the lowest value of ρ , a simulation with misaligned pores was carried out. Four pores per unit cell were considered, yielding a total of 86576 atoms. Three of the pores are aligned and one is misaligned by 2nm in both the x and y directions. Having slightly misaligned pores further decreases κ by a factor of 3 (see Tab. 5.2.1).

To compare with experiments performed on thin films [21], the reduction of κ in a 20 nm crystalline homogeneous thin film (no pores) was first evaluated with respect to that of the bulk. Two cases were considered: one film with smooth surfaces and one with 1nm rough surfaces, to mimic experimental samples, which are prepared as Si

on oxide and are expected to have a thin oxide layer at their surfaces. The reduction factors of 3 and 7 were found, respectively; this result is consistent with experiment, where the ratio $\frac{\kappa_{c-Si}}{\kappa_{thin-film}} \simeq 7.5$. Then a 20 nm thin film with the same porosity as the bulk samples discussed above ($\phi = 0.07$) was simulated, and the surface-to-volume ratio of this thin film np-Si is close to experiment ($\rho = 0.07$). In this case, only ordered pore surfaces and smooth thin film surfaces were considered, and a reduction of a factor of 3 was found with respect to a crystalline thin film sample (no pores) of the same exact thickness. The reduction found experimentally is larger (close to 9); however, including the effect of pore misalignment and disordered pore surfaces brings the results in this work very close to the experimental ones [21].

In order to characterize, at the microscopic scale, the properties of the heat carriers of np-Si, and to understand how they differ from those of c-Si, a series of lattice dynamics calculations were carried out (see Chapter 2.3). A specific sample ($\phi = 0.07$ and $\rho = 0.3$) was focused. In np-Si with ordered surfaces np-Si(OS), due to the presence of pores, the group velocities (v_g) of modes below 3-5 THz in the direction perpendicular to the pores are greatly decreased with respect to c-Si (most of them by approximately one order of magnitude), particularly for acoustic modes below 3-5 THz (see Fig. 5.2.2). This change is largely responsible for the decrease of thermal conductivity in the direction perpendicular to the pores (κ_{\perp}) found in the MD simulations. In contrast, a very moderate decrease of v_g was observed in the direction parallel to the pores, consistent with the small decrease of κ_{\parallel} (of the order of 10%) with respect to c-Si.

An analysis of the polarization of vibrational modes show that in the np-Si sample a considerable amount of vibrations is no longer propagating but rather becomes diffusive, as in *a*-Si (see Fig. 5.2.3), and unlike the case of c-Si, where all vibrational

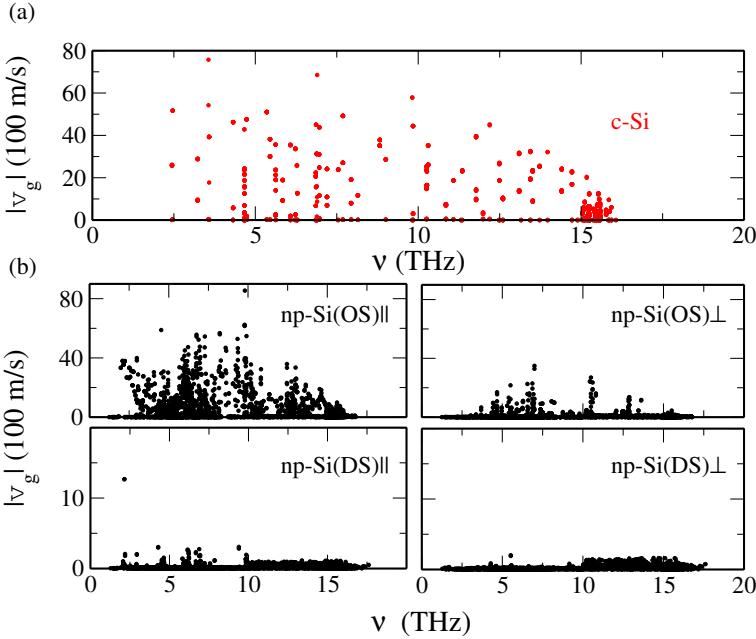


Figure 5.2.2: (a) Group velocity as a function of frequency for np-Si with ordered [np-Si(OS)] and disordered [np-Si(DS)] surfaces (the two samples have the same porosity: $\phi = 0.07$). The left and right panels show the group velocity in the direction parallel to the pores and in the direction perpendicular to the pores, respectively. (b) Group velocity as a function of frequency for np-Si with ordered [np-Si(OS)] and disordered [np-Si(DS)] surfaces (the two samples have the same porosity: $\phi = 0.07$). The left and right panels show the group velocity in the direction parallel to the pores and in the direction perpendicular to the pores, respectively.

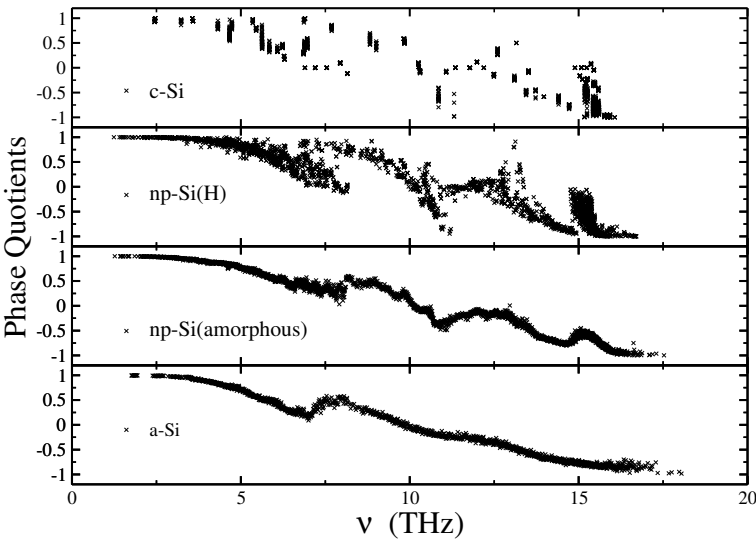


Figure 5.2.3: Calculated phase quotient as a function of frequency for c-Si, np-Si with hydrogen terminated pores, np-Si with *a*-Si terminated pores, and *a*-Si, respectively.

modes are propagating phonons. Diffusive modes exhibit a weak localization of the Ioffe-Regel type, [142] rather than an Anderson-localization type behavior. Indeed, an analysis of the spatial extent of their eigenvectors (not shown) shows a polynomial, rather than an exponential decay as a function of distance, similar to what is found in *a*-Si. Diffusive modes are heat carriers, although much less effective than phonons. The relative contributions of diffusive and propagating modes to the thermal conductivity of np-Si can be found by describing phonons with the Boltzmann transport equation in the single mode relaxation time approximation, and by describing diffusive modes using the theory devised for such modes in *a*-Si by Allen and Feldman. The results show that 25% of the thermal conductivity of the np-Si sample originates from propagating modes with reduced group velocities with respect to *c*-Si, and the rest comes from diffusive modes. The sum of the two contributions yields the value computed independently in our MD simulations.

Amorphization of the pore surfaces further decreases the group velocities of all modes of np-Si, and yields an increased density of diffusive modes. Group velocities decrease both in the direction parallel and perpendicular to the pores. While group velocities of vibrational modes are greatly affected by both mesoscopic (i.e. presence of pores) and atomistic disorder, lifetimes (τ , not shown) exhibit a less dramatic variation. The existence of nano-scale pores only leads to a moderate decrease of τ (by a factor of 2 to 3, depending on porosity), with respect to the crystal. It is the presence of amorphized surfaces that considerably lowers the lifetimes, especially the ones of low frequency modes. In np-Si (DS), the calculated mean free path ($\lambda = v\tau$) (see Fig. 5.2.4) may attain values of the order of the distance between pores. The mean free paths of low frequency modes of np-Si(OS) are instead larger, on average, with values up to 50 nm in the direction perpendicular to the pores and of the order

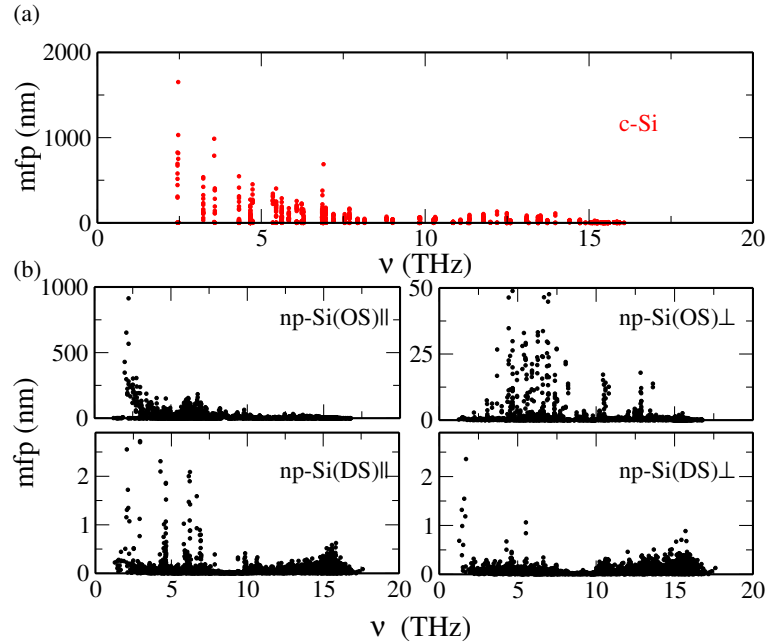


Figure 5.2.4: (a) Mean free path as a function of frequency for the same np-Si samples shown in figure 5.2.2. The left and right panels show the mean free path in the direction parallel to the pores and in the direction perpendicular to the pores, respectively. (b) Mean free path as a function of frequency for c-Si (upper panel) and *a*-Si (lower panel).

of a micron in the direction parallel to the pores.

5.3 Thermal transport in nanoporous silicon germanium

We now turn to the discussion of our equilibrium molecular dynamics (EMD) simulations of the thermal conductivity of nanoporous SiGe (np-SiGe) at stoichiometric composition. The results obtained in this work show that in the direction perpendicular to the pores, the thermal conductivity (κ_{pp}) of np-SiGe may be reduced by a factor of approximately 3 to 16, with respect to that of crystalline bulk

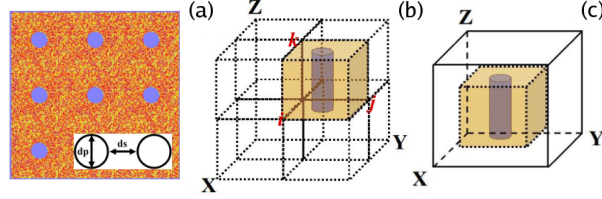


Figure 5.3.1: Schematic representation of a nanoporous silicon germanium sample investigated in the molecular dynamics (MD) simulations. (a) Top view of the sample along the z direction (parallel to the pores). The inset indicates the pore diameter (d_p) and the distance between pores (d_s). (b) A representative supercell used in our equilibrium MD simulations, where the shaded region indicates a cell (1064 atoms) that was repeated i th, j th, and k th times in the X , Y and Z directions, respectively, when performing convergence tests. (c) A representative supercell used in the equilibrium MD simulations, where the shaded region indicates a cell (1064 atoms) whose size along the X , Y , Z directions was systematically increased in simulations aimed at testing the influence of pore distance with a fixed diameter of pore.

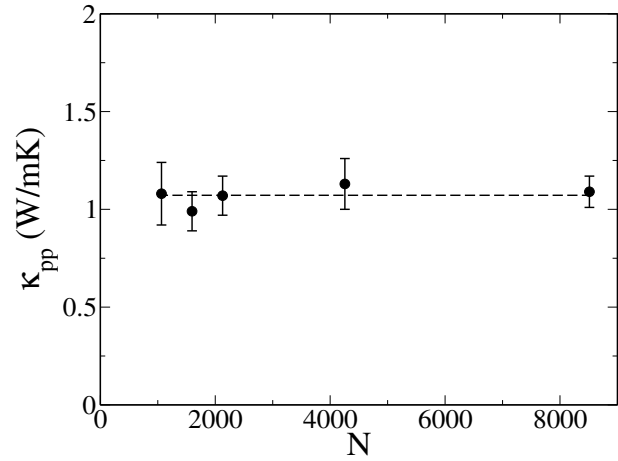
SiGe samples, depending on the chosen porosity (ϕ) and surface-to-volume ratio (ρ). For values of ϕ and ρ similar to those recently obtained for Si nanomeshes [21, 108], κ_{pp} of np-SiGe is reduced by about three times with respect to that of the bulk. The results also show that, whereas reducing the thickness of crystalline SiGe thin films decreases their thermal conductivity (e.g. by a factor of $\simeq 1.5$ at $\simeq 20$ nm), film thickness weakly affects κ_{pp} of np-SiGe. Likewise, the presence of atomistic disorder at pore surfaces has little effect on the value of κ_{pp} , contrary to what was found for the case of np-Si [108]. Finally the results of np-SiGe samples with pores of ~ 1 nm diameter as a function of T show that their thermal conductivity is almost constant between 300 and 1100 K.

We carried out the EMD simulations on np-SiGe in the DLPOLY code with the Tersoff empirical potential [30] and periodic boundary conditions. Several np-SiGe samples were considered at stoichiometric composition, as a function of porosity (ϕ) and surface-to-volume ratio (ρ), defined as $\phi = \pi d_p^2 / (2d_p + 2d_s)^2$, and $\rho = \pi d_p / (d_p +$

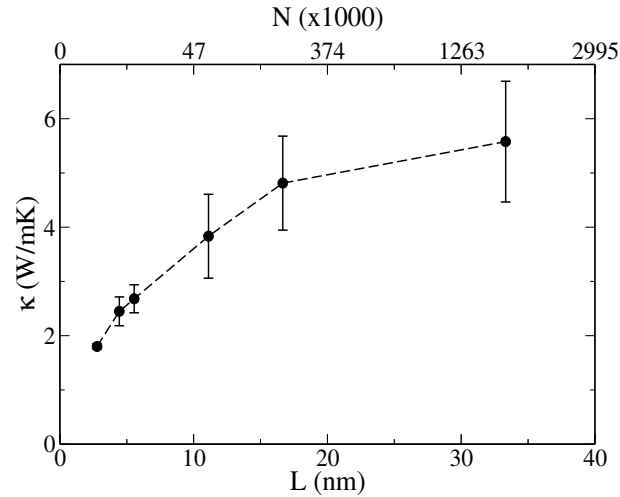
$d_s)^2$, respectively, where d_s and d_p are the pore spacing and pore diameter (see Fig. 5.3.1). The thermal conductivity in the direction perpendicular to the pores (κ_{pp}) was calculated using the Green-Kubo (GK) formula (see Eq. 2.2.22). The heat current was computed based on the Eq. 2.2.27 in DLPOLY.

The convergence of the thermal conductivity with respect to the truncation time (t_{tr}) was tested for a specific sample (with porosity 0.07 and surface-to-volume ratio 0.27 nm^{-1}) composed of 1064 atoms (see Fig. 5.3.3). The results show that $t_{tr} = 5$ ps yields well converged values of κ_{pp} . Extensive convergence tests as a function of system size were also carried out. Five simulations were performed for each size, and each simulation has randomly chosen mass disorder distributions. Within statistical error bars the same value of κ_{pp} for all sizes considered here was found (see Fig. 5.3.2 (a)). This behavior is in stark contrast with that obtained for bulk SiGe, for which millions of atoms are necessary in equilibrium MD (EMD) simulations to properly converge the value of the thermal conductivity, as shown in Fig. 5.3.2 (b). The value of κ for bulk SiGe obtained by EMD is $\sim 6.0 \text{ W/mK}$ (see Chapter 4). The reason for the difference in convergence between bulk SiGe and np-SiGe stems from the type of carriers contributing to the thermal conductivity and from their mean free path. Anharmonic lattice dynamics calculations [112], as well as the MD simulations in this work, show that in bulk SiGe low frequency carriers, with frequency smaller than $\sim 3 \text{ THz}$, have mean free paths of the order of a micron and these carriers yield a substantial contribution to κ . The results show below that in the case of np-SiGe, the presence of pores reduces the mean free paths of the low frequency carriers to nanometers, in the direction perpendicular to the pores.

Tab. 5.3.1 shows the computed results of κ_{pp} for np-SiGe as a function of porosity and surface-to-volume ratio, comparing with those obtained for np-Si in Fig. 5.3.4.



(a)



(b)

Figure 5.3.2: (a) Thermal conductivity of nanoporous SiGe at stoichiometric composition as a function of the number of atoms in the MD cell (N), at room temperature. The dimensions of the MD cells (L_x, L_y, L_z) in nm , the number of pores (n) and the pore radius (r) in nm for the samples with N atoms used in our simulations are the following: $N=1064$, (3.4, 3.4, 2.3), $n=1$, $r=0.5$; $N=1596$, (3.4, 3.4, 3.4), $n=1$, $r=0.5$; $N=2128$, (3.4, 3.4, 4.5), $n=1$, $r=0.5$; $N=4256$, (6.8, 6.8, 2.3), $n=4$, $r=0.5$; $N=8512$, (6.8, 6.8, 4.5), $n=4$, $r=0.5$. All samples have the same porosity ($\phi=0.07$) and the same surface-to-volume ratio ($\rho=0.27 \text{ nm}^{-1}$), (See also Fig. 1). (b) Thermal conductivity of bulk $\text{Si}_{0.5}\text{Ge}_{0.5}$ as a function of the length L of the molecular dynamics cell used in our simulations; the number of atoms (N) in the cell is given in the upper axis. The largest cell used for bulk SiGe contains 1.728 million atoms. The simulations were carried out at room temperature.

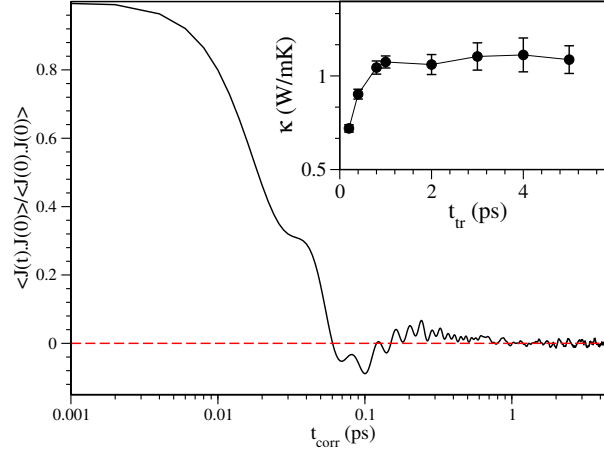


Figure 5.3.3: The normalized heat current autocorrelation function of np-SiGe at stoichiometric composition as a function of correlation time (t_{corr}) at 300K. The porosity ϕ of the sample is 0.07 and the surface-to-volume ratio (ρ) is 0.27 1/nm. The inset shows the calculated thermal conductivity as a function of the truncation time (t_{tr})

Table 5.3.1: Thermal conductivity computed for nanoporous SiGe samples (κ_{pp}) in the plane perpendicular to the pores, as a function of porosity (ϕ) and surface-to-volume ratio (ρ). The surface-to-volume ratio of 0.07 is the same as previously studied in np-Si [108]. For each sample, the distance between pores (d_s), and the pore diameter (d_p) are also given. All systems represent bulk samples except the one for which the film thickness (20 nm) is explicitly given.

ϕ	ρ nm ⁻¹	κ_{pp} W/mK	d_s nm	d_p nm
0.27	1.09	0.36±0.03	0.70	1.00
0.15	0.62	0.56±0.04	1.26	1.00
0.10	0.39	0.74±0.05	1.83	1.00
0.07	0.27	1.08±0.16	2.40	1.00
0.07(rough surfaces)	0.27	0.98±0.15	2.40	1.00
0.07	0.07	1.78±0.36	10.00	4.40
0.07(20nm film)	0.07	1.89±0.46	10.00	4.40

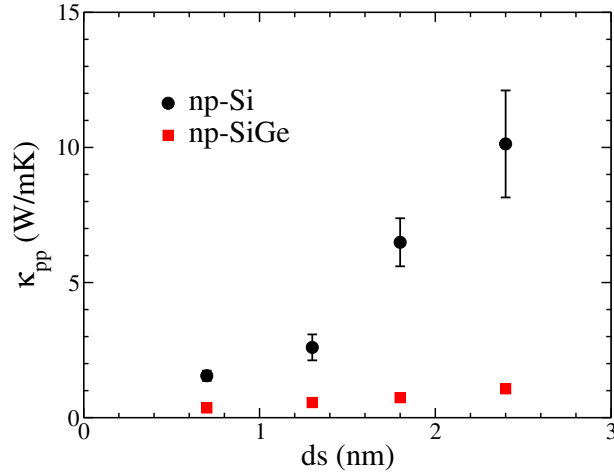


Figure 5.3.4: Thermal conductivity of nanoporous Si (np-Si) and nanoporous SiGe (np-SiGe) in the direction perpendicular to the pores, as a function of pore distance (ds). The pore diameter is constant and equal to 1 nm.

For fixed pore diameter, the variation of κ_{pp} as a function of pore spacing is much weaker than in the case of np-Si [108], consistent with results obtained for much larger pores ($d_p = 1 \sim 10$ micrometer) by Mingo et al.[137], using mesoscopic Monte Carlo simulations of phonon transport. In addition, all values of κ_{pp} obtained for np-SiGe are smaller than the corresponding ones computed for np-Si. The ratio ($\kappa_{bulk-SiGe}/\kappa_{pp}$) varies between 3 and 16. In particular, for porosities similar to those investigated in Si nanomeshes [21, 108], the thermal conductivity is reduced by a factor of 3 with respect to the bulk. These results indicate that one may significantly reduce the thermal conductivity of bulk SiGe by nanostructuring, and that morphological constraints on pore size and spacing are less stringent than in the case of pure Si.

This work also investigated the effect on thermal transport of film thickness and of atomistic disorder at the pore surfaces. In the MD simulations, disorder at pore surfaces was obtained by heating an ordered sample to 2800 K for 50ps and then

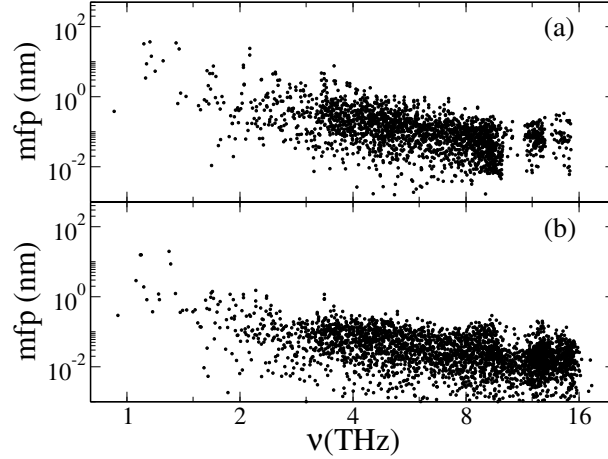


Figure 5.3.5: Mean free paths of vibrational modes as a function of frequency for a stoichiometric np-SiGe sample (1064 atoms) with $\phi=0.07$ and $\rho=0.27 \text{ nm}^{-1}$. (a) np-SiGe with ordered pore surfaces; (b) np-SiGe with disordered pore surfaces.

cooling it for 30 ns to 300 K while allowing a small region close to the surface to amorphize. The disordered surface of the samples shown in Tab. 5.3.1 contains 19% non-crystalline sites, where disorder was characterized with an order parameter typically adopted for tetrahedrally bonded materials [108, 141]. Contrary to the case of np-Si, the κ_{pp} of np-SiGe shows hardly any change in the presence of atomistic disorder at the pore surfaces (see Tab. 5.3.1).

In order to understand this result, the effective mean free paths of carriers as a function of frequency were computed for two samples that differ only by the amount of disorder at the pore surfaces: in one case samples have perfectly ordered surfaces, and in the other case samples have atomistic disorder over two layers close to surfaces. The effective mean free path of mode i is given by $\lambda_i = v_i^g \tau_i$, where effective group velocities v_i^g were obtained by diagonalizing the dynamical matrix of the system, and lifetimes τ_i were computed by MD simulations from the normalized autocorrelation function of the energy (E) of each vibrational mode i (Eq. 2.3.27). As shown by

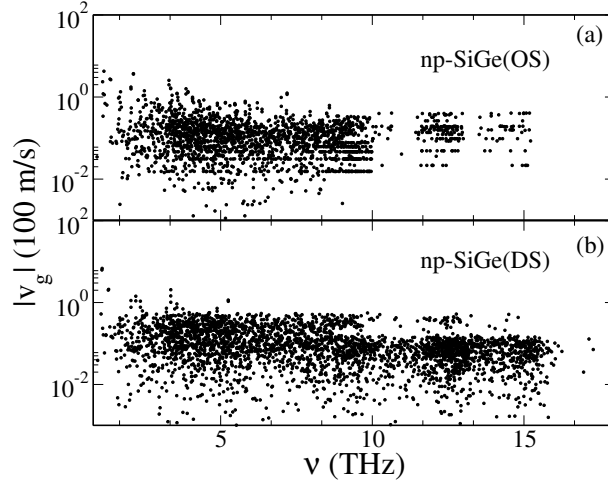


Figure 5.3.6: Calculated amplitudes of the group velocities of vibrational modes as a function of frequency for a stoichiometric np-SiGe sample with porosity $\phi=0.07$ and surface-to-volume ratio $\rho=0.27$ 1/nm at 300K. (a) with ordered pore surfaces, (b) with disordered pore surfaces.

comparing Fig. 5.3.5 (a) and (b), the presence of atomistic disorder leads to small changes in λ for most modes, with changes up to a factor of 8 to 10 only for a very small fraction of low frequency modes. An analysis of the group velocities (see Fig. 5.3.6) and lifetimes (see Fig. 5.3.7) show that at low frequency, v_i^g and τ_i are both reduced by the presence of atomistic disorder, in a fashion similar to what was found for np-Si [108]. However, the overall changes in v_i^g and τ_i are much smaller than in the case of np-Si, and so turns out to be the overall small change in κ_{pp} of np-SiGe. Therefore in the presence of mass disorder, atomistic surface disorder plays a negligible role in determining the value of the thermal conductivity in the direction perpendicular to the pores.

Likewise, reducing the film thickness of np-SiGe to 20nm appears little effect on its thermal conductivity. As shown in Tab. 5.3.1, for the same ρ and ϕ , the values of the conductivity of a bulk sample and of a thin film with thickness equal to 20 nm are

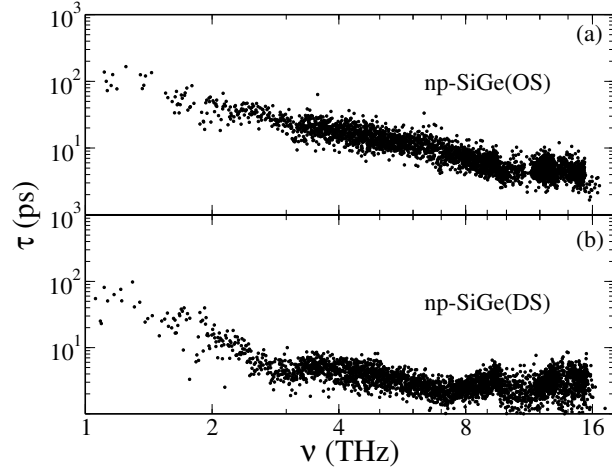
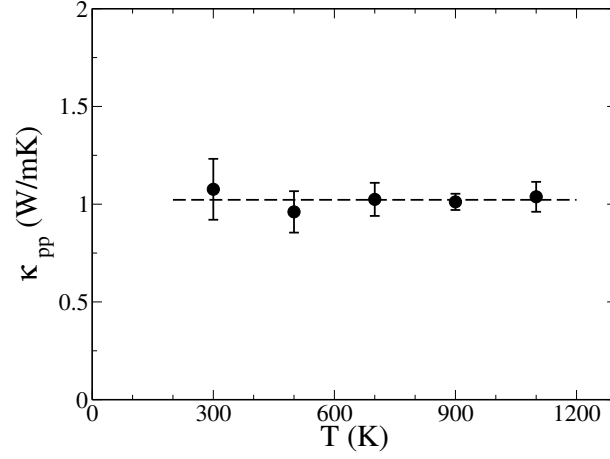


Figure 5.3.7: Calculated lifetimes of vibrational modes as a function of frequency for a stoichiometric np-SiGe sample with porosity $\phi=0.07$ and $\rho =0.27$ 1/nm at 300K. (a)with ordered pore surfaces, (b)with disordered pore surfaces.

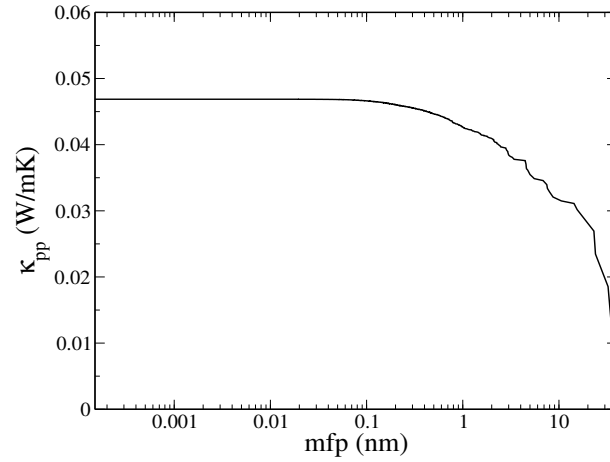
quite similar. This result may be explained again by overall small changes in v_i^g and τ_i upon thickness reduction, as in the case of disordered pore surfaces. However, this conclusion holds in the case of the nanoporous material where mean free paths are at most of the order of a nanometer, but it does not hold for bulk crystalline samples. Indeed, the simulations for crystalline SiGe thin films (with thickness equal to 20 nm) yield a decrease of $\sim 30\%$ of κ , with respect to the bulk sample: in this case thickness reduction does affect the mean free paths of low frequency modes, which may be of the order of several microns in the bulk. Similar results as a function of thickness were obtained in the case of amorphous Si [143]. An additional decrease of κ of crystalline SiGe may be obtained by allowing atomistic disorder at the thin film surfaces, as in the case of Si thin films [108].

This work also investigated the behavior of κ_{pp} as a function of temperature T . The results are reported in Fig. 5.3.8 (a) for a representative sample of np-SiGe with $\phi=0.07$ and $\rho=0.27$ nm⁻¹, where it is shown that κ_{pp} is essentially constant

between 300 and 1100 K. The sample was again chosen to be similar, in terms of porosity, to a np-Si sample previously studied [108]. The behavior of $\kappa_{pp}(T)$ shown in Fig. 5.3.8 (a) can be understood by analyzing the nature of the heat carriers in the direction perpendicular to the pores with anharmonic lattice dynamics calculations. As mentioned earlier, the low frequency modes of np-SiGe are “*greatly slowed down*” compared to the low frequency modes of bulk SiGe (whose mean free paths are of the order of microns). In addition, most of the computed group velocities (shown as Fig. 5.3.6) turned out to be between 10 and 100 m/sec, that is about 1/500 to 1/50 of the sound velocity in bulk SiGe. As a consequence, the mode *effective* mean free path, computed as $\lambda_i = v_i^g \tau_i$, is less than or equal to inter-atomic distances for frequencies $\nu > 4 \sim 5$ THz (see Fig. 5.3.5). Therefore, if one computes κ from the formula $\kappa_{BTE} = \sum_i c_i v_i^2 \tau_i$ (c_i is the specific heat per unit volume of vibrational mode i) – that is by using an approximate solution of the Boltzmann Transport Equation (BTE) that accounts only for propagating vibrations with mean free path substantially larger than the average interatomic distance–, one finds a value of the thermal conductivity much smaller than the one obtained in MD simulations (see Fig. 5.3.8 (b)). The results show that κ_{BTE} amounts to only 5% of the total value of κ_{pp} computed by EMD. This indicates that the largest contribution to κ_{pp} comes from modes with mean free path of the order of Angstrom, which are not accounted for by the approximate formula of κ_{BTE} . The behavior of $\kappa_{pp}(T)$ is dominated by the T dependence of modes with short (\sim Angstrom) mean free paths, whose contribution to thermal transport hardly changes in a wide T range, as found in the case of Si nanowires with disordered surfaces [107].



(a)



(b)

Figure 5.3.8: (a) Thermal conductivity of stoichiometric np-SiGe in the direction perpendicular to the pores for samples with $\phi=0.07$ and $\rho=0.27 \text{ nm}^{-1}$, as a function of temperature. (b) Thermal conductivity at 300K computed from the formula $\sum_{mfp}^{\infty} c_i v_i \lambda_i$, as a function of the maximum mean free path (mfp), included in the summation: the index i denotes vibrational modes. By using this formula (that accounts only for propagating modes with mean free paths much larger than inter-atomic distances) one accounts only for 5% of the total value of κ_{pp} obtained in our MD.

Chapter 6

Conclusions

In this dissertation we have presented a detailed atomistic study of heat transport in silicon based crystalline, amorphous and nanostructured materials. We have focused on Si, SiGe alloys and SiO₂, and we have carried out a series of calculations using equilibrium molecular dynamics, non-equilibrium molecular dynamics, the Boltzmann transport equation (BTE) and the Allen-Feldman (AF) theory. In all cases inter-atomic interactions were described by empirical potentials of the Tersoff type [30].

We first analyzed the numerical and theoretical approximations underlying the MD techniques used to compute the heat current, and we compared results obtained using MD simulations and approximate solutions of the BTE for crystalline systems. Although these approaches had been previously used in the literature to study heat transport in Si and Ge, their limit of validity had not been thoroughly investigated. Contrary to earlier reports [56, 57], we found that MD cells with several hundred thousands of atoms are necessary to converge calculations of the thermal conductivity of crystalline Si, due to the long mean free paths of the low frequency modes. Similar results were found for SiGe alloys where simulations with millions of atoms were

carried out, to obtain values of the thermal conductivity close to convergence. We used anharmonic lattice dynamics calculations to interpret our MD results and to build approximate solutions of the BTE, and we showed that the MD and BTE approaches may give consistent results, if compared for same size systems.

Our lattice dynamic calculations allowed us to distinguish between propagating and quasi-stationary modes in amorphous and nanostructured materials and to study their relative contributions to heat transport. In particular, in the case of *a*-Si we have shown that both types of heat carriers are present and give substantial contributions to the thermal conductivity. Therefore, the widely used concept of majority heat carriers with a well-defined mean free path and a simple kinetic model cannot be applied to describe thermal transport in *a*-Si at 300 K. We also showed how the mean free path of long-wavelength modes may be substantially decreased either in thin *a*-Si films or by etching holes in the glass, and we have investigated the effect of order at the mesoscopic scale on the thermal conductivity of *a*-Si.

Etching holes in crystalline Si modifies the propagation of vibrations and leads to a decrease of its thermal conductivity. We have shown that the presence of pores has two main effects on heat carriers: (i) appearance of non-propagating, diffusive modes and (ii) reduction of the group velocity of propagating modes, or phonons. The relative proportions of diffusive and propagating modes and the extent to which the group velocity (and thus the mean free path) of low-frequency propagating modes is reduced depend on pore spacing and distance. We found that effect (i) is enhanced by the presence of disorder at the pore surfaces; effect (ii) is enhanced by decreasing film thickness. Overall, our findings are consistent with those obtained for two and threedimensional model porous system (e.g., Lennard-Jones Ar) and for nonporous thin films.

Another effect leading to a decrease of the thermal conductivity in semiconductors is the presence of mass disorder (e.g. the conductivity of stoichiometric SiGe alloys is 15-20 times smaller than that of Si). However mass disorder does not completely suppress the existence of propagating modes. Our MD simulations showed that a substantial contribution to the thermal conductivity of bulk SiGe arises from a small portion of low frequency modes with mean free path of several micrometers. Etching holes in bulk SiGe dramatically hampers the contribution of these low-frequency propagating modes to heat transport, by reducing both group velocities and lifetimes, and thus their mean free paths. Such reductions lead to a substantial decrease of the thermal conductivity. Additional morphological changes to the material, for example, atomistic disorder at the pore surfaces and thickness of the film, have a negligible effect on the thermal conductivity in the direction perpendicular to the pores. The thermal conductivity is also found to be basically independent of T in the range 300-1100 K for pores of dimensions of about 1 nm, indicating that thermal conduction is dominated by mass and boundary scattering. These results suggest that the reduction of the thermal conductivity of SiGe alloys by nanoscale modifications is subject to much less stringent fabrication constraints than in the case of pure crystalline Si. Our findings also show that np-SiGe may be a good thermoelectric material over a wide T range, unlike bulk SiGe that is currently limited to high-T applications.

Finally our study of crystalline and amorphous silica showed that in the amorphous system, contrary to Si, propagating modes are basically absent giving rise to a thermal conductivity which is almost temperature independent and also weakly sensitive to cell sizes in MD simulations. The results on silica will be used to build models of realistic nanostructured semiconducting materials, inclusive of oxidized surfaces.

List of Publications

1. Yuping He, Davide Donadio and Giulia Galli, “Morphology and Temperature Dependence of the Thermal Conductivity of Nanoporous SiGe”, *Nano Lett.*, 11, 3608-3611, 2011.
2. Yuping He, Davide Donadio and Giulia Galli, “Heat Transport in Amorphous Silicon: Interplay Between Morphology and Disorder”, *Appl. Phys. Lett.*, 98, 144101, 2011.
3. Yuping He, Davide Donadio, Joo-Hyoung Lee, Jeffrey C. Grossman and Giulia Galli, “Thermal Transport in Nanoporous Silicon: Interplay Between Disorder at the Mesoscopic and Atomic Scale”, *ACS Nano.*, 5, 1839, 2011.

References

- [1] T. J. Seebeck, *Magnetic Polarization of Metals and Minerals*. Abhandl. Deut. Akad. Wiss. Berlin, 1822-23. 265-373.
- [2] J. C. Peltier, "Nouvelle experiences sur la caloricit  des courans electrique," *Ann. Chem.*, vol. LVI, p. 371, 1834.
- [3] W. Thomson, "On a mechanical theory of thermo-electric currents," *Proc. Roy. Soc. Edinburgh*, pp. 91-98, 1851.
- [4] E. Altenkirch, "Uber den nutzeffekt der thermosaule," *Phys. Zeitschrift*, vol. 10, pp. 560-568, 1909.
- [5] E. Altenkirch, "Electrothermische kalteerzeugung und reversible electrische heizung," *Phys. Zeitschrift*, vol. 12, pp. 920-924, 1911.
- [6] F. R. and G. Wiedemann, "On the heat conductivity of metals," *Annalen der Physik*, vol. 165, pp. 497-531, 1853.
- [7] A. F. Ioffe, S. V. Airapetyants, A. V. Ioffe, N. V. Kolomoets, and L. S. Stilbans, "On increasing the efficiency of semiconducting thermocouples," *Dokl. Akad. Nauk SSSR*, vol. 106, p. 931, 1956.

- [8] C. R. Russell, *Radioisotopic Power Sources in Elements of Energy Conversion*. Pergamon Press, 1967.
- [9] R. R. Heikes and R. W. Ure, *Thermoelectricity: Science and Engineering*. Interscience, New York, 1961.
- [10] C. B. Vining, “An inconvenient truth about thermoelectrics,” *Nature Mater.*, vol. 8, p. 83, 2009.
- [11] A. Majumdar, “Thermoelectricity in semiconductor nanostructures,” *Science*, vol. 303, pp. 777–778, 2004.
- [12] L. D. Hicks and M. S. Dresselhaus, “Thermoelectric figure of merit of one-dimensional,” *Phys. Rev. B*, vol. 47, p. 16631, 1993.
- [13] G. Chen, “Thermal conductivity and ballistic-phonon transport in the cross-plane direction of superlattices,” *Phys. Rev. B*, vol. 57, p. 14958, 1998.
- [14] M. N. Touzelbaev, P. Zhou, R. Venkatasubramanian, and K. E. Goodson, “Thermal characterization of $\text{bi}_2\text{te}_3/\text{sb}_2\text{te}_3$ superlattices,” *J. Appl. Phys.*, vol. 90, pp. 763–767, 2001.
- [15] J. C. Caylor, K. Coonley, J. Stuart, T. Colpitts, and R. Venkatasubramanian, “Enhanced thermoelectric performance in pbte-based superlattice structures from reduction of lattice thermal conductivity,” *Appl. Phys. Lett.*, vol. 87, p. 23105, 2005.
- [16] H. B. et al., “High thermoelectric figure of merit z_t in pbte and bi_2te_3 -based superlattices by a reduction of the thermal conductivity,” *Physica E*, vol. 13, pp. 965–968, 2002.

- [17] G. A. Slack, in *CRC Handbook of Thermoelectrics*, ed. by D. M. Rowe. CRC Press, Boca Raton, FL, 1995. 407.
- [18] D. G. Cahill, S. K. Watson, and R. O. Pohl, “Lower limit to thermal conductivity of disordered crystals,” *Phys. Rev. B*, vol. 46, pp. 6131–6140, 1992.
- [19] W. S. Capinski, H. J. Maris, E. Bauser, I. Silier, M. Asen-Palmer, T. Ruf, M. Cardona, and E. Gmelin, “Thermal conductivity of isotopically enriched si,” *Appl. Phys. Lett*, vol. 71, p. 2109, 1997.
- [20] A. I. Hochbaum, R. Chen, R. D. Delgado, W. Liang, E. C. Garnett, M. Najarian, A. Majumdar, and P. Yang, “Enhanced thermoelectric performance of rough silicon nanowires,” *Nature*, vol. 451, pp. 163–167, 2008.
- [21] J.-K. Yu, S. Mitrovic, D. Tham, J. Varghese, and J. R. Heath, “Reduction of thermal conductivity in phononic nanomesh structures,” *Nature, Nanotechnol.*, vol. 5, pp. 718–721, 2010.
- [22] J. Tang, H. T. Wang, D. H. Lee, M. Fardy, Z. Huo, T. P. Russell, and P. Yang, “Holey silicon as an efficient thermoelectric material,” *Nano Letters*, vol. 10, no. 10, pp. 4279–4283, 2010.
- [23] J. Yang, *Thermal Conductivity: Theory, Properties and Applications*. [edited by] Terry Tritt. Kluwer Academic/Plenum Publisher, 2004. 1.
- [24] M. P. Allen and D. J. Tildesley, *Computer Simulation of Liquids*. Clarendon Press · OXFORD, 1987. 188.
- [25] R. W. Hockney, “The potential calculation and some applications,” *Methods Comput. Phys.*, vol. 9, pp. 136–211, 1970.

- [26] W. C. Swope, H. C. Andersen, P. H. Berens, and K. R. Wilson, "A computer simulation method for the calculation of equilibrium constants for the formation of physical clusters of molecules: application to small water clusters," *J. Chem. Phys.*, vol. 76, pp. 637–649, 1982.
- [27] F. H. Stillinger and T. A. Weber, "Computer simulation of local order in condensed phases of silicon," *Phys. Rev. B*, vol. 31, pp. 5262–5271, Apr 1985.
- [28] E. Pearson, T. Takai, T. Halicioglu, and W. A. Tiller, "Computer modeling of si and sic surfaces and surface processes relevant to crystal growth from the vapor," *Journal of Crystal Growth*, vol. 70, pp. 33 – 40, 1984.
- [29] M. Z. Bazant and E. Kaxiras, "Modeling covalent bonding in solids by inversion of cohesive energy curves," *Phys. Rev. Lett.*, vol. 77, p. 4370, 1996.
- [30] J. Tersoff, "Modeling solid-state chemistry: Interatomic potentials for multi-component systems," *Phys. Rev. B*, vol. 39, pp. 5566–5568, Mar 1989.
- [31] P. C. Kelires and J. Tersoff, "Equilibrium alloy properties by direct simulation: Oscillatory segregation at the si-ge(100) 2x1 surface," *Phys. Rev. Lett.*, vol. 63, no. 11, pp. 1164–1167, 1989.
- [32] K. L. Whiteaker, I. K. Robinson, J. E. Van Nostrand, and D. G. Cahill, "Compositional ordering in sige alloy thin films," *Phys. Rev. B*, vol. 57, no. 19, pp. 12410–12420, 1998.
- [33] J. Tersoff, "New empirical model for the structural properties of silicon," *Phys. Rev. Lett.*, vol. 56, no. 6, pp. 632–635, 1986.

- [34] S. Munetoh, T. Motooka, K. Moriguchi, and A. Shintani, “Interatomic potential for si-o systems using tersoff parameterization,” *Comput. Mater. Sci.*, vol. 39, pp. 334–339, 2006.
- [35] D. A. McQuarrie, *Statistical Mechanics*. University Science Books, Sausalito, CA, 2000. 641.
- [36] S. G. Volz and G. Chen, “Molecular dynamics simulation of thermal conductivity of silicon crystal,” *Phys. Rev. B*, vol. 61, pp. 2651–2656, 2000.
- [37] A. Einstein, *Investigations on the Theory of Brownian Movement*, ed. R. Fürth, translated by A.D. Cowper. Einstein, Collected Papers, 1926. vol. 2, 170.
- [38] D. A. Weitz, D. J. Pine, P. N. Pusey, and R. J. A. Tough, “Nondiffusive brownian motion studied by diffusing-wave spectroscopy,” *Phys. Rev. Lett.*, vol. 63, pp. 1747–1750, 1989.
- [39] F. Müller-Plathe, “A simple nonequilibrium molecular dynamics method for calculating the thermal conductivity,” *J. Chem. Phys.*, vol. 106, p. 6082, April 1997.
- [40] M. Born and R. Oppenheimer, “Zur quantentheorie der molekeln,” *Ann. Phys. (Leipzig)*, vol. 84 (20), p. 457, 1927.
- [41] M. T. Dove, *Introduction to Lattice Dynamics*. Cambridge University Press, 1993. 83.
- [42] A. J. H. McGaughey and M. Kaviany, “Quantitative validation of the boltzmann transport equation phonon thermal conductivity model under the single-mode relaxation time approximation,” *Phys. Rev. B*, vol. 69, p. 094303, 2004.

- [43] P. B. Allen and J. L. Feldman, “Thermal conductivity of disordered harmonic solids,” *Phys. Rev. B*, vol. 48, pp. 12581–12588, 1993.
- [44] G. P. Srivastava, *The Physics of Phonons*. Adam Hilger, Bristol, Philadelphia and New York., 1990. p94.
- [45] <http://www.cse.scitech.ac.uk/ccg/software/DLPOLY>.
- [46] <http://lammmps.sandia.gov>.
- [47] C. J. Glassbrenner and G. A. Slack, “Thermal conductivity of silicon and germanium from 3° k to the melting point,” *Phys. Rev.*, vol. 134, p. A1058, 1964.
- [48] J. Koenigsberger and J. Weiss, “Ueber die thermoelektrischen effekte (thermokräfte, thomsonwärme) und die wärmeleitung in einigen elementen und über die experimentelle prüfung der elektronentheorie,” *Ann. Phys., Lpz.*, vol. 35, p. 1, 1911.
- [49] A. D. Stuckes, “The thermal conductivity of germanium, silicon and indium arsenide from 40gc to 425c,” *Phil. Mag.*, vol. 5, p. 84, 1960.
- [50] R. D. Morris and J. G. Hust, “Thermal conductivity measurements of silicon from 30° to 425°c,” *Phys. Rev.*, vol. 124, p. 1426, 1961.
- [51] H. R. Shanks, P. D. Maycock, P. H. Sidles, and G. C. Danielson, “Thermal conductivity of silicon from 300 to 1400° k,” *Phys. Rev.*, vol. 130, p. 1743, 1963.
- [52] T. Ruf, R. W. Henn, M. Asen-Palmer, E. Gmelin, M. Cardona, H. J. Pohl, G. G. Devyatych, and P. G. Sennikov, “Thermal conductivity of isotopically enriched silicon,” *Solid State Commun.*, vol. 115, pp. 243–247, 2000.

- [53] R. K. Kremer, K. Graf, M. Cardona, G. G. Devyatykh, A. V. Gusev, A. M. Gibin, A. V. Inyushkin, A. N. Taldenkov, and H. J. Pohl, “Thermal conductivity of isotopically enriched ^{28}Si : revisited,” *Solid State Commun.*, vol. 131, pp. 499–503, 2004.
- [54] P. K. Schelling, S. R. Phillpot, and P. Keblinski, “Comparison of atomic-level simulation methods for computing thermal conductivity,” *Phys. Rev. B*, vol. 65, p. 144306, 2002.
- [55] D. P. Sellan, E. S. Landry, J. E. Turney, A. J. H. McGaughey, and C. H. Amon, “Size effects in molecular dynamics thermal conductivity predictions,” *Phys Rev B*, vol. 81, no. 21, p. 214305, 2010.
- [56] J. V. Goicochea, M. Madrid, and C. Amon, “Thermal properties for bulk silicon based on the determination of relaxation time using molecular dynamics,” *J. Heat Transfer*, vol. 132, pp. 012401–1, 2010.
- [57] L. Sun and J. Y. Murthy, “Domain size effects in molecular dynamics simulation of phonon transport in silicon,” *Appl. Phys. Lett.*, vol. 89, p. 171919, 2006.
- [58] D. A. Broido, A. Ward, and N. Mingo, “Lattice thermal conductivity of silicon from empirical interatomic potentials,” *Phys. Rev. B*, vol. 72, p. 014308, 2005.
- [59] A. F. Ioffe, “Heat transfer in semiconductors,” *Can. J. Phys.*, vol. 34, p. 1342, 1956.
- [60] B. Abeles, D. S. Beers, G. D. Cody, and J. P. Dismukes, “Thermal conductivity of ge-si alloy at high temperatures,” *Phys. Rev.*, vol. 125, pp. 44–46, 1962.
- [61] J. H. Lee and J. C. Grossman, “Thermoelectric properties of nanoporous ge,” *Appl. Phys. Lett.*, vol. 95, p. 013106, 2009.

- [62] V. V. Murashov and M. A. White, “Thermal properties of zeolites: effective thermal conductivity of dehydrated powdered zeolite 4a,” *Mater. Chem. Phys.*, vol. 75, p. 178, 2002.
- [63] Z. Y. Liu, G. Cacciola, G. Restuccia, and N. Giordano, “Fast simple and accurate measurement of zeolite thermal conductivity,” *Zeolites*, vol. 565, p. 10, 1990.
- [64] M. B. Jakubinek, B. Z. Zhan, and M. A. White, “Temperature-dependent thermal conductivity of powdered zeolite nax,” *Microporous Mesoporous Mater.*, vol. 108, p. 103, 2007.
- [65] A. M. Greestein, S. Graham, Y. C. Hudiono, and S. Nair, “Thermal properties and lattice dynamics of polycrystalline mfi zeolite films,” *Nanoscale Microscale Thermophys. Eng.*, vol. 10, p. 321, 2006.
- [66] P. Jund and R. Jullien, “Molecular-dynamics calculation of the thermal conductivity of vitreous silica,” *Phys. Rev. B*, vol. 59, 1999.
- [67] Y.-G. Yoon, R. Car, D. J. Srolovitz, and S. Scandolo, “Thermal conductivity of crystalline quartz from classical simulations,” *Phys. Rev. B*, vol. 70, p. 012302, 2004.
- [68] S. S. Mahajan, G. Subbarayan, and B. G. Sammakia, “Estimating thermal conductivity of amorphous silica nanoparticles and nanowires using molecular dynamics simulations,” *Phys. Rev. E*, vol. 76, p. 056701, 2007.
- [69] Z. Huang, Z. Tang, J. Yu, and S. Bai, “Thermal conductivity of amorphous and crystalline thin film by molecular dynamics simulation,” *Physica B*, vol. 404, pp. 1790–1793, 2009.

- [70] T. Coquil, J. Fang, and L. Pilon, “Molecular dynamics study of the thermal conductivity of amorphous nanoporous silica,” *Int. J. Heat Mass Tran.*, vol. 54, pp. 4540–4548, 2011.
- [71] A. J. H. McGaughey and M. Kaviany, “Thermal conductivity decomposition and analysis using molecular dynamics simulations part ii. complex silica structures,” *Int. J. Heat Mass Tran.*, vol. 47, pp. 1799–1816, 2003.
- [72] J. Che, T. Cagin, W. Deng, and W. A. G. III, “Thermal conductivity of diamond and related materials from molecular dynamics simulations,” *J. Chem. Phys.*, vol. 113, p. 6888, 2000.
- [73] E. S. Landry and A. J. H. McGaughey, “Effect of interfacial species mixing on phonon transport in semiconductor superlattices,” *Phys. Rev. B*, vol. 79, p. 075316, 2009.
- [74] S. chuang Wang, X. gang Liang, X. hua Xu, and T. Ohara, “Thermal conductivity of silicon nanowire by nonequilibrium molecular dyanmics simulations,” *J. Appl. Phys.*, vol. 105, p. 014316, 2009.
- [75] L. Shi, D. Yao, G. Zhang, and B. Li, “Size dependent thermoelectric properties of silicon nanowires,” *Appl. Phys. Lett.*, vol. 95, p. 063102, 2009.
- [76] P. G. Klemens, “The thermal conductivity of dielectric solids at low temperatures (theoretical),” *Proc. Roy. Soc. (London)*, vol. A208, p. 108, 1951.
- [77] S. Munetoh, T. Motooka, K. Moriguchi, and A. Shintani, “Interatomic potential for si-o systems using tersoff parameterization,” *Comput. Mater. Sci.*, vol. 39, pp. 334–339, 2007.

- [78] R. T. Downs and D. C. Palmer, "The pressure behavior of α cristobalite," *American Mineralogist*, vol. 79, pp. 9–14, 1994.
- [79] J. J. Pluth and J. V. Smith, "Crystal structure of low cristobalite at 10, 293 and 473 k: Variation of framework geometry with temperature," *J. Appl. Phys.*, vol. 57, p. 1045, 1985.
- [80] G. Domingues, J. B. Saulnier, and S. Volz, "Thermal relaxation times and heat conduction in β -cristobalite and α -quartz silica structures," *Superlattices and Microstructures*, vol. 227-237, p. 35, 2004.
- [81] D. Herzbach and K. Binder, "Comparison of model potentials for molecular-dynamics simulations of silica," *J. Chem. Phys.*, vol. 124711, p. 123, 2005.
- [82] B. W. H. van Beest, G. J. Kramer, and R. A. van Santen, "Force fields for silicas and aluminophosphates based on *ab initio* calculations," *Phys. Rev. Lett.*, vol. 64, pp. 1955–1958, 1990.
- [83] J. Etchepare, M. Merian, and P. Kaplan, "Vibrational normal modes of SiO_2 ii. cristobalite and tridymite," *J. Chem. Phys.*, vol. 68, p. 1531, 1978.
- [84] H. Wada and T. Kamijoh, "Thermal conductivity of amorphous silicon," *Japanese Journal of Applied Physics*, vol. 35, no. Part 2, No. 5B, pp. L648–L650, 1996.
- [85] B. L. Zink, R. Pietri, and F. Hellman, "Thermal conductivity and specific heat of thin-film amorphous silicon," *Phys. Rev. Lett.*, vol. 96, p. 055902, Feb 2006.
- [86] H. S. Yang *et al.*, "Anomalously high thermal conductivity of amorphous Si deposited by hot-wire chemical vapor deposition," *Phys. Rev. B*, vol. 81, p. 104203, Mar 2010.

- [87] D. G. Cahill, M. Katiyar, and J. R. Abelson, “Thermal conductivity of a-si:h thin films,” *Phys. Rev. B*, vol. 50, pp. 6077–6081, Sep 1994.
- [88] B. S. W. Kuo, J. C. M. Li, and A. W. Schmid, “Thermal conductivity and interface thermal resistance of si film on si substrate determined by photothermal displacement interferometry,” *Applied Physics A: Materials Science & Processing*, vol. 55, pp. 289–296, 1992.
- [89] S. Moon, M. Hatano, M. Lee, and C. P. Grigoropoulos, “Thermal conductivity of amorphous silicon thin films,” *Int. J. Heat and Mass Transfer*, vol. 45, pp. 2439–2447, 2002.
- [90] X. Liu *et al.*, “High thermal conductivity of a hydrogenated amorphous silicon film,” *Phys. Rev. Lett.*, vol. 102, p. 035901, Jan 2009.
- [91] L. Wiczorek, H. J. Goldsmid, and G. L. Paul, *In Thermal Conductivity 20*, edited by D. P. H. Hasselman and J. R. Thomas. Plenum, New York, 1989. 235.
- [92] J. L. Feldman, P. B. Allen, and S. R. Bickham, “Numerical study of low-frequency vibrations in amorphous silicon,” *Phys. Rev. B*, vol. 59, pp. 3551–3559, Feb 1999.
- [93] P. B. Allen and J. L. Feldman, “Thermal conductivity of disordered harmonic solids,” *Phys. Rev. B*, vol. 48, pp. 12581–12588, Nov 1993.
- [94] Y. H. Lee *et al.*, “Molecular-dynamics simulation of thermal conductivity in amorphous silicon,” *Phys. Rev. B*, vol. 43, pp. 6573–6580, Mar 1991.

- [95] M. S. Love and A. C. Anderson, “Estimate of phonon thermal transport in amorphous materials above 50 k,” *Phys. Rev. B*, vol. 42, pp. 1845–1847, Jul 1990.
- [96] J. J. Freeman and A. C. Anderson, “Thermal conductivity of amorphous solids,” *Phys. Rev. B*, vol. 34, pp. 5684–5690, Oct 1986.
- [97] J. L. Feldman, M. D. Kluge, P. B. Allen, and F. Wooten, “Thermal conductivity and localization in glasses: Numerical study of a model of amorphous silicon,” *Phys. Rev. B*, vol. 48, pp. 12589–12602, Nov 1993.
- [98] J. Fabian and P. B. Allen, “Anharmonic decay of vibrational states in amorphous silicon,” *Phys. Rev. Lett.*, vol. 77, no. 18, pp. 3839–3842, 1996.
- [99] R. O. Pohl, X. Liu, and E. Thompson, “Low-temperature thermal conductivity and acoustic attenuation in amorphous solids,” *Rev. Mod. Phys.*, vol. 74, p. 991, Oct 2002.
- [100] J. K. Bording, “Molecular-dynamics simulation of ge rapidly cooled from the molten state into the amorphous state,” *Phys. Rev. B*, vol. 62, pp. 7103–7109, Sep 2000.
- [101] H. J. C. Berendsen, J. P. M. Postma, W. F. van Gunsteren, A. DiNola, and J. R. Haak, “Molecular dynamics with coupling to an external bath,” *J. Chem. Phys.*, vol. 81, p. 3684, 1984.
- [102] D. E. Polk, “Structural model for amorphous silicon and germanium,” *J. Non-Cryst. Solids*, vol. 5, p. 365, 1970.

- [103] S. Kugler, L. Pusztai, L. Rosta, P. Chieux, and R. Bellissent, “Structure of evaporated pure amorphous silicon: Neutron-diffraction and reverse monte carlo investigations,” *Phys. Rev. B*, vol. 48, pp. 7685–7688, Sep 1993.
- [104] L. Wei *et al.*, “Heat conduction in silicon thin films: Effect of microstructure,” *Journal of Materials Research*, vol. 10, pp. 1889–1896, 1995.
- [105] J. E. Turney, E. S. Landry, A. J. H. McGaughey, and C. H. Amon, “Predicting phonon properties and thermal conductivity from anharmonic lattice dynamics calculations and molecular dynamics simulations,” *Phys. Rev. B*, vol. 79, no. 6, p. 064301, 2009.
- [106] W. A. Kamitakahara, C. M. Soukoulis, H. R. Shanks, U. Buchenau, and G. S. Grest, “Vibrational spectrum of amorphous silicon: Experiment and computer simulation,” *Phys. Rev. B*, vol. 36, pp. 6539–6542, Oct 1987.
- [107] D. Donadio and G. Galli, “Temperature dependence of the thermal conductivity of thin silicon nanowires,” *Nano Lett.*, vol. 10, no. 3, pp. 847–851, 2010.
- [108] Y. He, D. Donadio, J.-H. Lee, J. C. Grossman, and G. Galli, “Thermal transport in nanoporous silicon: Interplay between disorder at mesoscopic and atomic scales,” *ACS Nano*, vol. 5, no. 3, pp. 1839–1844, 2011.
- [109] J. Yang and T. Caillat, “Thermoelectric materials for space and automotive power generation,” *MRS Bulletin*, vol. 31, pp. 224–229, 2006.
- [110] X. W. Wang, H. Lee, Y. C. Lan, G. H. Zhu, G. Joshi, D. Z. Wang, J. Yang, A. J. Muto, M. Y. Tang, J. Klatsky, S. Song, M. S. Dresselhaus, G. Chen, and Z. F. Ren, “Enhanced thermoelectric figure of merit in nanostructured n-type silicon germanium bulk alloy,” *Appl. Phys. Lett.*, vol. 93, p. 193121, 2008.

- [111] A. Skye and P. K. Schelling, “Thermal resistivity of si-ge alloys by molecular-dynamics simulation,” *J. Appl. Phys.*, vol. 103, p. 113524, 2008.
- [112] J. Garg, N. Bonini, B. Kozinsky, and N. Marzari, “Role of disorder and anharmonicity in the thermal conductivity of silicon-germanium alloys: A first-principles study,” *Phys. Rev. Lett.*, vol. 106, no. 4, p. 045901, 2011.
- [113] A. Skye and P. K. Schelling, “Thermal resistivity of si-ge alloys by molecular-dynamics simulation,” *J. Appl. Phys.*, vol. 103, no. 11, p. 113524, 2008.
- [114] B. Abeles, “Lattice thermal conductivity of disordered semiconductor alloys at high temperatures,” *Phys. Rev.*, vol. 131, no. 5, pp. 1906–1911, 1963.
- [115] J. P. Dismukes, L. Ekstrom, E. F. Steigmeier, I. Kudman, and D. S. Beers, “Thermal and electrical properties of heavily doped ge-si alloys up to 1300k,” *J. of Appl. Phys.*, vol. 35, p. 2899, 1964.
- [116] J. P. Dismukes, L. Ekstrom, E. F. Steigmeier, I. Kudman, and D. S. Beers, “Thermal and electrical properties of heavily doped ge-si alloys up to 1300 k,” *J. Appl. Phys.*, vol. 35, no. 10, p. 2899, 1964.
- [117] P. Jund and R. Jullien, “Molecular-dynamics calculation of the thermal conductivity of vitreous silica,” *Phys. Rev. B*, vol. 59, p. 13707, 1999.
- [118] S. S. Mahajan and G. Subbarayan, “Estimating thermal conductivity of amorphous silica nanoparticles and nanowires using molecular dynamics simulations,” *Phys. Rev. E*, vol. 76, p. 056701, 2007.
- [119] S.-M. Lee and D. G. Cahill, “Heat transport in thin dielectric films,” *J. Appl. Phys.*, vol. 81, p. 2590, 1997.

- [120] T. Coquil, E. K. Richman, N. J. Hutchinson, S. H. Tolbert, and L. Pilon, “Thermal conductivity of cubic and hexagonal mesoporous silica thin films,” *J. Appl. Phys.*, vol. 106, p. 034910, 2009.
- [121] Y. K. Koh and D. G. Cahill, “Frequency dependence of the thermal conductivity of semiconductor alloys,” *Phys. Rev. B*, vol. 76, p. 075207, Aug 2007.
- [122] D. G. Cahill and R. O. Pohl, “Thermal conductivity of amorphous solids above the plateau,” *Phys. Rev. B*, vol. 35, p. 4067, 1987.
- [123] P. E. Hopkins, B. Kaehr, L. M. Phinney, T. P. Koehler, A. M. Grillet, D. Dunphy, F. Garcia, and C. J. Brinker, “Measuring the thermal conductivity of porous, transparent SiO_2 films with time domain thermoreflectance,” *J. Heat Tran.*, vol. 133, pp. 06160–1, 2011.
- [124] J. Horbach and W. Kob, “Static and dynamic properties of a viscous silica melt,” *Phys. Rev. B*, vol. 60, p. 3169, 1999.
- [125] A. Nakano, L. Bi, R. K. Kalia, and P. Vashishta, “Molecular-dynamics study of the structural correlation of porous silica with use of a parallel computer,” *Phys. Rev. B*, vol. 49, p. 9441, 1994.
- [126] S. N. Taraskin and S. R. Elliott, “Nature of vibrational excitations in vitreous silica,” *Phys. Rev. B*, vol. 56, p. 8605, 1997.
- [127] D. L. Price and J. M. Carpenter, “find out,” *J. Non-Crystalline Solids*, vol. 92, pp. 153–174, 1987.
- [128] S. Shenogin, A. Bodapati, P. Keblinski, and A. J. H. McGaughey, “Predicting the thermal conductivity of inorganic and polymeric glasses: The role of anharmonicity,” *J. Appl. Phys.*, vol. 105, p. 034906, 2009.

- [129] P. B. Allen, J. L. Feldman, J. Fabian, and F. Wooten, “Diffusons, locons, propagons: Character of atomic vibrations in amorphous si,” *Philos. Mag. B*, vol. 79, p. 1715, 1999.
- [130] G. J. Snyder and E. S. Toberer, “Complex thermoelectric materials,” *Nature Materials*, vol. 7, pp. 105–114, 2008.
- [131] A. J. Minnich, H. Lee, X. W. Wang, G. Joshi, M. S. Dresselhaus, Z. F. Ren, G. Chen, and D. Vashaee, “Modeling study of thermoelectric sige nanocomposites,” *Phys. Rev. B*, vol. 80, no. 15, p. 155327, 2009.
- [132] D. Donadio and G. Galli, “Atomistic simulations of heat transport in silicon nanowires,” *Physical Review Letters*, vol. 102, p. 195901, 2009.
- [133] A. I. Boukai, Y. Bunimovich, J. Tahir-Kheli, J.-K. Yu, W. A. G. III, and J. R. Heath, “Silicon nanowires as efficient thermoelectric materials,” *Nature*, vol. 451, pp. 168–171, 2008.
- [134] J.-H. Lee, J. C. Grossman, J. Reed, and G. Galli, “Lattice thermal conductivity of nanoporous si: Molecular dynamics study,” *Applied Physics Letters*, vol. 91, no. 22, p. 223110, 2007.
- [135] J. Lee, G. A. Galli, and J. C. Grossman, “Nanoporous Si as an Efficient Thermoelectric Material,” *Nano Letters*, vol. 8, pp. 3750–3754, 2008.
- [136] G. Joshi, H. Lee, Y. Lan, X. Wang, G. Zhu, D. Wang, R. W. Gould, D. C. Cuff, M. Y. Tang, M. S. Dresselhaus, G. Chen, and Z. Ren, “Enhanced thermoelectric figure-of-merit in nanostructured p-type silicon germanium bulk alloys,” *Nano Letters*, vol. 8, no. 12, pp. 4670–4674, 2008.

- [137] C. Bera, N. Mingo, and S. Volz, “Marked effects of alloying on the thermal conductivity of nanoporous materials,” *Phys. Rev. Lett.*, vol. 104, no. 11, p. 115502, 2010.
- [138] V. Samvedi and V. Tomar, “Role of heat flow direction, monolayer film thickness, and periodicity in controlling thermal conductivity of a si-ge superlattice system,” *J. Appl. Phys.*, vol. 105, p. 013541, 2009.
- [139] M. K. Y. Chan, J. Reed, D. Donadio, T. Mueller, Y. S. Meng, G. Galli, and G. Ceder, “Cluster expansion and optimization of thermal conductivity in si-ge nanowires,” *Phys. Rev. B*, vol. 81, no. 17, p. 174303, 2010.
- [140] P. J. Steinhardt, D. R. Nelson, and M. Ronchetti, “Bond-orientational order in liquids and glasses,” *Phys. Rev. B*, vol. 28, pp. 784–805, Jul 1983.
- [141] T. Li, D. Donadio, and G. Galli, “Nucleation of tetrahedral solids: A molecular dynamics study of supercooled liquid silicon,” *J. Chem. Phys.*, vol. 131, p. 224519, 2009.
- [142] S. N. Taraskin and S. R. Elliott, “Determination of the ioffe-regel limit for vibrational excitations in disordered materials,” *Philosophical Magazine B*, vol. 79, pp. 1747–1754, 1999.
- [143] Y. He, D. Donadio, and G. Galli, “Heat transport in amorphous silicon:interplay between morphology and disorder,” *Appl. Phys. Lett.*, vol. 98, p. 144101, 2011.